Angular dispersion of radio waves in mobile channels

Please check the document version of this publication:

Angular Dispersion of Radio Waves in Mobile Channels

Measurement based Analysis and Modelling

Angular Dispersion of Radio Waves in Mobile Channels

Measurement based Analysis and Modelling

PROEFSCHRIFT

ter verkrijging van de graad van doctor aan de
Technische Universiteit Eindhoven, op gezag van de
Rector Magnificus, prof.dr.ir. C.J. van Duijn, voor een
commissie aangewezen door het College voor
Promoties in het openbaar te verdedigen op
woensdag 10 december 2008 om 16.00 uur

door

Maurice Rogier Jozef Arthur Emanuel Kwakkernaat

geboren te Venray

Dit proefschrift is goedgekeurd door de promotoren:

prof.dr.ir. E.R. Fledderus
en
prof.Dr.-Ing. T. Kürner

Copromotor:
dr.ir. M.H.A.J. Herben

Cover design by Maurice Kwakkernaat
Cover photo by Bart van Overbeeke

Aan mijn ouders
Aan Anne-Marie

Samenstelling van de promotiecommissie:

prof.dr.ir. P.P.J. van den Bosch, voorzitter
prof.dr.ir. E.R. Fledderus, Technische Universiteit Eindhoven, eerste promotor
prof. Dr.-Ing. T. Kürner, Technische Universität Braunschweig, tweede promotor
dr.ir. M.H.A.J. Herben, Technische Universiteit Eindhoven, co-promotor
prof. Dr.-Ing. M. Haardt, Technische Universität Ilmenau
prof.dr. R. Bultitude, Carleton University
prof.dr. A.G. Tijhuis, Technische Universiteit Eindhoven
dr.ir. Y.L.C. de Jong, Communications Research Centre Canada

Summary

Angular Dispersion of Radio Waves in Mobile Channels

Measurement based Analysis and Modelling

Multi-antenna techniques are an important solution for significantly increasing the bandwidth efficiency of mobile wireless data transmission systems. Effective and reliable design of these multi-antenna systems requires thorough knowledge of radiowave propagation in the urban environment.

The aim of the work presented in this thesis is to obtain a better physical understanding of radiowave propagation in mobile radio channels in order to provide a basis for the improvement of radiowave propagation prediction techniques for urban environments using knowledge from 3-D propagation experiments and simulations combined with space-wave modelling. In particular, the work focusses on: the development of an advanced 3-D mobile channel sounding system, obtaining propagation measurement data from mobile radio propagation experiments, the analysis of measured data and the modelling of angular dispersive scattering effects for the improvement of deterministic propagation prediction models.

The first part of the study presents the design, implementation and verification of a wideband high-resolution measurement system for the characterisation of angular dispersion in mobile channels. The system uses complex impulse response data obtained from a novel 3-D tilted-cross switched antenna array as input to an improved version of 3-D Unitary ESPRIT. It is capable of characterising the delay and angular properties of physically-nonstationary radio channels at moderate urban speeds with high resolution in both azimuth and elevation. For the first time, omnidirectional video data that were captured during the measurements are used in combination with the measurement results to accurately identify and relate the received radio waves directly to the actual environment while moving through it.

The second part of the study presents the results of experiments in which the high-resolution measurement system, described in the first part, is used in several mobile outdoor experiments in different scenarios. The objective of these measurements was to gain more knowledge in order to improve the understanding of radiowave propagation. From these results the dispersive effects in the angular domain, caused by rough building surfaces and other irregular structures was paid particular attention. These effects not only influence the total amount of received power in dense urban

environments, but can also have a large impact on the performance and deployment of multi-antenna systems. To improve the data representation and support further data analysis a hierarchical clustering method is presented that can successfully identify clusters of multipath signal components in multidimensional data. By using the data obtained from an omnidirectional video camera the clusters can be related directly to the environment and the scattering effects of specific objects can be isolated. These results are important in order to improve and calibrate deterministic propagation models.

In the third part of the study a new method is presented to account for the angular dispersion caused by irregular surfaces in ray-tracing based propagation prediction models. The method is based on assigning an effective roughness to specific surfaces. Unlike the conventional reflection reduction factor for Gaussian surfaces, that only reduces the ray power, the new method also distributes power in the angular domain. The results of clustered measurement data are used to calibrated the model and show that this leads to improved channel representations that are better matched to the real-world channel behavior.

Contents

1

Introduction

1.1   Background and motivation

For several decades mobile communication mainly focussed on voice and text messaging services. Today, the success of cable & digital subscriber line (DSL) services and wireless local area networks (WLAN) has been accelerating the demand for mobile internet and multimedia applications with increasingly high-quality and high data-rate services. This trend is mainly caused by the ever growing developments in online applications, information sharing and digital social networks, which will drive users from "occasionally connected" towards "connected anytime-anywhere". The demands for such a scenario can partly be fulfilled by Third Generation (3G) techniques such as Universal Mobile Telecommunication System (UMTS) and enhancements such as High Speed Downlink Packet Access (HSDPA) and its uplink counterpart HSUPA. The further extension of UMTS towards Long Term Evolution (LTE), developed within the 3rd Generation Partnership Project (3GPP) and expected to be available in 2010, aims to offer peak rates up to 50 Mbps and 100 Mbps in up and downlink, respectively, using only 20 MHz bandwidth [1]. Furthermore, the currently emerging Worldwide Interoperability for Microwave Access (WiMAX) technologies, based on the IEEE 802.16 standard, are expected to offer peak rates up to 28 Mbps in downlink and 60 Mbps in uplink using only 10 MHz bandwidth [2].

To obtain sufficient coverage and quality of service (QoS) using existing and next generation technologies, operators move towards smaller cells such as pico-cells or femto-cells, mostly applied in indoor scenarios [3, 4]. The use of these smaller radio cells is mainly due to the fact that data-throughput and user-capacity can be increased

and interference be mitigated more easily if cell sizes are reduced. Furthermore, smaller radio cells can help to fill the gaps in signal coverage, especially in dense urban or indoor environments. The effective deployment and planning of these cells requires accurate knowledge about propagation behaviour in these areas and implies that propagation models include information about the local features of the environment at the receiver and transmitter locations.

Furthermore, next generation technologies make use of adaptive antenna technology, which includes single- or multiuser multiple-input multiple-output (MIMO) technology and spatial-division multiple access (SDMA). The use of these adaptive antenna techniques stems from exploiting the spatial or directional channel diversity in order to improve signal-to-interference-and-noise ratio (SINR) and, more importantly, increase spectral efficiency in order to achieve high data rates. The effective application of these techniques requires the design of appropriate antenna arrays and optimised smart antenna or MIMO algorithms. This can only be accomplished if sufficient knowledge about the radio channel in urban environments is available and real-world propagation models are used that include spatial or directional information.

Researchers and developers of multi-antenna technologies have an urgent need for realistic (stochastic) directional channel models that are intended for system level design and performance evaluation. Stochastically spatial channel models are often used for this purpose and generate multipath components (MPCs) that are chosen randomly from appropriate probability distributions. Examples of such models are the 3GPP SCM model [5] that has recently been extended by WINNER [6] and the COST273 model [7] that is being further developed within the COST2100 framework. A geometrical-based channel model that bridges the gap between stochastic directional channel models and deterministic ray-based models is the Ilmprop model [8,9], which can be used for the analysis of multi-user, time-variant, MIMO systems. The design, calibration and improvement of the above models, in turn, requires accurate (statistical) information on MPC parameters including angle-of-arrival (AOA) and their non-stationary behaviour [7].

It is widely recognised that the semi-empirical or stochastic propagation prediction models used for the planning and optimisation of conventional, macrocellular networks are not suitable if smaller cells or adaptive antennas are deployed [10–12]. Not only do these models produce highly inaccurate results in complex urban environments typical of micro cells [13], they are also incapable of predicting directional channel characteristics. For this reason, interest has shifted towards more advanced, so-called deterministic prediction methods, which use physical models of radio propagation mechanisms such as reflection and diffraction, as well as detailed information about the environment, for example locations of buildings and vegetation and their electromagnetic (EM) properties. Although these deterministic models provide a potential way to improve propagation prediction results, their dependence on detailed building databases and their excessive computational complexity have so far prevented their extensive use by mobile system operators [14]. Most current research in the area of deterministic propagation modelling deals with reducing the high computational complexity associated with deterministic propagation prediction, while further improving

prediction accuracy. In addressing both of these issues, it is important that the dominant mechanisms of propagation in mobile radio environments are identified, so that computational resources can be spent on modelling the significant mechanisms, and research efforts can be focused on improved modelling of the most significant ones. Results of high-resolution AOA measurements can provide valuable insight as to which mechanisms are dominant, because they provide information about the propagation trajectories corresponding to the strongest MPCs. Additionally, this information is important for the calibration of location specific model parameters and verification of prediction results, since the performance of deterministic propagation prediction models relies on accurate model calibration [15].

More specifically, there is an increased interest in the importance of modelling scattering phenomena that cause angular dispersion, such as scattering by vegetation or irregular surfaces. These effects can have a large impact on adaptive antenna technologies and need to be modelled more accurately [16–20]. Due to these scattering phenomena the arriving waves no longer have well-defined AOAs. In beamforming systems this strongly influences the effect of steering nulls in specific directions and, therefore, influences the capacity enhancement [21]. In MIMO systems the angular dispersion also has a major effect on the capacity and diversity gain [22, 23]. This means that adaptive antenna arrays need to be designed to match the different spatial characteristics of the radio environment in order to achieve significant performance enhancements.

Also, a further analysis of the rate of change of MPCs along a trajectory can help to reduce model complexity by extrapolating the composition of MPCs more effectively [24]. Furthermore, there is a need for more information about the propagation behavior in azimuth *and* elevation, e.g. for scenarios where over-rooftop or through-building propagation are dominant [25].

Several methods have been reported for the characterisation of directional radio propagation effects. In [26], a measurement system was described based on a virtual uniform circular array that can be used to characterise the angular properties of the channel at the receiver in a *static* scenario with high resolution in azimuth, but limited resolution in elevation. In [27] a method was presented based on a virtual rectangular array lattice to obtain improved elevation resolution. Due to the large measurement duration this system can only be used for *static* measurements. In [28, 29], systems were presented based on spherical and semi-spherical switched arrays that are capable of measuring radio channels at the receiver *while moving*, however, the performance in both angular domains is poor. Measurements of the directional propagation effects at *both* the transmitter and receiver have been reported in [30, 31] using the Elektrobit PropSound Channel Sounder [32]. Similar measurements were also reported in [33] using the RUSK ATM channel sounder [34]. Although these double-directional measurements provide much information about the double-directional propagation behaviour, the system complexity either limits the ability to perform measurements while moving through the environment or limits the angular resolution performance.

The above interests endorse the need for *more* accurate, high-resolution *mobile* prop-

agation measurements and analysis to improve propagation modelling in order to provide a basis for the design of radio-systems that are better matched to the real-world behavior of mobile radio-channels.

1.2   Previous work and objectives

The work presented in this thesis follows on previous work performed at the Eindhoven University of Technology (TU/e) by De Jong [25] and Jevrosimović [24]. In the work of De Jong the dominant effects of transmission through buildings and the scattering by trees were identified by experiments, modelled and incorporated into a deterministic prediction tool. One of the outcomes of this work was the need for more knowledge about the three dimensional propagation effects, i.e. improved analysis in the elevation domain. These effects are considered especially important for the analysis of ground reflections and over rooftop propagation in cells that have some of the characteristics of both macrocells and microcells. The work of Jevrosimović analyses the effects of real-world propagation in urban micro-cell environments on UMTS performance using smart antennas. Here, a method was proposed to compute information on the composition of the waves, i.e. ray parameters, at the central point of a "pixel"-area using a ray-tracing model and to extrapolate signals for any point within that pixel on the basis of that information. This reduces the computational complexity of deterministic prediction models along a trajectory, depending on the pixel size. In order to improve and further extend the pixel concept, more information is needed on the amount of change of the composition of the MPCs along a trajectory in real-world scenarios.

The present work was started in 2004 as a collaboration between the Communications Research Centre Canada (CRC) and TU/e and, in a later stage, the collaboration within the research framework Dutch Research Delta (DRD), a research cooperation between Koninklijke PTT Nederland (KPN), Netherlands Organisation for Applied Scientific Research (TNO) and a number of Dutch universities. In this thesis the results of this scientific work are presented. The aim of this work is to obtain a better physical understanding of radiowave propagation in mobile radio channels and to improve radiowave propagation prediction for urban environments using knowledge from 3-D propagation experiments and simulations combined with space-wave modelling. In particular, the main objectives of the work are:

- Development, implementation and evaluation of an advanced 3-D mobile channel sounding system.

- Obtaining propagation measurement data from mobile radiowave propagation experiments and performing analysis.

- Modelling local scattering mechanisms for the improvement of deterministic propagation prediction models.

The results will provide a basis for the development and analysis of improved propagation and channel models for 4th generation (4G) mobile communications systems.

1.3   Outline and contributions of this thesis

In this section a general overview and outline of this thesis is presented.

Chapter 2 reports the design and implementation of a measurement system that is capable of characterising the delay and angular properties of physically-nonstationary radio channels. The system is based on a 3-D antenna array and a wideband channel sounder that allows high-speed characterisation of the radio channel. The array geometry allows the application of the 3-D Unitary ESPRIT algorithm, explained in more detail in Chapter 3, to obtain high-resolution AOA estimations.

The main contributions and innovations of this chapter are:

- The design and implementation of a wideband radio channel sounder for high-speed characterisation of the radio channel and a 3-D tilted-cross switched antenna array that allows angle-of-arrival estimations at typical urban speeds (< 50 km/h). These results were published by the author in [35–37].

- The presentation, implementation and evaluation of a novel method to reduce mutual coupling in switched antenna arrays. These results were published by the author in [37, 38].

Chapter 3 describes the Unitary ESPRIT algorithm for three-dimensional parameter estimation, and its application in the analysis of data measured with the 3-D tilted-cross array that was described in Chapter 2. The 3-D Unitary ESPRIT algorithm and an improved version of the 3-D structured-least-squares (3-D I-SLS) method are presented. This method enables the Unitary ESPRIT algorithm to be applied to the 3-D tilted-cross array and to cross arrays in general. The main contributions and innovations of this chapter are:

- A new method is presented to apply 3-D Unitary ESPRIT to the specific category of cross arrays. This result was published by the author in [39].

- To minimise the effects of shadowing of the antenna array support structure a method was presented to detect and discard erroneous data with minimal loss of performance using a unique reliability criterion. This result was published by the author in [36].

- Theoretical and experimental results support the validity of the measurement method and show that multiple sources can be accurately characterised with a resolution performance of less than $5°$ in both azimuth and elevation.

In chapter 4, the results of several outdoor experiments are presented. The results are used to demonstrate the system capabilities in real-world urban environments and confirm that the composition of the multipath components along a trajectory can be

accurately characterised and tracked. Omnidirectional video data that were captured during the measurements are used in combination with the measurement results to accurately identify and relate the received radio waves directly to the actual environment while moving through it. This information helps to identify the most significant propagation mechanisms, which is vital for the the improvement and calibration of deterministic propagation models. Additionally, it can also be very useful when the measurement system is used as a diagnostic tool as will be shown in chapter 5.

The main contributions and innovations of this chapter are:

- The result of measurements along a trajectory are presented that show the capabilities and performance of the measurement system in a real-world scenario. Elevation angles are estimated accurately, but waves reflected by the ground are difficult to detect and phase distortions due to ground reflected waves reduce the estimation performance in elevation.

- The composition of the sets of multipath components along a trajectory can be accurately characterised and tracked. These sets of multipath components can be accurately related to the actual environment using omnidirectional video data that were captured during the measurements along the trajectory.

- The results from outdoor experiments in an urban environment show that over rooftop diffractions can be identified, as well as reflections from irregular building structures and diffuse scattering effects in the delay and angular domain. The results were partly published by the author in [37].

Chapter 5 describes the results of a diagnostic survey in the framework of a collaboration between TU/e, TNO-ICT and KPN. The results obtained in the scenarios presented here are obtained using the measurement system presented in Chapters 2, 3 and 4, and are especially important for mobile system operators, because they reveal some of the causes of insufficient propagation prediction. Measurements were performed in a dense urban environment in Amsterdam, the Netherlands. Results show that the measurement approach can be used to create a setup that is similar to the actual network scenario and is capable of accurately identifying the dominant propagation effects while moving through the environment. The results underline the limitations of the propagation prediction models currently used by mobile system operators such as KPN and the importance of accurate propagation knowledge and modelling.

The main contributions and innovations of this chapter are:

- Results obtained using a diagnostic analysis of the propagation effects inside an operational network using the recently developed high-resolution measurement system are presented. The main propagation mechanisms and the causes of unexpected signal degradation and interference are successfully identified with the help of omnidirectional video data.

- It is shown that shadowing and reflections from irregular building structures can be dominant propagation mechanisms.

- Current propagation models used by operators such as KPN do not provide sufficient flexibility and accuracy in complex urban environments, therefore, more accurate propagation modelling is required.

Chapter 6 describes the clustering of multidimensional measurement data. Since visual inspection and analysis of multidimensional measurement data can be very complex, a hierarchical clustering method is presented that can find clusters in the four-dimensional space (azimuth, elevation, delay, position). The method is capable of isolating the scattering effects of specific objects, which is important for the improvement and calibration of deterministic propagation models. Dispersive effects in the angular domain, caused by irregular building surfaces and other irregular structures was paid particular attention.

The main contributions and innovations of this chapter are:

- A method to cluster multidimensional estimation data obtained with a 3-D high-resolution channel sounder is presented and successfully applied to the measurement data. The work was published by the author in [40, 41].

- The results from several outdoor experiments are presented and used to apply the clustering algorithm. The scattering effects of specific objects can be isolated and the angular dispersion of these objects in azimuth as well as in elevation can be analysed. Angular spreads of less than one degree up to several degrees are observed, for different objects. The results have been published by the author in [40, 42].

Chapter 7 describes the modelling of scattering caused by irregular surfaces as a basis for implementation in ray-tracing methods. A novel approach is presented in a first attempt to model the dispersive effects, caused by scattering on surfaces which have "random" irregularities, directly *at the receiver*. The method is based on assigning a effective stochastic roughness to a specific surface. The scattering effects caused by the surface roughness include the *combined* effects of both the surface irregularities and changes in material properties. The results of simulations and measurements show that the method can be used to model the dispersive effects of rough surface scattering in a manner similar to using the reflection reduction factor for Gaussian surfaces, except that the reduced power in the specular direction is distributed in the angular domain. The possibility of including the model into a 3-D ray-tracer is outlined.

The main contributions and innovations of this chapter are:

- A novel approach to model the dispersive effects of rough surface scattering directly at the receiver is presented. The model generates instantaneous realisations of the channel at the receiver and includes both the coherent and incoherent components. The work has been published by the author in [43].

- The results from outdoor experiments that were conducted to study scattering from a rough building surface are presented and used to calibrate the model. The effective surface roughness in the model is calibrated through the angular

spread that is generated by the surface and estimated from high-resolution measurement results. The results obtained from measurements of scattering from a building with a rough surface show that it is possible to calibrate the ray-tracing model using measurements of scattering from a small area and then apply it to accurately predict the effects of scattering from the total, larger surface.

Finally, Chapter 8 presents a summary of the main results together with the general conclusions from the work conducted during the thesis project reported on herein and provides recommendations for future research.

2

Angle-of-arrival measurement system

2.1   Introduction

From the general introduction in the previous chapter it follows that identifying the dominant mechanisms of propagation in mobile radio environments is important, so that computational resources are spent on modelling the most significant mechanisms, and research efforts can be focused on their modelling. Results of high-resolution angle-of-arrival (AOA) measurements can provide valuable insight as to which mechanisms are dominant, because they provide information about the propagation trajectories corresponding to the strongest multipath components (MPCs).

Several measurement systems have been reported in literature that are capable of measuring the delay and angular characteristics of mobile radio channels [26–34]. A number of prominent systems that are considered important for the work reported herein are listed below.

- In [26], a high-resolution measurement system that used the uniform circular array multiple signal classification (UCA-MUSIC) algorithm applied to a synthetic circular array geometry was described. Although this system can be used to characterise the delay and angular properties of the channel with high resolution in azimuth ($< 5°$), the resolution in elevation is poor ($\gg 5°$) and there is an ambiguity in the elevation domain. This system cannot perform measurements under mobile conditions, because a single measurement sample takes several

seconds, while the channel coherence-time is in the order of micro-seconds, depending on the speed of the mobile.

- In [29], a system was presented that can describe the three-dimensional spatial radio channel using a spherical array geometry. Although this system is capable of measuring time-variant radio channels, its resolution in both angular domains is poor (up to 40°).

- More recently a measurement system was described in [28] that used a semi-spherical array that can measure angular characteristics under mobile conditions, but only with a limited elevation range and poor resolution in azimuth (up to 26°) and elevation (up to 44°).

In this chapter, the design and implementation of a wideband high-resolution mobile radio channel measurement system is presented. This system is capable of characterising the delay and angular properties of mobile radio channels with a resolution better than 5° in *both* the azimuth and elevation domain without ambiguities and while *moving* through the environment at moderate urban speeds. Firstly, an overview of the general system specifications is presented in Section 2.2. Secondly, the specifications of the modified channel sounder are described and a novel 3-D tilted-cross antenna array which forms an important part of the system is presented. The array geometry allows the application of 3-D unitary estimation of signal parameters via rotational invariance technique (Unitary ESPRIT) for high-resolution parameter estimation, which will be explained in more detail in Chapter 3.

In Section 2.3 a method is developed to reduce the negative effects of mutual coupling in switched antenna arrays used in AOA estimation systems. The concept as well as computational and experimental results are presented, which demonstrate that the method can be applied to the 3-D tilted-cross antenna array and switched antenna arrays in general. Finally, Section 2.4 gives conclusions.

2.2   Measurement system

Parts of the measurement system described in this chapter were designed and built in close co-operation between the Technische Universiteit Eindhoven (TU/e) and the Communications Research Centre Canada (CRC), Ottawa, Canada. These parts were combined and further improved at the TU/e were the system has been in use since March 2006.

The system operates in the frequency band between 2200-2300 MHz, which is close to the current UMTS/LTE spectrum between 1920-2170 MHz and the additional available spectrum for LTE between 2500-2690 MHz [1]. The current measurement system was realised by extending and modifying parts of the previous wideband radio channel sounder described in [25]. This system is capable of measuring wideband radio channel properties in a stationary measurement scenario. Here, the pseudonoise (PN) correlation method is used to provide an estimate of the complex impulse response

(CIR) of the channel under measurement. The demand for more accurate measurement results and performing measurements under mobile conditions were the main drivers behind the development of the new system. A comparison between the current and the previous measurement system specifications is shown in Table 2.1. This comparison shows a significant improvement in elevation resolution and a large increase of the effective acquisition rate, which allows measurements at moderate urban speeds. In Fig. 2.1, a block diagram of the new measurement system is shown.

To perform accurate CIR measurements with a moving antenna and receiver, the number of samples recorded while the receiver is connected to each antenna needs to be reduced as much as possible and the effective acquisition rate of the channel sounder needs to be increased considerably. With the current system design these demands have been spectacularly achieved. Both of these measures are needed to prevent large estimation errors caused by the variation of the phases of the signals on all antenna elements during one snapshot. Here, a *snapshot* is defined as a data file that results from the sampling of the received signal on each of the antenna elements in the array. To keep the variation of the phases as little as possible, the PN sequence length of the channel sounder was reduced from 511 to 255 bits, which in turn reduces the unambiguous range from 10.22 μs to 5.10 μs. Since the measurement system is designed for use in microcells the unambiguous range of 5.10 μs is sufficient. Furthermore, the effective sampling rate was halved and the number of antenna elements was reduced to 31. By performing the correlation of the received baseband data samples with the replica data samples off-line (post processing), the effective acquisition rate is increased even further. The time to obtain sufficient measurement data necessary to produce a single CIR is little more than the period of the PN sequence itself, i.e. 5.10 μs. Due to the above measures, the acquisition rate was increased by a factor of more than 3000, which allows high-speed characterisation of the radio channel and makes it possible to perform measurements at typical urban speeds (< 50 km/h).

2.2.1 Channel sounder

The channel sounder transmitter generates a 50 Mchip/s PN sequence with a period of 255 chips which modulates a 900 MHz carrier using binary phase-shift keying (BPSK). The resulting signal is bandpass filtered and up-converted by a 1350 MHz local oscillator to a center-frequency of 2250 MHz. The modulated 2250 MHz signal is bandpass filtered, amplified to a maximum power of +40 dBm and radiated via an antenna appropriate for the measurement scenario. Calibrated rubidium standards provide synchronisation between the local oscillators at the transmitter and receiver.

Table 2.1: Measurement system specifications.

	Previous system	Current system
Carrier frequency (MHz)	2250	2250
1-dB Bandwidth (MHz)	100	100
Nominal output power (dBm)	+27	+27/+40
Receiver type	sliding-correlator	off-line sliding-correlator
Time resolution (ns)	20	20
Azimuth angular resolution (deg)	< 5	< 5
Elevation angular resolution (deg)	$\gg 5$	< 5
PN sequence length	511	255
Unambiguous range (μs)	10.22	5.10
Effective sampling rate (samples/bit)	4	2
Multipath Power Sensitivity Ratio (dB)	40	35
Effective acquisition rate (CIR/s)	9.8	31155
Snapshot duration (s)	16.0	0.192
Number of (synthetic) array elements	157	31
Maximum array dimension (m)	0.30	0.60
Maximum allowable velocity (km/h)	0	50[†]

[†] A maximum phase-change of 7 degrees is tolerated over the time between when the first antenna is sampled and when the last antenna is sampled, during a single snapshot.

(a)

(b)
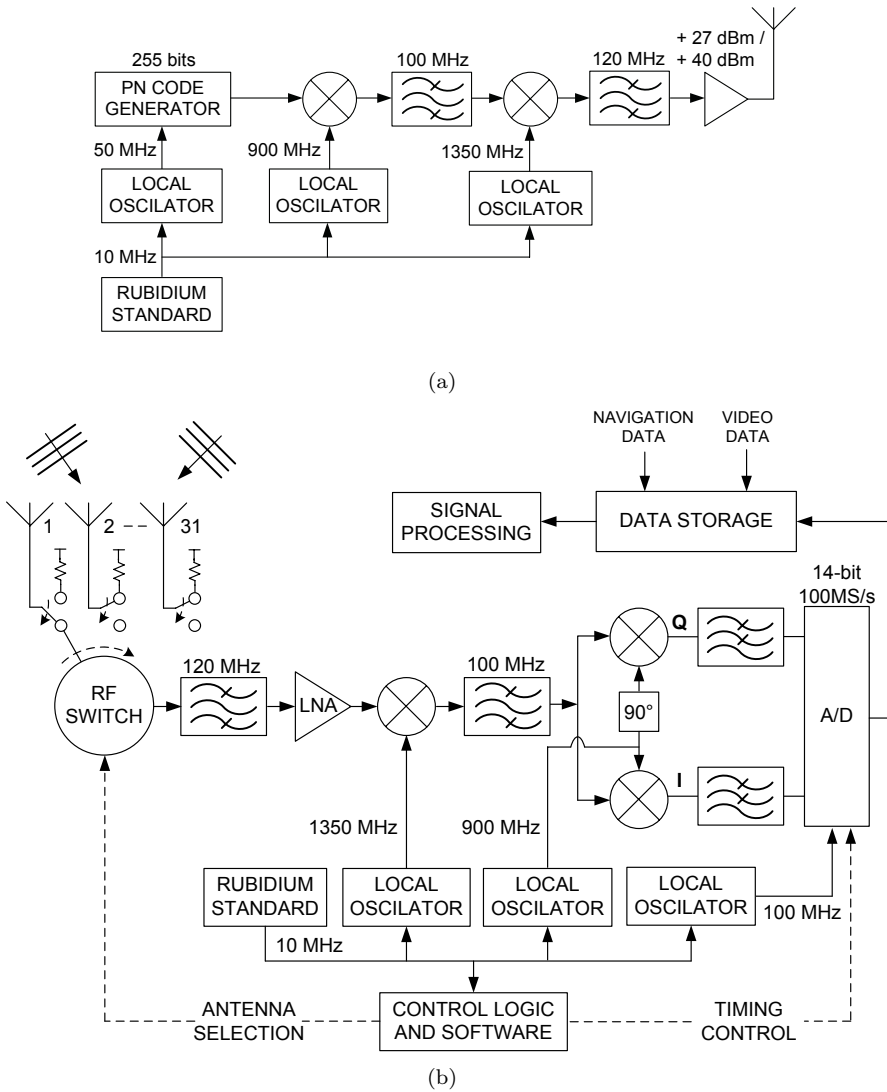
Fig. 2.1: Mobile radio channel sounder. (a) Transmitter. (b) Receiver.

At the channel sounder receiver a switched antenna array consisting of 31 antenna elements is used. The signal from each of the 31 antennas is received via an RF switch. The signal at the output of the RF switch is bandpass filtered to reduce interference and amplified by a low-noise amplifier (LNA). The LNA output is then down-converted by a 1350 MHz local oscillator and demodulated to baseband using in-phase (I) and quadriphase (Q) branches. After an anti-aliasing low-pass filter the baseband data samples are digitised at a rate of 100 Msamples/s using a 14-bit AD converter, transferred, and stored by the data collection system. Subsequently, estimates for the CIRs of the radio channel are determined *off-line* by correlation of the stored measurement data samples with a locally stored digitised replica maximum-length sequence, which is obtained from a back-to-back measurement. In such a back-to-back measurement scenario the transmitter-output is connected directly to the receiver-input via an appropriate cable and known attenuation. This calibration procedure also ensures accurate measurements of the absolute multipath intensities. The processed data samples consist of CIRs with an *unambiguous range* of 5.10 μs and a multipath Power Sensitivity Ratio (MPSR) of 35 dB. Here, the MPSR is defined as the difference in dB between the maximum and minimum power value that can still be detected in the power-delay profile (PDP) obtained from a back-to-back measurement. The reduction of the MPSR from 40 dB for the previous system to 35 dB for the current system is related to the reduction of the PN sequence that reduces spreading gain (-3dB) and the additional noise caused by signal losses in the switches before the LNA.

Results from preliminary back-to-back measurements showed that the demodulated I and Q branches exhibit a small amplitude and phase imbalance that cannot easily be reduced further. This imbalance adds a complex conjugate version of the ideally received signal, if no imbalance would be present, to the received signal. This in turn will cause mirrored versions of the true estimates in the angular spectrum. To compensate for this effect, a method to correct the IQ-imbalance via post processing was used successfully and is described in the next section.

2.2.2   Compensation of I/Q imbalances

When a continuous wave (CW) signal with frequency ω is used to modulate a carrier at the transmitter, ideally the demodulated i and q outputs of the receiver are

$$i(t) = \cos(\omega t) \tag{2.1}$$

$$q(t) = \sin(\omega t), \tag{2.2}$$

and the resulting complex received signal

$$x(t) = i(t) + jq(t). \tag{2.3}$$

If there is a DC-bias β for each path and a total amplitude and phase error of ϵ and φ, respectively, the down-converted i and q signals become [44]

$$\hat{i}(t) = i(t)(1 + \frac{\epsilon}{2}e^{-j\frac{\varphi}{2}}) + \beta_i \qquad (2.4)$$

$$\hat{q}(t) = q(t)(1 - \frac{\epsilon}{2}e^{j\frac{\varphi}{2}}) + \beta_q. \qquad (2.5)$$

It can be shown that without loss of generality the total phase error φ can be allocated to the q path and the amplitude error ϵ to the i path, which results in

$$\hat{i}(t) = i(t)\alpha + \beta_i \qquad (2.6)$$

$$\hat{q}(t) = q(t)\cos(\varphi) + i(t)\sin(\varphi) + \beta_q, \qquad (2.7)$$

where $\alpha = 1 + \epsilon$. From Eqs. (2.6) and (2.7) $i(t)$ and $q(t)$ can be determined as

$$i(t) \;=\; \frac{\hat{i}(t) - \beta_i}{\alpha} \qquad (2.8)$$

$$q(t) \;=\; \frac{-\sin(\varphi)(\hat{i}(t) - \beta_i)}{\alpha\cos(\varphi)} + \frac{1}{\cos(\varphi)(\hat{q}(t) - \beta_q)}. \qquad (2.9)$$

The above two expressions describe the compensation method and imply that improved versions for the measured i and q channels can be obtained, if values for α, φ, β_i and β_q can be determined.

Assume that $\hat{i}(t)$ and $\hat{q}(t)$ are obtained from a back-to-back measurement. Values for β_i and β_q are found from

$$\beta_i \;=\; <\hat{i}(t)> \qquad (2.10)$$

$$\beta_q \;=\; <\hat{q}(t)>, \qquad (2.11)$$

where $< . >$ denotes the mean over an integer number of periods. What remains is finding α and φ, which can be determined from

$$<\hat{i}(t)\hat{i}(t)> = \alpha^2 <\cos^2(\omega t)> = \alpha^2 \left\langle \frac{1}{2} + \frac{1}{2}\cos(2\omega t) \right\rangle = \frac{1}{2}\alpha^2, \qquad (2.12)$$

and

$$<\hat{i}(t)\hat{q}(t)> = \frac{1}{2}\alpha^2\sin(\varphi). \qquad (2.13)$$

By performing a back-to-back measurement, the following stable values for α, φ, β_i and β_q are determined

$$\alpha = 0.8284$$
$$\varphi = 0.0079\pi$$
$$\beta_i = 0.0073$$
$$\beta_q = 0.0059.$$

These values are only dependent on the receiver characteristics and are, therefore, used to compensate for the I/Q imbalance in all the measurement results in this work. Fig. 2.2 shows the result of the back-to-back data before and after applying the compensation method. It should be noted that this compensation method slightly colours the noise statistics, in contrast to the white noise assumption that is used in Sections 3.2 and 3.3.4 on pages 32 and 42.
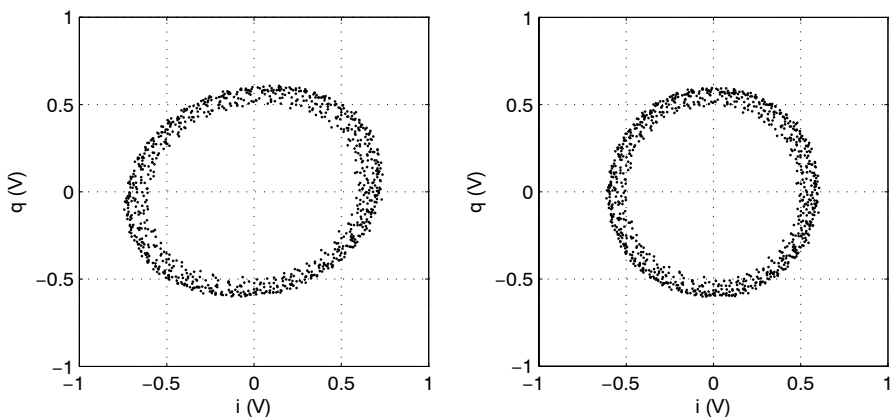
Fig. 2.2: Results of the i and q signals, left, before compensation and right, after compensation.

2.3 Antenna array

In order to accurately measure the directional radio propagation characteristics while moving through the environment, the antenna array that is used should have a uniform estimation performance, high resolution, minimum estimation ambiguities and the total number of antenna elements should be reduced to a minimum. At the same time, the applicability of existing high-resolution algorithms should be taken into account. The design goal for the angular resolution in both azimuth *and* elevation is to be better than 5° and the accuracy should be ≪ 1°.

2.3.1 Array design

The uniform circular array (UCA) has drawn much attention due to its perfectly uniform performance in azimuth. When maximum resolution is required the linear array performs optimally, but with a high loss of uniformity and increased ambiguities. Since neither of the two array geometries mentioned above are optimal in terms of both uniformity and resolution, an intermediate solution that minimises performance variation and ambiguities and maximises resolution capabilities is preferred. In [45] it was shown that Y-shaped or X-shaped geometries exhibit the lowest performance

variation together with the highest resolution capabilities when the same number of antenna elements are available. Unfortunately, as with all planar array geometries these geometries exhibit a very poor performance at low elevation angles and cannot distinguishing waves coming from positive and negative elevation angles. This makes them highly unsuitable for azimuth and elevation AOA estimation. The only solution to this is to extend the geometries to the third dimension.

Extending the circular array geometry to a spherical or cylindrical geometry increases the resolution performance in the elevation domain, but reduces the resolution performance in the azimuth domain dramatically when the same number of elements are used. This is due to the fact that the same number of elements have to be distributed across a spherical or cylindrical surface, which reduces the aperture in the azimuth domain. Since Y-shaped or X-shaped geometries exhibit larger resolution capabilities, their extension to the third dimension results in high resolution capabilities in both azimuth and elevation together with a low performance variation. To create such a structure the Y-shaped and X-shaped geometries are extended into 3D to form the so called 3-D tilted-cross array, shown in Fig. 2.3. The array consists of three perpendicular linear array arms positioned in an x, y, z-axis geometry that is firstly tilted 45 degrees around the x-axis and secondly 35.26 degrees around the y-axis, such that the ends of each of the three array arms end in the same horizontal plane.
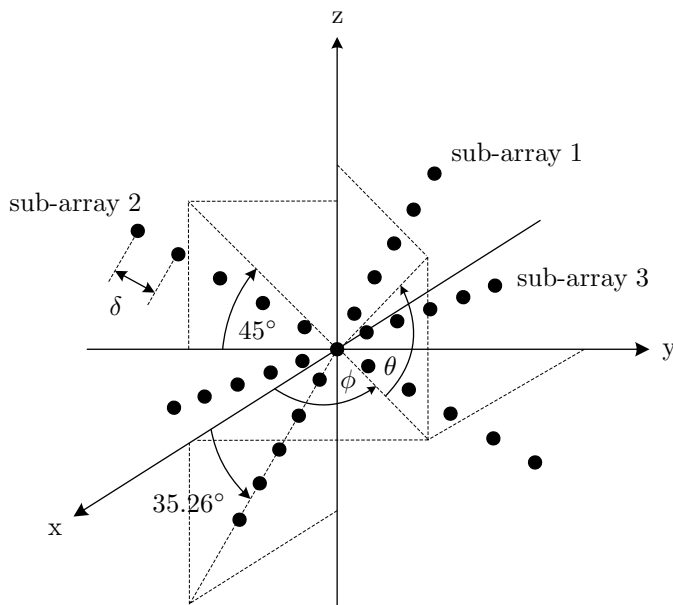
Fig. 2.3: 3-D Tilted-cross antenna geometry.

The maximum number of antenna elements that can be used in the 3-D tilted-cross array is limited by two important factors. Firstly, the total array size is limited. This is a requirement due to the plane wave assumption and the narrow-band array assumption, which are both assumptions used by the signal model and the high-

resolution algorithm described in Section 3.2 on page 32 and in Section 3.3 on page 35, respectively. Furthermore, due to the limited size of practical measurement platforms, i.e. vehicle rooftops, the final array size is also limited. Secondly, the time that it takes to sample one complete set of data from all elements should be short enough to assume the channel to be physically stationary during mobile measurements.

The above considerations were taken into account and a 3-D switched antenna array was designed that consists of 31 antenna elements that are positioned in a 3-D tilted-cross configuration. The elements are grouped in three linear sub-arrays of $M = 11$ elements, sharing the same centre element. To prevent grating lobes, the elements are equally spaced according to the Hansen-Woodyard condition [46] at $\delta = 0.45\lambda$, where λ represents the wavelength corresponding to the centre-frequency, i.e. 2250 MHz. Although the Hansen-Woodyard condition applies to linear arrays, simulations have shown that for the 3-D tilted-cross array, which is made up of a combination of linear arrays, this condition still results in the best trade-off between directivity and side-lobe level. The 3-D geometry, shown in Fig. 2.3, occupies a volume that is equal to that of a sphere of radius 30 cm, which is approximately two times the wavelength at the operating frequency. This novel 3-D array geometry is designed such that high-resolution AOA estimation is possible in azimuth (ϕ) as well as in elevation (θ). Moreover, due to the tilting of the array the resolution performance and uniformity are optimal in the area where the elevation angles are close to zero, which includes the predominant elevation area for typical rural and urban scenarios [7]. When beamforming is applied to all elements, the antenna array exhibits a half-power-beam-width (HPBW) of 16 degrees in azimuth as well as in elevation in comparison to 40 degrees HPBW in the case of a spherical geometry with the same number of elements [29]. The uniform element spacing and centro-symmetry of the geometry allow for the application of the recently improved version of the multidimensional Unitary ESPRIT algorithm [39] for low-complexity, high-resolution AOA estimation, and is described in Section 3.3.

To limit the complexity of the receiver, the measurement system uses time-division multiplexing to acquire data on each antenna element in the array in sequence. This is effectively equal to simultaneously measuring all 31 antennas, if there are no changes on the channel during the total measurement interval. In practice, however, it is assumed that any such changes are insignificant, imposing a requirement that measurements be recorded as quickly as possible. Note that it was recently shown in [47] that in time-division multiplexed MIMO channel sounders phase noise can lead to significant errors in terms of estimated mutual information and channel capacity. In deterministic channel estimations, this causes a "randomisation" of the channel that can lead to false AOA estimations. In *one-sided* switching systems, such as the system presented here, this effect is, however, not significant [48]. Furthermore, it was shown in [49] that phase fluctuations can cause AOA estimation errors, but this effect is very limited in the case of high antenna switching speeds and accurately calibrated rubidium standards.

The timing diagram of the measurement system for obtaining data samples from all 31 antenna elements is shown in Fig. 2.4. The time needed to sample sufficient data

on a single antenna to produce a single CIR is represented by t_p. The time needed for the recording of one snapshot to produce a single CIR for each of the 31 antennas is represented by t_s. The complete acquisition cycle, t_c, needed to sample, transfer and store one set of snapshot data is longer than t_s to allow for transferring and writing the data to disk. It is discovered that data recorded during the time immediately after switching from one element to another can be corrupted. To make possible the discarding of this data during post processing, an extra guard interval of $t_g = 0.9$ μs is added. As a result, $t_s = 31 \cdot (t_g + t_p) = 186$ μs.
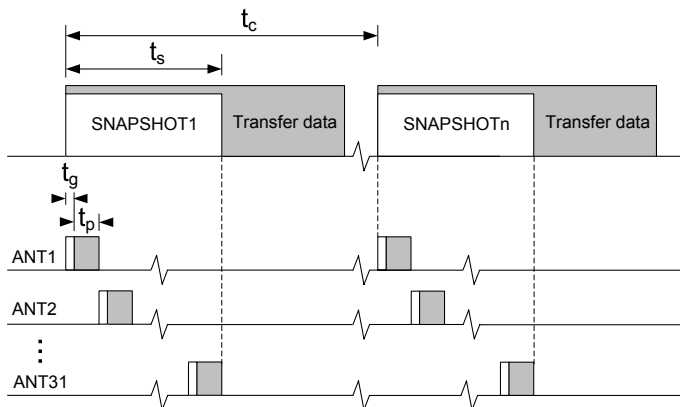
Fig. 2.4: Timing diagram for data aquisition.

To enable measurements at typical urban speeds the phase variation introduced by motion should be small enough to prevent large estimation errors. This means effectively that there is a worst case maximum distance the antenna array can travel during the time for the recording of one snapshot, such that the estimation error caused by this motion remains sufficiently low. A typical urban speed of $V = 50$ km/h or 13.9 m/s corresponds to a travel distance of $s = V \cdot t_s = \lambda/51.6$. This speed generates a maximum phase variation of $7°$ over the time between when the first antenna is sampled and when the last antenna is sampled. Simulations have shown that in this case, with Unitary ESPRIT applied, the angular RMS estimation error in azimuth and elevation caused by the motion remains sufficiently low, i.e. $< 0.1°$, in accordance with the design goal discussed at the beginning of Section 2.3.

2.3.2 Array realisation

The 3-D tilted-cross antenna array, shown in Fig. 2.5, was designed and built at CRC by the author in collaboration with CRC colleagues. It is built using six 30 cm long hollow carbon fiber tubes that are glued together at the centre and through which all the signal and control cables run. Smaller 6 cm carbon fiber tubes, spaced uniformly at a distance of $\delta = 0.45\lambda$, are glued vertically on top of the structure

and support the antennas. The support structure is populated with 1-dBi drooping radial monopole antennas, shown in Fig. 2.7 on page 24, which are designed to be resonant at 2250 MHz and operate over a 100 MHz bandwidth. The antennas have an omnidirectional radiation pattern in the azimuth plane, a vertical 3-dB beamwidth of $80°$ and a maximum directivity at $0°$ elevation. The antenna bandwidth (return loss $(S_{11}) < -15$ dB) extends from 2150 to 2350 MHz.

To reduce scattering and mutual coupling effects of the metal cables inside the rods, flexible microwave absorbing material and absorbing paste is used to cover the rods. This absorber material has a reflectivity of -20 dB or less in the operating bandwidth.

To reduce the additional stress on the structure caused by the weight of the absorber, polycarbonate rods are added for extra support. A cylindrical shielded box is mounted underneath the antenna array structure and holds a 31:1 RF antenna switchboard that connects the antennas to the receiver in sequence. The top of the cylindrical box is covered with thick absorbing material to reduce possible scattering effects.
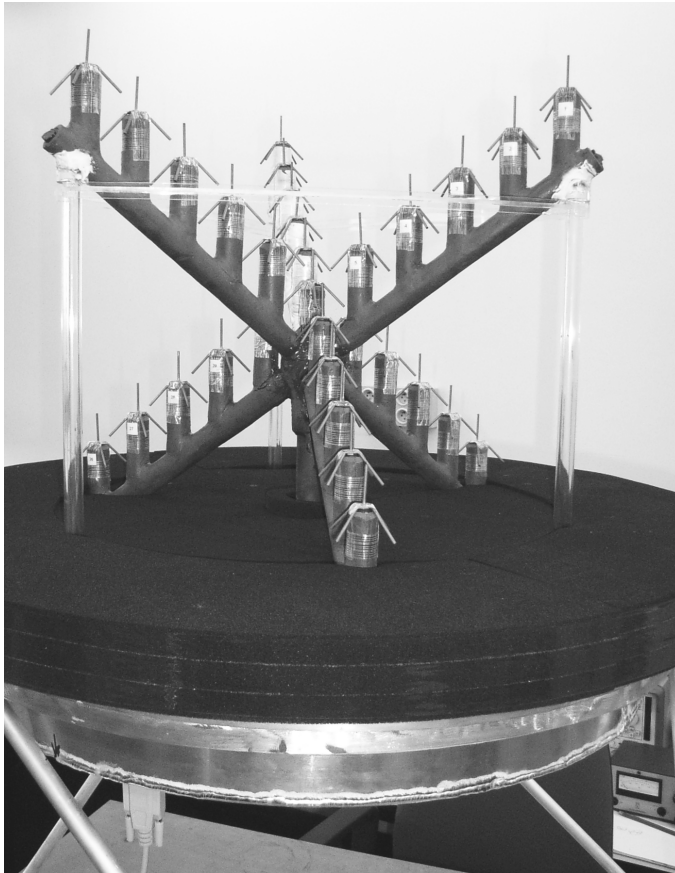
Fig. 2.5: 3-D Tilted-cross switched antenna array.

2.4 Mutual coupling reduction

A well know major problem that degrades the performance of antenna arrays is the undesirable electromagnetic coupling between the elements in the array, often referred to as mutual coupling (MC) [46]. This MC phenomenon strongly affects the radiation pattern and the input impedance of the antenna elements. Since ignoring the presence of MC will degrade the array performance, techniques that minimise MC effects are important. Even if the antenna pattern and input impedance are distorted due to MC, it is theoretically possible to eliminate these effects by correcting the voltages at the terminals of the array elements by using an impedance matrix [50]. In order to avoid significant performance degradation, this correction matrix must be very accurately known over the entire system bandwidth. Furthermore, this matrix is not necessarily invariant in terms of time and measurement circumstances, which makes calibration a great challenge in practice. If an antenna array exhibits perfect circular symmetry, the effects of mutual coupling can also theoretically be avoided by expanding the open-circuit voltages into a limited number of phase modes, the number of which depends only on the electromagnetic dimensions of the array [51]. In order to apply this technique, the antenna separation distance needs to be decreased, which means that the number of elements increase if the same aperture is considered. The technique requires perfect symmetry as well as accurate characterisation of the array steering matrix over the entire angular domain, which can be difficult to achieve in practice. Instead of compensating for MC effects, it is therefore desirable to *suppress* these effects as much as possible, so that the actual properties of the antennas are as close as possible to their ideal properties. Additionally, compensation techniques such as the ones described above could be used to *further* reduce MC effects. In AOA estimation systems, MC effects can also be avoided with the aid of virtual arrays, in which a single antenna is moved in space, for example along a linear or circular trajectory [26,27,52]. This technique can, however, only be used for stationary measurements and requires advanced mechanics to create array geometries other than linear or circular.

When *switched* antenna arrays are used, such as the one presented in the previous section, MC effects can also be minimised by changing the termination of the non-active (parasitic) elements in the switched antenna array [53]. It was shown in [54–56] that suppression of the induced current can be achieved by terminating the passive antennas in a suitably chosen reactive impedance. By using this approach it is possible, for example, to completely eliminate re-radiation in the H-plane of the antenna. This approach is used in the next section, where a method is presented to reduce mutual coupling in switched antenna arrays.

2.4.1 Concept

Mutual coupling between antenna elements in switched antenna arrays are the result of secondary radiated fields from passive antennas, produced by induced displacement currents due to the radiated field from the active antenna element [57,58]. The secondary radiated fields in turn cause induced displacement currents in the active

antenna element, which distort its radiation pattern and input impedance. The coupling of the active antenna element with the passive antennas can be reduced by minimising the radiated power of the passive antennas. This radiated power depends strongly on the distribution of the current along the antenna. In general, the induced current magnitude is large and the mutual coupling is strong if the passive antennas are nearby, equally polarised and are of resonant size, i.e., if they have similar electrical dimensions. To prevent grating lobes from occurring, the inter-element separation (periodicity) can usually not be made larger than half the wavelength. In order to obtain maximum gain in the desired plane, the polarisation directions for each antenna are usually taken as being equal. To reduce the induced current magnitude the electrical dimensions of the antennas can be changed through the impedance in which their feedpoints are terminated. This is visualised in Fig. 2.6, where the current distributions of two nearby vertical polarised dipole antennas with different feedpoint terminations are shown. By correctly changing the feedpoint impedance of, for example, vertically polarised passive antennas positioned in a horizontal plane, the total induced current magnitude and, therefore, also the secondary radiated power, can be reduced. As a result, considerable suppression of mutual coupling can be achieved.
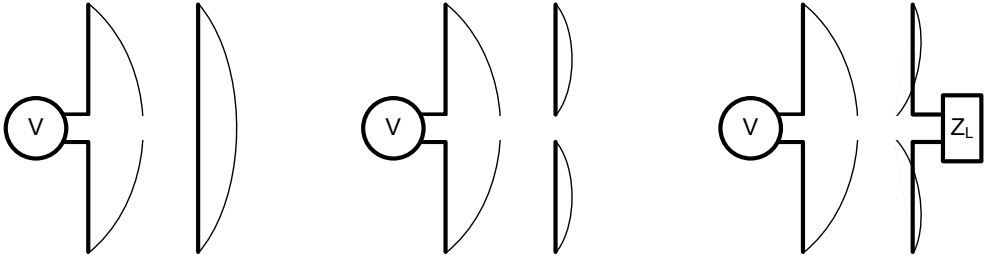
Fig. 2.6: Current distributions in an active and nearby passive dipole antenna with the feedpoint of the passive antenna (left) short-circuited, open-circuited (middle) and terminated in an impedance that minimises the total re-radiated field magnitude (right).

The induced current in a passive dipole antenna of height $2h$ (or monopole antenna of height h) in the vicinity of an active element of comparable length can be approximated by [59]

$$I(z) = \frac{E^{\text{inc}}}{\beta_0} \left[u(z) - v(z)u(0)\frac{Z_L Z_0}{Z_L + Z_0} \right], \qquad -h \leq z \leq h, \qquad (2.14)$$

where E^{inc} is the incident field created by the active antenna element, Z_0 is the impedance of the antenna, Z_L is the impedance of the load, $\beta_0 = 2\pi/\lambda$, λ equals the wavelength, $u(z)$ is the distribution of the current for the passive unloaded antenna, $v(z)$ is the distribution of the current in the active element and h is the antenna height. Expressions for $u(z)$ and $v(z)$ and the definition of the antenna height h are available in Appendix A.

It is shown in [54] that an impedance can be determined that, when inserted at the feedpoint of the antenna, decreases the amplitude and modifies the phase of the

induced current in such a way that the re-radiated field is directed upward, and a minimum reradiated field is achieved in the H-plane. The technique only effectively minimises the reradiated field in the H-plane, but not in other directions. For antennas positioned at relatively small distances this may not result in low mutual coupling effects. To minimise the re-radiated field in all directions, it is proposed here to minimise a cost function that represents the total reradiated field in all directions derived from the theory in [54, 59]. Although it would be of interest to minimise MC based on the total 3-D array geometry instead of the two-element scenario, simulations not presented here have shown that this does not lead to a more optimal result.

By using (2.14) it is shown in Appendix A that the radiation field of the passive monopole antenna at distance r and elevation angle Θ is given by

$$E(r, \Theta) = \frac{j\zeta_0 E^{\mathrm{inc}} e^{-j\beta_0 r}}{2\pi\beta_0 r} u(0) \left\{ \frac{G_m(\Theta, \beta_0 h)}{1 - \cos\beta_0 h} - \frac{F_m(\Theta, \beta_0 h) + TG_m(\Theta, \beta_0 h)}{\sin\beta_0 h + T(1 - \cos\beta_0 h)} \frac{Z_L}{Z_0 + Z_L} \right\}, \quad (2.15)$$

where $\zeta_0 = 120\pi\ \Omega$, $u(0)$ is equal to the current at the base of an unloaded antenna. Expressions for T, $G_m(\Theta, \beta_0 h)$ and $F_m(\Theta, \beta_0 h)$ are available in Appendix A. Now, an impedance Z_L can be determined for a idealised monopole that minimises the re-radiated field in all directions by minimising the following expression

$$\min_{Z_L} \left(\int_{-\pi/2}^{\pi/2} \frac{G_m(\Theta, \beta_0 h)}{1 - cos\beta_0 h} - \frac{F_m(\Theta, \beta_0 h) + TG_m(\Theta, \beta_0 h)}{sin\beta_0 h + T(1 - cos\beta_0 h)} \frac{Z_L}{Z_0 + Z_L} d\Theta \right). \quad (2.16)$$

With the aid of this method, the termination for the antennas used in the switched antenna array is determined to be $Z_L = j245\ \Omega$.

2.4.2 Computational analysis

In order to verify the theory presented in the previous section and to investigate the characteristics of the reduction of MC effects using different terminations on the passive elements, simulations were performed on a two-element antenna array positioned in the horizontal plane. The antenna elements were identical to the elements used in the switched antenna array and consist of vertically polarised drooping radial monopole antennas that are designed to be resonant at 2250 MHz and operate over a 100 MHz bandwidth. This type of antenna was chosen because of its omnidirectional antenna pattern in azimuth and its near-50 Ω input impedance. The characteristics of this type of antenna are equivalent to an isolated monopole on an infinite ground-plane [46, 57], which allows application of the theory presented in the previous section. Fig. 2.7 shows the antenna elements and their setup used in the simulations and in the measurements.

Simulations were performed using a method-of-moments (MoM) based simulation tool, [60], in which the antenna elements were accurately modelled and spaced at a
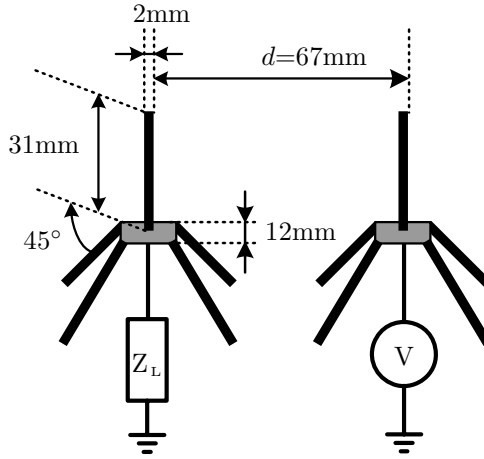
Fig. 2.7: Simulation and measurement setup of two quarter-wavelength drooping radial monopole antenna elements using $d = 0.5\lambda$ and $f = 2250$ MHz.

distance of $d = 0.5\lambda$. One of the elements was passive and was terminated in an impedance that was varied from 0 to j600 Ω, while the other element was driven by a single-frequency voltage signal through a 50-Ω transmission line.

Firstly, the return loss, S_{11}, of the active antenna element was analysed for different reactive terminations of the passive antenna. The results in Fig. 2.8 show that the lowest value for S_{11} is obtained by terminating the passive antenna in an impedance close to j250 Ω. Secondly, Γ, the maximum distortion in the antenna pattern of the active antenna element is analysed for different reactive terminations of the passive antenna. Γ is defined as the difference, in dB, between the maximum and minimum value of the antenna pattern over the entire azimuthal range at a certain elevation angle. Fig. 2.8 shows Γ for different reactive terminations at 0° elevation. A termination close to j250 Ω is seen to minimise Γ in the horizontal plane. The findings from the results above closely agree with the result determined from Eq. (2.16), where the total radiated field is minimised. For an impedance value of j250 Ω, Γ is reduced to less than 0.5 dB.

To investigate the effect of the separation distance, d, on the minimisation of Γ, simulations were performed where d was varied between 0.25λ and 2λ. The parasitic antenna was terminated in either j250 Ω or the system impedance of 50 Ω. The results in Fig. 2.9 show that Γ can be reduced significantly when using the reactive termination, especially at small separation distances. Even for separation distances less than 0.5λ, Γ remains close to 0.5 dB in the case of $Z_L = $ j250 Ω. The results above show that the new method is effective and can be used to obtain a spectacular reduction of the MC effects.
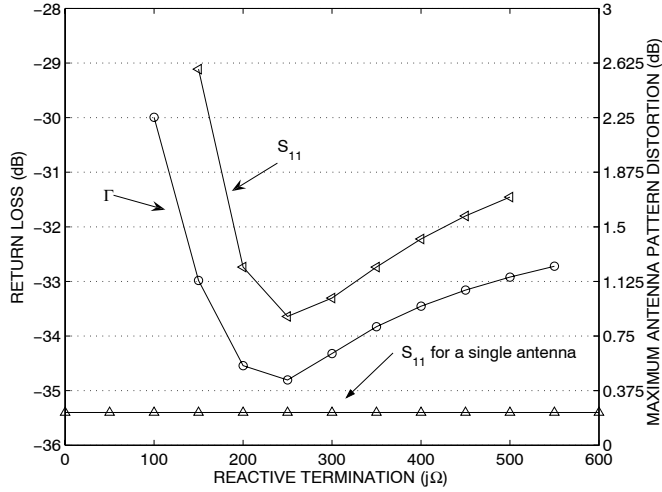
Fig. 2.8: Simulated return loss, S_{11}, at $f = 2250$ MHz, and maximum antenna pattern distortion, Γ, in the horizontal plane of the active antenna, versus the reactive termination, Z_L, of the passive antenna using $d = 0.5\lambda$ and $f = 2250$ MHz.
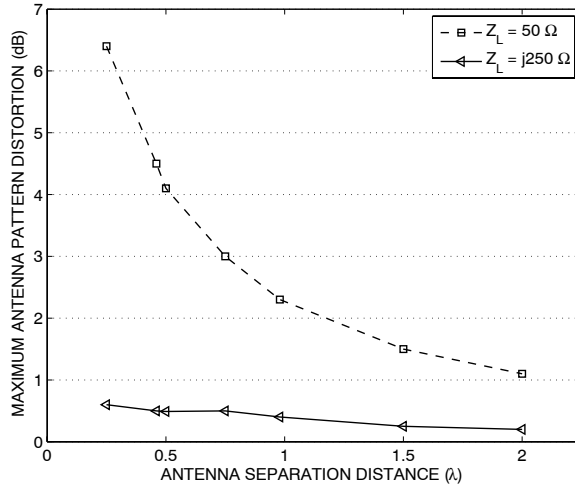
Fig. 2.9: Simulated maximum antenna pattern distortion, Γ, in the horizontal plane of the active antenna versus the antenna separation distance, d, for different terminations of the passive antenna with $f = 2250$ MHz.

The frequency sensitivity of the active antenna in the two-element array was investigated by analysing the antenna pattern at three points in a 100 MHz bandwidth while terminating the parasitic antenna in either j250 Ω or the system impedance of 50 Ω. The results in Fig. 2.10 show that the frequency selectivity that is visible using the 50 Ω termination disappears completely when the parasitic antenna is terminated in j250 Ω.

Although the method above is determined for two separated antenna elements, simulations similar to the ones presented here have shown that in the case of multiple antenna elements, i.e. the 3-D tilted-cross array, the same optimal value for Z_L applies.

Fig. 2.10: Simulated antenna patterns in the horizontal plane of the active antenna element in a two-element antenna array with $d = 0.5\lambda$ at $f = 2200$, 2250 and 2300 MHz using either a 50-Ω or a j250-Ω termination. The amplitude scale is 2 dB/div. Note that for $Z_L = $ j250 Ω, all curves more or less coincide.

2.4.3   Experimental verification

To confirm the concept of mutual coupling reduction by impedance switching, antenna pattern and return loss (S_{11}) measurements were performed in an anechoic chamber with two antenna elements in a configuration identical to that employed in the simulations. In order to limit the required measurement time, only one separation distance was considered, namely $d = 0.5\lambda$. Again, one of the two antenna elements acts as the active element while the other acts as a parasitic antenna and is terminated in either a reactive load or the 50-Ω system impedance. The reactive load was implemented using an open-circuited stub of semi-rigid cable and an SMA-connector. The length of the stub was tuned in an anechoic environment such that the S_{11} parameter of the active element closely matches that of an isolated antenna.

Fig. 2.11 shows measured and simulated results of the S_{11} parameter for a single isolated antenna, and for an active element close to a passive element that was terminated in either the tuned stub or 50 Ω impedance. The results of the tuned stub closely matches that of the isolated antenna. To verify the impedance value of the tuned stub, a network analyser was used and by transforming the measured value using the phase shift in the antenna connectors, a value of j219 Ω was determined, which is close to the optimal value from Fig. 2.8.

Antenna pattern measurements were performed in the horizontal plane, with the passive element terminated in 50 Ω, or using the tuned stub. The results of the measurements presented in Fig. 2.12 show a high level of agreement with the simulation results. The results also show that in the case of the reactive load a reduction of the pattern distortion up to 6 dB and an increase of the return loss of 9 dB at the central frequency can be achieved, as shown in Fig. 2.11. The differences between the measurements and simulations that are still observed in these figures are mainly due to the non-ideal measurement setup and imperfections in the anechoic chamber that cause reflections, which lead to an apparent mismatch of the antenna. It has also been verified that this technique is effective when a combination of two switches is used to alternately load or select elements as would be required in an actual array implementation and therefore this technique was applied to all antenna elements in the 3-D tilted-cross array. The switchboards, shown together with the antenna element in Fig. 2.13, are located directly underneath each antenna.
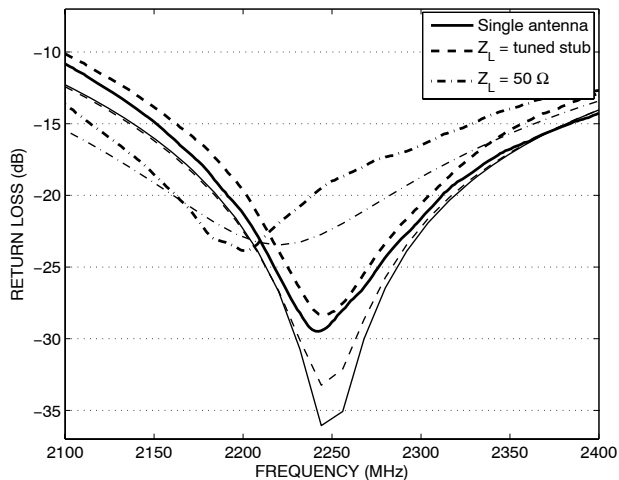
Fig. 2.11: Measured and simulated return loss, S_{11}, versus frequency for a single antenna and for an active antenna element with a passive antenna at 0.5λ distance using the tuned stub and a 50-Ω load. Thick lines represent measurement results, thin lines represent simulation results.

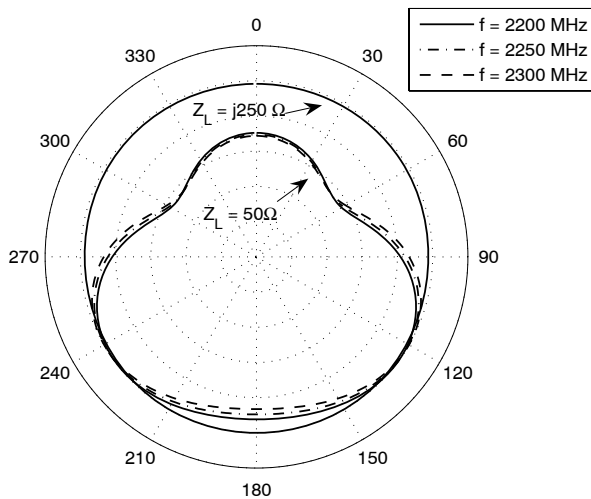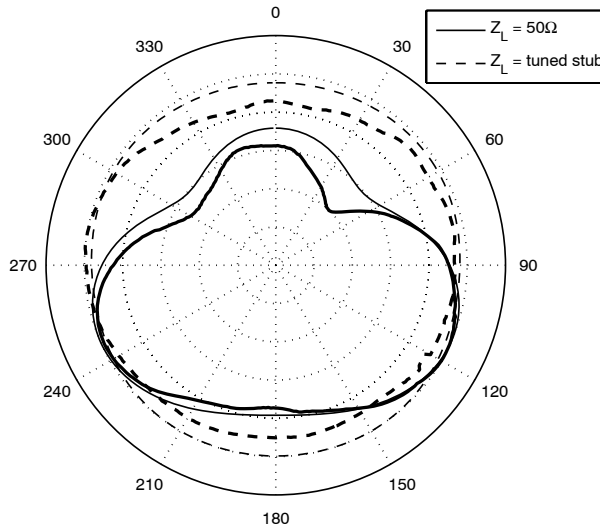Fig. 2.12: Measured and simulated antenna patterns in the horizontal plane of the active antenna element in a two-element antenna array with $d = 0.5\lambda$ at $f = 2250$ MHz using a 50-Ω load and the tuned stub. The amplitude scale is 2 dB/div. Thick lines represent measurement results, thin lines represent simulation results.
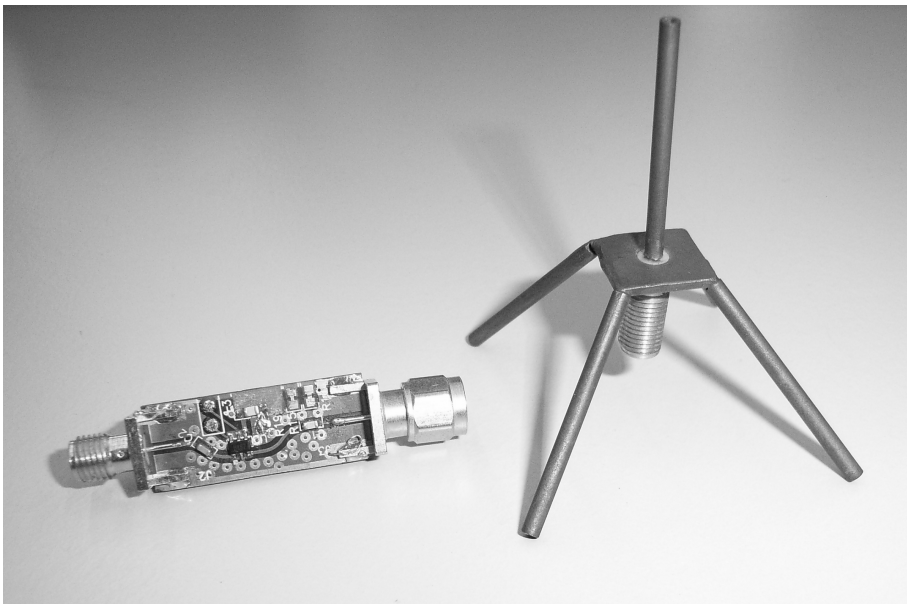
Fig. 2.13: Impedance switchboard (left) and monopole antenna element (right).

2.5   Conclusions

In this chapter, a system was presented to obtain high-resolution AOA estimates of multipath waves in the physically-nonstationary mobile radio channel using a wideband radio channelsounder and a 3-D tilted-cross switched antenna array. Firstly, the design and implementation of the channel sounder were presented, including a method that can successfully compensate for I/Q imbalance.

Secondly, the design and implementation of a novel 3-D switched antenna array are presented. The array can be used for high-resolution AOA estimation in both azimuth and elevation, and the design is a compromise between structures with uniformity and those that would result in better resolution. The array geometry is particularly interesting because it fits perfectly with a recently updated version of the multidimensional Unitary ESPRIT algorithm that will be described in Section 3.3.

To reduce mutual coupling effects caused by the antennas, an impedance switching technique, based on the theory in [54], was evaluated and applied to reduce the mutual coupling effects in switched antenna arrays. The technique encompasses the termination of the passive antenna elements in a suitably chosen reactive termination, that can be determined theoretically by minimising a cost function that describes the re-radiated field in all directions. Results indicate a significant increase in the return loss and in the antenna pattern distortion.

In summary, the main contributions and innovations of the work presented in this chapter are:

- The design and implementation of a wideband radio channel sounder for high-speed characterisation of the radio channel and a 3-D tilted-cross switched antenna array that allows AOA estimations at typical urban speeds (< 50 km/h), as presented in Section 2.2 and 2.3 and previously published by the author in [35–37].

- The presentation, implementation and evaluation of a novel method to reduce the negative effects of mutual coupling in switched antenna arrays, as presented in Section 2.4 and previously published by the author in [37, 38].

3

Multi-dimensional channel parameter estimation

3.1   Introduction

Radio channel parameter estimation is an area which includes the problem of high-resolution angle-of-arrival (AOA) estimation from the outputs of a multidimensional array of antennas. The use of *high-resolution* signal processing techniques is well-known to offer better performance than conventional techniques, such as beamforming [61, 62]. The term high-resolution refers to the ability to accurately resolve two or more closely separated spatial frequencies in a given data set. The most popular estimation techniques can be classified as either subspace-based, e.g. multiple signal classification (MUSIC), estimation of signal parameters via rotational invariance technique (ESPRIT), [63, 64], or maximum-likelihood based, e.g. expectation maximisation (EM), space alternating generalised EM (SAGE), [65].

Maximum-likelihood based techniques are usually superior in terms of performance when both the SNR and the number of snapshots are small and the sources are highly correlated. However, the computational complexity associated with these algorithms is high and increases drastically with multidimensional estimation problems. Iterative maximum-likelihood based algorithms, such as SAGE, overcome these issues and are closely related to subspace based algorithms in that they involve projections onto estimates of the signal space. Observations show that almost equivalent performance can be obtained [66, 67].

Unitary ESPRIT [68] is an efficient and popular subspace-based technique for high-resolution multidimensional AOA estimation. It does not require complicated search or optimisation procedures, as is the case with MUSIC or SAGE, however, it requires antenna elements with identical radiation properties that are spaced uniformly and in a centro-symmetric array geometry. The 3-D tilted-cross array presented in Chapter 2 was specifically designed to possess these properties.

This chapter describes the Unitary ESPRIT algorithm for three-dimensional (3-D) parameter estimation with the application to the 3-D tilted-cross array. Firstly, Section 3.2 introduces the signal model. Secondly, Section 3.3 presents the 3-D Unitary ESPRIT algorithm and an improved version of the 3-D structured-least-squares (3-D SLS) method that solves the rank-deficiency problem that may occur when standard 3-D SLS or other methods are used in combination with crossed arrays. The improved method enables the Unitary ESPRIT algorithm to be applied to the 3-D tilted-cross array and cross arrays in general. Furthermore, a method used for the estimation of the number of signals is presented followed by a numerical technique to reduce the effects of shadowing caused by the antenna array support structure. A summary of the algorithm is given at the end of Section 3.3.

In Section 3.4 numerical results are presented that show the accuracy improvement achieved by using the improved 3-D SLS method. After application of the technique presented in Section 2.4 on page 21 the resolution performance was evaluated using simulations based on either ideal uncoupled antennas or antennas that are influenced by the remaining mutual coupling (MC) between them using method-of-moment (MoM) based simulations. Subsequently, the performance of the estimation of the number of signals is shown. Experimental results are presented in Section 3.5, which show the improvement in estimation of AOAs as a result of the MC and shadowing mitigation techniques described in Chapter 2. Additionally, the ability to identify two closely spaced sources is investigated. Finally, conclusions are drawn in Section 3.6.

3.2   Signal model

As described in Section 2.2.1 on page 11, a pseudonoise (PN) correlation method is used to provide an estimate of the complex impulse response (CIR) of the radio channel between the measurement system transmit and receive antennas. The auto-correlation of the original transmitted PN binary sequence, $a(t)$, with period T and chip duration T_c can be written as

$$x(\tau) = \frac{1}{T} \int_0^T a(t)a(t - \tau)dt, \tag{3.1}$$

where $x(\tau)$ is a periodic function consisting of triangular peaks with a base width of $2T_c$.

Assume that a number, N, of plane waves coming from different azimuth (ϕ) and elevation (θ) angles, arrive at the 31-element 3-D tilted-cross antenna array described

in Section 2.3.1 on page 16. At the mth antenna element, in one of the $R = 3$ linear arrays, each consisting of $M = 11$ elements, the correlation of $a(t)$ with the received signal can be written in complex baseband notation for the ith delay bin $(iT_c, (i+1)T_c)$ as

$$y_m^{(r)}(\tau_i) = \sum_{n=1}^{N^{(i)}} c_n^{(i)} e^{j\left(\frac{2m-1-M}{2}\right)\mu_n^{(i;r)}} x(\tau_i - T_n^{(i)}) + n_m^{(r)}(\tau_i). \tag{3.2}$$

Here, c_n and T_n are the complex amplitude and the relative delay of the nth multi-path wave, respectively and $n_m(\tau_i)$ is an additive white noise signal. All $N - N^{(i)}$, $(N^{(i)} \leq N)$, negligible contributions to the ith delay bin are omitted and τ_i is located randomly within the ith delay bin with uniform probability. The spatial frequency co-efficients for each of the three linear arrays, $\mu_n^{(i;r)}$, $r = 1, 2, 3$, can be determined from the projection of the positions of the antenna elements, $\mathbf{e}_m^{(r)}$, in spherical coordinates

$$\mathbf{e}_m^{(r)}(d_m, \theta_m, \phi_m) = d_m \cos(\theta_m) \cos(\phi_m)\mathbf{e}_x + d_m \cos(\theta_m) \sin(\phi_m)\mathbf{e}_y + d_m \sin(\theta_m)\mathbf{e}_z, \tag{3.3}$$

onto a vector, $\mathbf{k}_n^{(i)}$, shown in Fig. 3.1, that points towards the direction of the incident wave

$$\mathbf{k}_n^{(i)}(1, \theta_n^{(i)}, \phi_n^{(i)}) = \cos(\theta_n^{(i)}) \cos(\phi_n^{(i)})\mathbf{e}_x + \cos(\theta_n^{(i)}) \sin(\phi_n^{(i)})\mathbf{e}_y + \sin(\theta_n^{(i)})\mathbf{e}_z, \tag{3.4}$$

and multiplied with the wave number $\frac{2\pi}{\lambda}$, where λ is the wavelength. For the 3-D tilted-cross array this results in

$$\mu_n^{(i;1)} = \frac{2\pi}{\lambda} \delta \cos \hat{\phi}_n^{(i)} \cos \hat{\theta}_n^{(i)} \tag{3.5}$$

$$\mu_n^{(i;2)} = \frac{2\pi}{\lambda} \delta \sin \hat{\phi}_n^{(i)} \cos \hat{\theta}_n^{(i)} \tag{3.6}$$

$$\mu_n^{(i;3)} = \frac{2\pi}{\lambda} \delta \sin \hat{\theta}_n^{(i)}, \tag{3.7}$$

where δ is the antenna inter-element spacing and $\hat{\phi}_n^{(i)}$ and $\hat{\theta}_n^{(i)}$ should be rotated $45°$ around the x-axis and $35.26°$ around the y-axis, in correspondence to the tilting angles of the array geometry, discussed Section 2.3.1 on page 16, to find $\phi_n^{(i)}$ and $\theta_n^{(i)}$, the true azimuth and elevation angles of the nth impinging wave in the ith delay bin.

In vector notation, the output of the r-th linear array of the 3-D tilted-cross at the ith delay instant is given by

$$\mathbf{y}^{(r)}(\tau_i) = \left[y_1^{(r)}(\tau_i), y_2^{(r)}(\tau_i), \dots, y_M^{(r)}(\tau_i)\right]^T \tag{3.8}$$

$$= \sum_{n=1}^{N^{(i)}} \mathbf{a}^{(i;r)}(\phi_n^{(i;r)}, \theta_n^{(i;r)}) s_n^{(i)}(\tau_i) + \mathbf{n}^{(r)}(\tau_i), \tag{3.9}$$
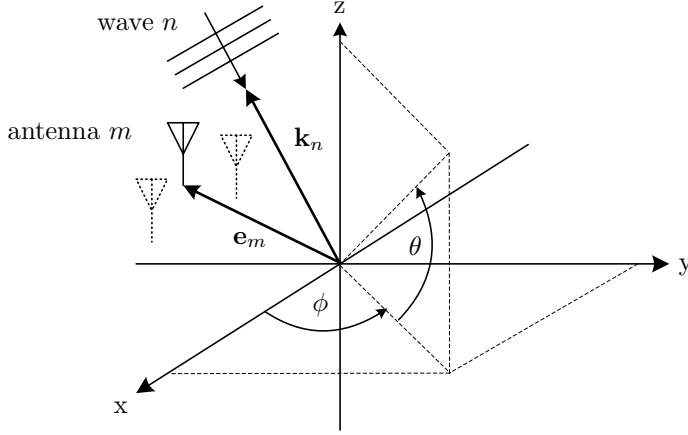
Fig. 3.1: The mth antenna element position given by vector $\mathbf{e}_m$ and the direction of the mth incident wave given by $\mathbf{k}_n$.

where

$$
\begin{aligned}
s_n^{(i)}(\tau_i) &= c_n^{(i)} x(\tau_i - T_n^{(i)}) & (3.10) \\
\mathbf{a}^{(r)}(\phi_n^{(i)}, \theta_n^{(i)}) &= \left[e^{j\left(\frac{1-M}{2}\right)\mu_n^{(i;r)}}, e^{j\left(\frac{3-M}{2}\right)\mu_n^{(i;r)}}, \ldots, e^{j\left(\frac{M-1}{2}\right)\mu_n^{(i;r)}} \right]^T & (3.11) \\
\mathbf{n}^{(r)}(\tau_i) &= \left[n_1^{(r)}(\tau_i), n_2^{(r)}(\tau_i), \ldots, n_M^{(r)}(\tau_i) \right]^T, & (3.12)
\end{aligned}
$$

represent the complex signal value, the array steering vector corresponding to the r-th linear array and the noise vector, respectively. The noise at each element is assumed to have zero mean and variance σ^2, and is assumed to be uncorrelated with the signals and the noise at the other antenna elements.

In matrix notation this can be rewritten for the whole array as

$$
\mathbf{y}(\tau_i) = \mathbf{A}^{(i)}\mathbf{s}^{(i)}(\tau_i) + \mathbf{n}(\tau_i), \tag{3.13}
$$

where

$$
\begin{aligned}
\mathbf{A}^{(i)} &= \left[\mathbf{a}(\phi_1^{(i)}, \theta_1^{(i)}), \mathbf{a}(\phi_2^{(i)}, \theta_2^{(i)}), \ldots, \mathbf{a}(\phi_{N^{(i)}}^{(i)}, \theta_{N^{(i)}}^{(i)}) \right] & (3.14) \\
\mathbf{a}(\phi_n^{(i)}, \theta_n^{(i)}) &= \left[\mathbf{a}^{(1)}(\phi_n^{(i)}, \theta_n^{(i)}), \mathbf{a}^{(2)}(\phi_n^{(i)}, \theta_n^{(i)}), \mathbf{a}^{(3)}(\phi_n^{(i)}, \theta_n^{(i)}) \right]^T & (3.15) \\
\mathbf{s}^{(i)}(\tau_i) &= \left[s_1^{(i)}(\tau_i), s_2^{(i)}(\tau_i), \ldots, s_{N^{(i)}}^{(i)}(\tau_i) \right]^T & (3.16) \\
\mathbf{n}(\tau_i) &= \left[\mathbf{n}^{(1)}(\tau_i), \mathbf{n}^{(2)}(\tau_i), \mathbf{n}^{(3)}(\tau_i) \right]^T. & (3.17)
\end{aligned}
$$

3.3   3-D Unitary ESPRIT

To estimate the AOAs and corresponding powers of waves that impinge on the 3-D tilted-cross array described in the previous chapter, a high-resolution subspace-based algorithm named 3-D Unitary ESPRIT is used [68, 69]. Because Unitary ESPRIT does not require any complicated search or optimisation procedures, as is the case with MUSIC or SAGE, it is a very attractive method in terms of computational complexity, especially for multidimensional problems. The AOAs are estimated by using the shift-invariant structure that is created by dividing each of the three $M = 11$ element linear arrays in the 3-D tilted-cross array into two identical overlapping $M-1$ element subarrays, shown in Fig. 3.2, which requires uniform element spacing.

3.3.1   ESPRIT
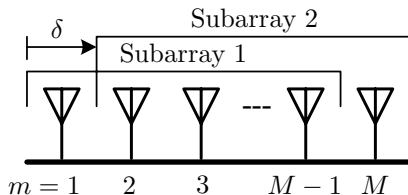
Fig. 3.2: The two overlapping $M-1$ element subarrays, created in each of the three $M = 11$ element linear arrays, that are required for ESPRIT.

The received and correlated signals from the $M - 1$ elements of subarrays 1 and 2 of each of the three orthogonal linear arrays, $r = 1, 2, 3$, at the ith delay instant can be written as

$$\mathbf{y}_1^{(r)}(\tau_i) = \mathbf{J}_1^{(r)}\mathbf{A}^{(i;r)}\mathbf{s}^{(i;r)}(\tau_i) + \mathbf{n}_1^{(r)}(\tau_i) \ \in \mathbb{C}^{M-1} \tag{3.18}$$

$$\mathbf{y}_2^{(r)}(\tau_i) = \mathbf{J}_1^{(r)}\mathbf{A}^{(i;r)}\mathbf{\Phi}^{(i;r)}\mathbf{s}^{(i;r)}(\tau_i) + \mathbf{n}_2^{(r)}(\tau_i) \ \in \mathbb{C}^{M-1}, \tag{3.19}$$

where the shift-invariance structure is described by

$$\mathbf{J}_1^{(r)}\mathbf{A}^{(i;r)}\mathbf{\Phi}^{(i;r)} = \mathbf{J}_2^{(r)}\mathbf{A}^{(i;r)}, \quad r = 1, 2, 3. \tag{3.20}$$

Here, $\mathbf{A}^{(i;r)} \in \mathbb{C}^{M \times N^{(i)}}$ is the array steering matrix for linear array r, corresponding to the r-th set of M rows of $\mathbf{A}^{(i)} \in \mathbb{C}^{3M \times N^{(i)}}$ defined in Eq. (3.14), $\mathbf{s}^{(i;r)}(\tau_i) \in \mathbb{C}^{N^{(i)}}$ represents the signal vector, $\mathbf{n}_1^{(r)}(\tau_i), \mathbf{n}_2^{(r)}(\tau_i) \in \mathbb{C}^{M-1}$ represent the noise vectors of subarray 1 and 2 respectively. Matrices $\mathbf{J}_1^{(r)} \in \mathbb{C}^{(M-1) \times M}$ and $\mathbf{J}_2^{(r)} \in \mathbb{C}^{(M-1) \times M}$ are selection matrices that pick the correct $M-1$ rows of $\mathbf{A}^{(i;r)}$ corresponding to subarray 1 and 2, respectively, of the rth linear array. The phase differences between the two displaced subarrays for each of the three linear arrays are described by the matrix $\mathbf{\Phi}^{(i;r)}$, which is a diagonal matrix with the spatial frequencies $e^{j\mu_n^{(i;r)}}, \quad n = 1 \ldots N^{(i)}$ on its diagonal and zeros elsewhere. The $N^{(i)}$ signal parameters can be determined

by rewriting Eqs. (3.5), (3.6), (3.7), as will be shown later in Eqs. (3.24) and (3.25). As a result, the estimation of the AOAs comes down to estimating $\boldsymbol{\Phi}^{(i;r)}$.

In a similar manner as for other subspace-based algorithms, ESPRIT uses the eigenvalue decomposition (EVD) of the array covariance matrix to find the signal subspace. The covariance matrix corresponding to the ith delay bin, for one of the three linear arrays is given by

$$\mathbf{R}^{(i;r)} = \mathbb{E}\{\mathbf{y}^{(r)}(\tau_i)\mathbf{y}^{(r)H}(\tau_i)\} = \mathbf{A}^{(i;r)}\mathbf{R}_s^{(i;r)}\mathbf{A}^{(i;r)H} + \sigma_{N^{(i)}}^2\mathbf{I}_M \in \mathbb{C}^{M \times M}, \quad (3.21)$$

where $\mathbf{R}_s^{(i;r)} = \mathbb{E}\{\mathbf{s}^{(i;r)}(\tau_i)\mathbf{s}^{(i;r)H}(\tau_i)\} \in \mathbb{C}^{N^{(i)} \times N^{(i)}}$ is the signal covariance matrix. An eigenvalue decomposition of $\mathbf{R}^{(i;r)}$ can be written as

$$\mathbf{R}^{(i;r)} = \left[\begin{array}{cc} \mathbf{U}_s^{(i;r)} & \mathbf{U}_0^{(i;r)} \end{array} \right] \left(\left[\begin{array}{cc} \boldsymbol{\Lambda}_{N^{(i)}}^{(i;r)} & 0 \\ 0 & 0 \end{array} \right] + \sigma_{N^{(i)}}^2\mathbf{I}_{M-1} \right) \left[\begin{array}{c} \mathbf{U}_s^{(i;r)H} \\ \mathbf{U}_0^{(i;r)H} \end{array} \right], \quad (3.22)$$

where the diagonal matrix $\boldsymbol{\Lambda}_{N^{(i)}}^{(i;r)}$ contains the nonzero eigenvalues corresponding to the $N^{(i)}$ incident waves, and the columns of $\mathbf{U}_s^{(i;r)}$ and $\mathbf{U}_0^{(i;r)}$ span the signal and noise subspace, respectively.

Now, let $\mathbf{J}_1^{(r)}\mathbf{U}_s^{(i;r)}$ and $\mathbf{J}_2^{(r)}\mathbf{U}_s^{(i;r)}$ hold the eigenvectors corresponding to the $N^{(i)}$ largest eigenvalues that describe the signal subspace of subarray 1 and 2, respectively. These two sets of eigenvectors span the same $N^{(i)}$-dimensional signal space and are therefore, as in Eq. (3.20), related by an unique nonsingular transformation matrix $\boldsymbol{\Psi}^{(i;r)}$. The transformation between the two bases can be described in the following, so-called invariance equation

$$\mathbf{J}_2^{(r)}\mathbf{U}_s^{(i;r)} = \mathbf{J}_1^{(r)}\mathbf{U}_s^{(i;r)}\boldsymbol{\Psi}^{(i;r)}, \quad r = 1, 2, 3, \quad (3.23)$$

where $\boldsymbol{\Psi}^{(i;r)} = \mathbf{T}\boldsymbol{\Phi}^{(i;r)}\mathbf{T}^{-1}$ and the matrix $\boldsymbol{\Phi}^{(i;r)}$ can be determined from an EVD on $\boldsymbol{\Psi}^{(i;r)}$.

Solving Eq. (3.23) for $\boldsymbol{\Psi}^{(i;r)}$ is the key in ESPRIT and is generally done using least squares (LS), total least squares (TLS) or structured least squares (SLS) methods [70]. After solving the three invariance equations, the AOAs are determined from the spatial frequencies $\mu_n^{(i;r)}$ in $\boldsymbol{\Phi}^{(i;r)}$ as follows

$$\hat{\phi}_n^{(i)} = \arctan\left\{\frac{\mu_n^{(i;2)}}{\mu_n^{(i;1)}}\right\} \quad (3.24)$$

$$\hat{\theta}_n^{(i)} = \arctan\left\{\frac{\mu_n^{(i;3)}}{\sqrt{\left(\mu_n^{(i;1)}\right)^2 + \left(\mu_n^{(i;2)}\right)^2}}\right\}, \quad (3.25)$$

where $\hat{\phi}_n^{(i)}$ and $\hat{\theta}_n^{(i)}$ are rotated versions of $\phi_n^{(i)}$ and $\theta_n^{(i)}$, the true azimuth and elevation angles of the ith impinging waves, respectively, in correspondence to the tilting angles of the array geometry.

3.3.2 Unitary ESPRIT

Since the true covariance matrix $\mathbf{R}^{(i;r)}$ is not available in practical applications it is estimated from a finite number K, of measurement snapshots. An estimated covariance matrix $\hat{\mathbf{R}}^{(i;r)}$ is determined as

$$\hat{\mathbf{R}}^{(i;r)} = \frac{1}{K} \sum_{k=1}^{K} \mathbf{y}^{(r)}(\tau_i; k) \mathbf{y}^{(r)}(\tau_i; k)^H = \frac{1}{K} \mathbf{Y}^{(i;r)} \mathbf{Y}^{(i;r)H}, \qquad (3.26)$$

where the matrix $\mathbf{Y}^{(i;r)} \in \mathbb{C}^{M \times K}$ contains the complex-valued measurement snapshots. To improve the condition of the estimated array covariance matrix and to reduce computational complexity *Unitary* ESPRIT transforms the received and correlated signals from the individual linear arrays to a real-valued representation with incorporated forward-backward (FB) averaging, as discussed in Appendix B. The method transforms the matrix $\mathbf{Y}^{(i;r)}$ to a complex-valued centro-Hermitian matrix that is subsequently transformed into a real-valued matrix $\mathbf{Z}^{(i;r)} \in \mathbb{R}^{M \times 2K}$ of twice its original size [68]. The FB averaging, which is illustrated in Fig. 3.3, doubles the number of complex-valued measurement snapshots by creating a *new* set of snapshots by mirroring the elements with respect to the centre (rotating the columns), flipping the order of the snapshots (rotating the rows) and applying complex conjugation to correct the phase. This proces requires a centro-symmetric data set, which is automatically created by sampling data at the elements of the tilted-cross array geometry.
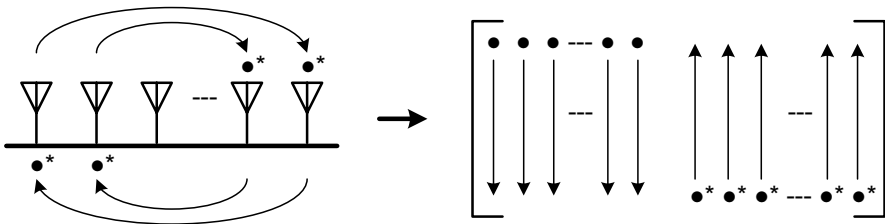
Fig. 3.3: Forward-backward averaging applied to one of the three $M = 11$ element linear arrays, which effectively doubles the number of data snapshots.

Now, the three resulting matrices corresponding to the three linear arrays are combined and stacked to form the composite real-valued snapshot matrix

$$\mathbf{Z}^{(i)} = \begin{bmatrix} \mathbf{Z}^{(i;1)} \\ \mathbf{Z}^{(i;2)} \\ \mathbf{Z}^{(i;3)} \end{bmatrix} \in \mathbb{R}^{3M \times 2K}, \qquad (3.27)$$

in which each of the three linear arrays share the same centre element.

As in Eq. (3.22) and (3.26), the now real-valued signal subspace $\mathbf{E}_s^{(i)}$ is estimated from an EVD on $\mathbf{Z}^{(i)} \mathbf{Z}^{(i)H}$. A real-valued invariance equation, like Eq. (3.23), can now be defined as

$$\mathbf{K}_1^{(r)} \hat{\mathbf{E}}_s^{(i)} \mathbf{\Upsilon}^{(i;r)} \approx \mathbf{K}_2^{(r)} \hat{\mathbf{E}}_s^{(i)}, \quad r = 1, 2, 3, \qquad (3.28)$$

in which $\mathbf{K}_1^{(r)} \in \mathbb{R}^{M-1 \times 3M}$ and $\mathbf{K}_2^{(r)} \in \mathbb{R}^{M-1 \times 3M}$, are known, real-valued matrices obtained from a real-valued transformation of the $(M-1) \times M$ selection matrices $\mathbf{J}_1^{(r)}$ and $\mathbf{J}_2^{(r)}$, which assign the array elements to three pairs of overlapping subarrays [68]. The matrix $\hat{\mathbf{E}}_s^{(i)} \in \mathbb{R}^{3M \times N^{(i)}}$ contains an *estimate* of the real-valued signal subspace with the associated eigenvectors in its columns, which is the reason that Eq. (3.28) may not have an exact solution.

Solving for $\boldsymbol{\Upsilon}^{(i;r)} \in \mathbb{R}^{N^{(i)} \times N^{(i)}}, \quad r = 1, 2, 3$ from Eq. (3.28) is effected in this thesis using an improved 3-D SLS method that will be presented in Section 3.3.3. In order to create *paired* spatial frequency estimates, which is required if more than a single source is incident, a Jacobi-type method to calculate the Simultaneous Schur Decomposition (SSD) is used [71]. The paired complex-valued spatial frequency estimates $\mu_n^{(i;r)}$ can then be obtained from a transformation of the eigenvalues $\omega_n^{(i;r)}$ of $\boldsymbol{\Upsilon}^{(i;r)}$ as $\mu_n^{(i;r)} = 2 \arctan(\omega_n^{(i;r)})$ [68]. Subsequently, the AOAs can be estimated from Eq. (3.24) and (3.25).

Estimates for the corresponding signal powers can be determined from the signal matrix $\mathbf{S}^{(i)} \in \mathbb{C}^{N^{(i)} \times K}$, defined as

$$\mathbf{S}^{(i)} = \left[\mathbf{s}_1^{(i)}(\tau_i), \mathbf{s}_2^{(i)}(\tau_i), \dots, s_K^{(i)}(\tau_i) \right]^T. \tag{3.29}$$

In [69] it is shown that, via a singular-value-decomposition (SVD), $\mathbf{S}^{(i)}$ can be written as

$$\mathbf{S}^{(i)} = \mathbf{T} \mathbf{U}_s^{(i)H} \mathbf{Y}^{(i)}, \tag{3.30}$$

and the array steering matrix can be written as

$$\mathbf{A}^{(i)} = \mathbf{U}_s^{(i)} \mathbf{T}^{-1}, \tag{3.31}$$

which leads to

$$\hat{\mathbf{S}}^{(i)} = \mathbf{A}^{(i)\dagger} \mathbf{U}_s^{(i)} \mathbf{U}_s^{(i)H} \mathbf{Y}^{(i)}, \tag{3.32}$$

where $(\cdot)^\dagger$ denotes the matrix pseudo-inverse. Here, $\mathbf{A}^{(i)} \in \mathbb{R}^{3M \times N^{(i)}}$ contains the array steering vectors, $\mathbf{Y}^{(i)} \in \mathbb{C}^{3M \times K}$ contains the received signals,

$$\mathbf{U}_s^{(i)} = \begin{bmatrix} \mathbf{U}_s^{(i;1)} \\ \mathbf{U}_s^{(i;2)} \\ \mathbf{U}_s^{(i;3)} \end{bmatrix} \in \mathbb{C}^{3M \times N^{(i)}}, \tag{3.33}$$

with $\mathbf{U}_s^{(i;r)} = \mathbf{Q}_M \hat{\mathbf{E}}_s^{(i;r)}$ and $\mathbf{Q}_M$ is defined in Appendix B. From $\hat{\mathbf{S}}^{(i)}$ an estimate for the signal powers can be determined as the diagonal elements of

$$\frac{1}{K} \left[\hat{\mathbf{S}}^{(i)} \hat{\mathbf{S}}^{(i)H} \right]. \tag{3.34}$$

3.3.3 Improved structured-least-squares

The structured-least-squares (SLS) method, [70], is a popular technique for obtaining an approximate solution to Eq. (3.28). Its improvement over the least squares (LS) and total least squares (TLS) methods is based on the explicit acknowledgment that $\hat{\mathbf{E}}_{\mathrm{s}}^{(i)}$ is an imperfect approximation of the true signal subspace, and that an improved estimate can be obtained as

$$\mathbf{E}_{\mathrm{s}}^{(i)} = \hat{\mathbf{E}}_{\mathrm{s}}^{(i)} + \boldsymbol{\epsilon}, \tag{3.35}$$

where $\boldsymbol{\epsilon}$ is an error matrix whose (Frobenius) norm is generally small compared to that of $\mathbf{E}_{\mathrm{s}}^{(i)}$. The method jointly minimises the Frobenius norms of the so-called residual matrices

$$\mathbf{R}^{(i;r)}\big(\mathbf{E}_{\mathrm{s}}^{(i)}, \boldsymbol{\Upsilon}^{(i;r)}\big) = \mathbf{K}_1^{(r)}\mathbf{E}_{\mathrm{s}}^{(i)}\boldsymbol{\Upsilon}^{(i;r)} - \mathbf{K}_2^{(r)}\mathbf{E}_{\mathrm{s}}^{(i)}, \qquad r = 1, 2, 3, \tag{3.36}$$

and the Frobenius norm of $\boldsymbol{\epsilon}$, such that an optimal solution for $\mathbf{E}_{\mathrm{s}}^{(i)}$ is found.

If the antenna elements in the array are positioned in a linear order, as is the case for each of the three arrays in 3-D tilted-cross array, it is possible that two or more wavefronts with different AOAs give rise to the same response on one pair of subarrays. As a result, the matrices $\mathbf{K}_1^{(r)}\mathbf{E}_{\mathrm{s}}^{(i)}$ and $\mathbf{K}_2^{(r)}\mathbf{E}_{\mathrm{s}}^{(i)}$ will be rank-deficient for that pair of subarrays, and the corresponding invariance equations individually will not have $N_{(i)}$ unique solutions. Consequentially, the LS, TLS, SLS or 3-D SLS methods will provide incorrect results.

The problem of rank deficiency in the estimated signal subspace for cross arrays was already pointed out in [72], where a 2-D cross array was considered. Here, the problem was solved by "complexifying" the solutions of both invariance equations such that a simultaneous, unique and paired solution is obtained. This method cannot be applied if a 3-D cross array is considered, as was first pointed out in [73]. Here, it was shown that the problem can be handled by solving a set of non-linear equations, however, this requires the use of additional and more complex numerical techniques.

It was shown in [39] that the 3-D SLS method can be improved by exploiting the observation that the matrices $\boldsymbol{\Upsilon}^{(i;r)}$, $r = 1, 2, 3$, share the same set of eigenvectors if $\hat{\mathbf{E}}_{\mathrm{s}}^{(i)}$ is a perfect estimate of the true signal subspace. As a consequence, the matrices defined by

$$\mathbf{F}^{(i;r,r')}\big(\boldsymbol{\Upsilon}^{(i;r)}, \boldsymbol{\Upsilon}^{(i;r')}\big) = \boldsymbol{\Upsilon}^{(i;r)}\boldsymbol{\Upsilon}^{(i;r')} - \boldsymbol{\Upsilon}^{(i;r')}\boldsymbol{\Upsilon}^{(i;r)}, \quad r = 1, 2, 3, \; r' > r, \tag{3.37}$$

must be null matrices [73].

Taking into account this additional constraint in solving the invariance equations in Eq. (3.28) solves the rank deficiency problem and leads to more accurate estimates.

Following an approach similar to that in [70], the improved 3-D SLS method, referred to as 3-D I-SLS, computes an approximate joint solution to the invariance equations in an iterative procedure, which simultaneously minimises the Frobenius norms of the

three matrices defined by (3.36), the three matrices defined by (3.37), and $\boldsymbol{\epsilon}$. Appropriate weighting factors are used in order to control the expected magnitudes of the entries of the different matrices, as will be discussed below. Key to the minimisation procedure are the vectorisation and linearisation of (3.36) and (3.37), which result in

$$
\begin{aligned}
\text{vec}\big\{\mathbf{R}^{(i;r)}\big(\mathbf{E}_{\text{s},k+1}^{(i)}, \boldsymbol{\Upsilon}_{k+1}^{(i;r)}\big)\big\} &\approx \text{vec}\big\{\mathbf{R}^{(i;r)}\big(\mathbf{E}_{\text{s},k}^{(i)}, \boldsymbol{\Upsilon}_{k}^{(i;r)}\big)\big\} \\
&+ \Big[\mathbf{I}_d \otimes \big(\mathbf{K}_1^{(r)}\mathbf{E}_{\text{s},k}^{(i)}\big)\Big] \text{vec}\big\{\Delta\boldsymbol{\Upsilon}_k^{(i;r)}\big\} \\
&+ \Big[\boldsymbol{\Upsilon}_k^{(i;r)T} \otimes \mathbf{K}_1^{(r)} - \mathbf{I}_d \otimes \mathbf{K}_2^{(r)}\Big] \text{vec}\big\{\Delta\mathbf{E}_{\text{s},k}^{(i)}\big\}
\end{aligned} \quad (3.38)
$$

$$
\begin{aligned}
\text{vec}\big\{\mathbf{F}^{(i;r,r')}\big(\boldsymbol{\Upsilon}_{k+1}^{(i;r)}, \boldsymbol{\Upsilon}_{k+1}^{(i;r')}\big)\big\} &\approx \text{vec}\big\{\mathbf{F}^{(i;r,r')}\big(\boldsymbol{\Upsilon}_{k}^{(i;r)}, \boldsymbol{\Upsilon}_{k}^{(i;r')}\big)\big\} \\
&+ \Big[\boldsymbol{\Upsilon}_k^{(i;r')T} \otimes \mathbf{I}_d - \mathbf{I}_d \otimes \boldsymbol{\Upsilon}_k^{(i;r')}\Big] \text{vec}\big\{\Delta\boldsymbol{\Upsilon}_k^{(i;r)}\big\} \\
&+ \Big[\mathbf{I}_d \otimes \boldsymbol{\Upsilon}_k^{(i;r)} - \boldsymbol{\Upsilon}_k^{(i;r)T} \otimes \mathbf{I}_d\Big] \text{vec}\big\{\Delta\boldsymbol{\Upsilon}_k^{(i;r')}\big\},
\end{aligned} \quad (3.39)
$$

where $\mathbf{E}_{\text{s},k+1}^{(i)} = \mathbf{E}_{\text{s},k}^{(i)} + \Delta\mathbf{E}_{\text{s},k}^{(i)}$ and $\boldsymbol{\Upsilon}_{k+1}^{(i;r)} = \boldsymbol{\Upsilon}_k^{(i;r)} + \Delta\boldsymbol{\Upsilon}_k^{(i;r)}$ are approximations of $\mathbf{E}_{\text{s}}^{(i)}$ and $\boldsymbol{\Upsilon}^{(i;r)}$, respectively, at the $(k+1)$th iteration step, $\otimes$ denotes the Kronecker product and vec$\{\mathbf{R}\}$ denotes a vector-valued function that maps an $M \times N^{(i)}$ matrix $\mathbf{R}$ into an $MN^{(i)}$-dimensional column vector. Further, the vectorised signal subspace error matrix at step $k+1$ is equal to

$$
\text{vec}\big\{\boldsymbol{\epsilon}_{k+1}\big\} = \text{vec}\big\{\mathbf{E}_{\text{s},k}^{(i)} - \hat{\mathbf{E}}_{\text{s}}^{(i)}\big\} + \text{vec}\big\{\Delta\mathbf{E}_{\text{s}^{(i)},k}\big\}. \quad (3.40)
$$

At each step of the iterative procedure, vec$\{\Delta\mathbf{E}_{\text{s},k}^{(i)}\}$ and vec$\{\Delta\boldsymbol{\Upsilon}_k^{(i;r)}\}$, $r = 1, 2, 3$, are obtained by setting the left-hand sides of (3.38), (3.39) and (3.40) to zero, and computing the LS solution to the resulting overdetermined set of linear equations.

The updated versions for vec$\{\Delta\mathbf{E}_{\text{s},k}^{(i)}\}$ and vec$\{\Delta\boldsymbol{\Upsilon}_k^{(i;r)}\}$, $r = 1, 2, 3$ at iteration k can be computed by solving

$$
\begin{bmatrix}
\text{vec}\big\{\mathbf{R}^{(i;1)}\big(\mathbf{E}_{\text{s},k}^{(i)}, \boldsymbol{\Upsilon}_k^{(i;1)}\big)\big\} \\
\text{vec}\big\{\mathbf{R}^{(i;2)}\big(\mathbf{E}_{\text{s},k}^{(i)}, \boldsymbol{\Upsilon}_k^{(i;2)}\big)\big\} \\
\text{vec}\big\{\mathbf{R}^{(i;3)}\big(\mathbf{E}_{\text{s},k}^{(i)}, \boldsymbol{\Upsilon}_k^{(i;3)}\big)\big\} \\
\text{vec}\big\{\mathbf{F}^{(i;1,2)}\big(\boldsymbol{\Upsilon}_k^{(i;1)}, \boldsymbol{\Upsilon}_k^{(i;2)}\big)\big\} \\
\text{vec}\big\{\mathbf{F}^{(i;2,3)}\big(\boldsymbol{\Upsilon}_k^{(i;2)}, \boldsymbol{\Upsilon}_k^{(i;3)}\big)\big\} \\
\text{vec}\big\{\mathbf{F}^{(i;3,1)}\big(\boldsymbol{\Upsilon}_k^{(i;3)}, \boldsymbol{\Upsilon}_k^{(i;1)}\big)\big\} \\
\kappa \cdot \text{vec}\big\{\mathbf{E}_{\text{s},k}^{(i)} - \hat{\mathbf{E}}_{\text{s}}^{(i)}\big\}
\end{bmatrix}
+ \mathbf{Z}
\begin{bmatrix}
\text{vec}\big\{\Delta\boldsymbol{\Upsilon}_k^{(i;1)}\big\} \\
\text{vec}\big\{\Delta\boldsymbol{\Upsilon}_k^{(i;2)}\big\} \\
\text{vec}\big\{\Delta\boldsymbol{\Upsilon}_k^{(i;3)}\big\} \\
\text{vec}\big\{\Delta\mathbf{E}_{\text{s},k}^{(i)}\big\}
\end{bmatrix}
= \mathbf{0}, \quad (3.41)
$$

in which

$$
\mathbf{Z} = [\mathbf{Z}_{*1} \quad \mathbf{Z}_{*2} \quad \mathbf{Z}_{*3} \quad \mathbf{Z}_{*4}] \quad (3.42)
$$

$$\mathbf{Z}_{*1} = \begin{bmatrix} \mathbf{I}_d \otimes \left(\mathbf{K}_1^{(1)}\mathbf{E}_{s,k}^{(i)}\right) \\ \mathbf{0} \\ \mathbf{0} \\ \mathbf{\Upsilon}_k^{(i;2)T} \otimes \mathbf{I}_d - \mathbf{I}_d \otimes \mathbf{\Upsilon}_k^{(i;2)} \\ \mathbf{0} \\ \mathbf{I}_d \otimes \mathbf{\Upsilon}_k^{(i;3)} - \mathbf{\Upsilon}_k^{(i;3)T} \otimes \mathbf{I}_d \\ \mathbf{0} \end{bmatrix} \quad \mathbf{Z}_{*2} = \begin{bmatrix} \mathbf{0} \\ \mathbf{I}_d \otimes \left(\mathbf{K}_1^{(2)}\mathbf{E}_{s,k}^{(i)}\right) \\ \mathbf{0} \\ \mathbf{I}_d \otimes \mathbf{\Upsilon}_k^{(i;1)} - \mathbf{\Upsilon}_k^{(i;1)T} \otimes \mathbf{I}_d \\ \mathbf{\Upsilon}_k^{(i;3)T} \otimes \mathbf{I}_d - \mathbf{I}_d \otimes \mathbf{\Upsilon}_k^{(i;3)} \\ \mathbf{0} \\ \mathbf{0} \end{bmatrix}$$

$$\mathbf{Z}_{*3} = \begin{bmatrix} \mathbf{0} \\ \mathbf{0} \\ \mathbf{I}_d \otimes \left(\mathbf{K}_1^{(3)}\mathbf{E}_{s,k}\right) \\ \mathbf{0} \\ \mathbf{I}_d \otimes \mathbf{\Upsilon}_k^{(i;2)} - \mathbf{\Upsilon}_k^{(i;2)T} \otimes \mathbf{I}_d \\ \mathbf{\Upsilon}_k^{(i;1)T} \otimes \mathbf{I}_d - \mathbf{I}_d \otimes \mathbf{\Upsilon}_k^{(i;1)} \\ \mathbf{0} \end{bmatrix} \quad \mathbf{Z}_{*4} = \begin{bmatrix} \mathbf{\Upsilon}_k^{(i;1)T} \otimes \mathbf{K}_1^{(1)} - \mathbf{I}_d \otimes \mathbf{K}_2^{(1)} \\ \mathbf{\Upsilon}_k^{(i;2)T} \otimes \mathbf{K}_1^{(2)} - \mathbf{I}_d \otimes \mathbf{K}_2^{(2)} \\ \mathbf{\Upsilon}_k^{(i;3)T} \otimes \mathbf{K}_1^{(3)} - \mathbf{I}_d \otimes \mathbf{K}_2^{(3)} \\ \mathbf{0} \\ \mathbf{0} \\ \mathbf{0} \\ \mathbf{I}_{Md} \end{bmatrix}.$$

Here, the factor

$$\kappa = \sqrt{\frac{3M + 3N^{(i)}}{\alpha M}}, \tag{3.43}$$

provides a normalisation that makes the minimisation of $\boldsymbol{\epsilon}$ independent of the dimensions of the other matrices. Further, setting $\alpha > 1$ allows the entries of $\boldsymbol{\epsilon}$ to have larger magnitudes, on average, than the elements of the other matrices and therefore the change in signal subspace, $\Delta\mathbf{E}_{s,k}^{(i)}$, is kept small. In practice, the performance of Unitary ESPRIT is not very sensitive to the exact value of α, and good results are obtained for $\alpha = 10$ [70].

The iterative procedure can be initialised by setting $\mathbf{E}_{s,0}^{(i)} = \hat{\mathbf{E}}_s^{(i)}$ and equating $\mathbf{\Upsilon}_0^{(i;r)}$, $r = 1, 2, 3$, to the LS solutions of (3.28). It was observed from computer simulations that both the 3-D SLS method and the 3-D I-SLS method presented herein require several iterations to converge, and that both methods fail to converge at all in some instances. This latter problem was solved by scaling the updated values vectors $\text{vec}\{\Delta\mathbf{\Upsilon}_k^{(i;r)}\}$, $r = 1, 2, 3$, and $\text{vec}\{\Delta\mathbf{E}_{s,k}^{(i)}\}$ by a constant factor $0 < \beta < 1$, chosen sufficiently small to keep the iterative procedure from "overshooting" the local optimum nearest to the initial solution. The convergence of both the 3-D SLS and 3-D I-SLS method are shown in Fig. 3.4, where simulations are performed with two closely space sources in the rank-deficient case and in the normal case. Here, the total normalised change in signal subspace versus the number of iterations is shown in Fig. 3.4 (a) and the total estimation error versus the number of iterations is shown in Fig. 3.4 (b). The results show that the 3-D I-SLS technique converges within 10 iterations in both cases. The 3-D SLS technique shows a faster convergence, however, the total estimation error shows that the error increases after 10 iterations in the normal case and that the sources cannot be resolved at all in the rank-deficient case.

Although the I-SLS technique described herein is derived for cross arrays with a common phase center, the same technique can also be applied to cross arrays in
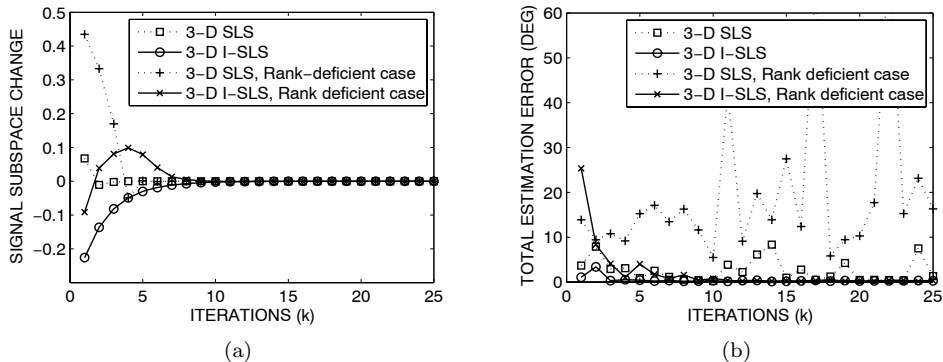
Fig. 3.4: Results of (a), normalised subspace change and (b), total estimation error versus the number of iterations k for the 3-D SLS and the 3-D I-SLS techniques using two closely spaced sources.

general when using standard ESPRIT, e.g. L-shaped geometries, or to any array geometry for which each invariance equation is associated with a linear array, e.g. uniform rectangular frame arrays (URFAs).

3.3.4   Estimation of the number of signals

As in the case of other high-resolution subspace based methods, ESPRIT needs accurate knowledge of the dimension $N^{(i)}$ of the signal subspace in order to perform accurate estimations using the measurement data. A slight overestimation of $N^{(i)}$ is generally preferred in order to include all sources. The estimated power of the additionally overestimated *spurious* sources is usually very low, such that they do not have a significant impact on the results. Finding an estimate, $\hat{N}^{(i)}$, for the signal subspace dimension is not straightforward, because only an *estimate* for the covariance matrix is available.

Techniques based on Akaike information criterion (AIC) and the minimum description length (MDL) criterion are often applied [26]. When the noise statistics are not Gaussian white, the Gerschörin disk estimator (GDE) [74] criterion outperforms AIC and MDL, but its performance is reduced for Gaussian white noise and it requires significantly more computational time.

In [75], a technique was presented that performs better than AIC and MDL in white and especially in colored noise and outperforms GDE in both colored and white noise. It also slightly overestimates the signal subspace dimension, which is preferable in high-resolution signal processing. The method is based on the fact that estimating N is equivalent to finding the number of largest eigenvalues that are associated to the signal subspace and finding the smallest eigenvalues associated to the noise subspace. This can be considered as a classification problem with two classes. The separation

limit between these two classes can be found using discriminant analysis, which is based on finding a set of linear combinations (discrimination functions) of the eigenvalues (discriminant variables), whose values are as close as possible within groups and as far apart as possible between groups. Here, $g_1(n)$ and $g_2(n)$ are the two discriminant functions and represent equivalent probability density functions. The function $g_1(n)$ describes the variation of the last $M-1$ eigenvalues ν_n, sorted in decreasing order, that may belong to the signal subspace as

$$g_1(n) = \frac{\nu_{n+1}}{\sum_{i=2}^{M} \nu_i} \quad n = 1, \ldots, M-1. \tag{3.44}$$

The function $g_2(n)$, corresponding to the noise subspace, has an inverse variation with respect to $g_1(n)$. It is based on the observation that there is a slope variation between the two classes of eigenvalues that can be used to distinguish between the two classes and is defined as

$$g_2(n) = \frac{\zeta_n}{\sum_{i=1}^{M-1} \zeta_i} \quad n = 1, \ldots, M-1. \tag{3.45}$$

Here, $\zeta_n = 1 - \gamma(\nu_n - \kappa_n)/\kappa_n$ mainly measures the relative slope variation of the eigenvalues ν_n that are sorted in a descending order, where $\kappa_\ell = (1/M-\ell)) \sum_{i=n+1}^{M} \nu_i$ is the mean of the next eigenvalues and the value for γ is taken so that $\gamma \max_n[(\nu_n - \kappa_n)/\kappa_n] = 1$.

The technique now proceeds by finding the eigenvalues $\nu_n, \ n = 1, \ldots, N^{(i)}$, of the estimated covariance matrix $\hat{\mathbf{R}}^{(i)}$ that belong to the signal subspace by finding the last positive value of the cost function defined as

$$C_{\text{new}}(n) = g_1(n) - g_2(n), \tag{3.46}$$

and equating $\hat{N}^{(i)}$ to its last argument.

The performance of the technique was investigated in [75] and is also demonstrated in Fig. 3.5 (a), where the discriminant functions are shown for $N = 5$ according to the multipath parameters in Table 3.2 on page 51 that are used later in Section 3.4.3. Fig. 3.5 (b) shows the cost function $C_{\text{new}}(n)$ that correctly identifies $\hat{N} = 5$.

In the case that $\hat{N} > N$, the additional and falsely estimated sources caused by overestimating the signal subspace dimension can be removed using the unique relationship between the spatial frequencies, $\mu_n^{(i;r)}$, of the tilted-cross geometry determined from the squared sum of Eq. (3.5), (3.6) and (3.7) presented on page 33 as follows

$$\xi_n^{(i)} = \left(\mu_n^{(i;1)}\right)^2 + \left(\mu_n^{(i;2)}\right)^2 + \left(\mu_n^{(i;3)}\right)^2 - \left(\frac{2\pi}{\lambda}\delta\right)^2, \tag{3.47}$$

where $\xi_n^{(i)}$ represents a *reliability* indicator that should ideally approach zero. The falsely estimated nth source in the ith delay-bin is removed when the following criterion is fulfilled
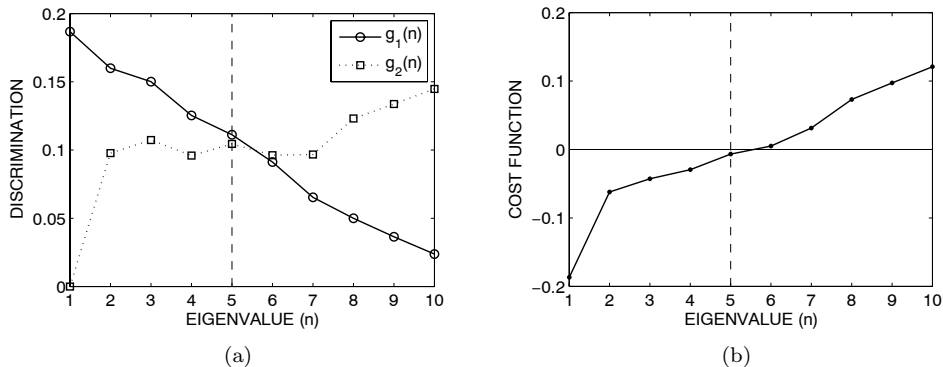
$$|\xi_n^{(i)}| > t_{rel}, \tag{3.48}$$

Fig. 3.5: Results of (a), discriminant functions $g_1(n), g_2(n)$ and (b), cost function $C_{\text{new}}(n)$ for $N = 5$ ($\hat{N} = 5$) according to multipath parameters discussed later in Table 3.2 on page 3.2.

where t_{rel} represents the reliability threshold. The value for t_{rel} determines the maximum estimation error that is tolerated to detect only spurious or unreliable estimates, such that they can be removed from the final results. Good results are obtained for $0.5 < t_{rel} < 3$.

3.3.5   Shadowing reduction

Although flexible absorber material is applied to the array support structure to prevent scattering and MC effects, it additionally causes shadowing of the radio waves incident on the array. This shadowing effect is worst in three different scenarios, in each of which, one of the three 11 element linear antenna arrays is shadowed by its own support structure. This occurs close to $\phi \approx 60°, 180°/-180°, -60°$. To avoid this problem, a selection scheme was developed that discards the erroneous data from the shadowed elements for a wave incident in these areas. This can be done with minimum loss of performance since the data from the array that is discarded in the processing has a low contribution to the total array aperture in this angular area and two instead of three linear arrays will still lead to reliable estimates. This is summarised in Table 3.1. Here, the largest shadowing effect and the lowest aperture, with respect to the spatial frequencies corresponding to each of the three linear arrays, is shown for the three distinct areas. It also shows the best combination of two array arms in terms of maximum aperture for the three areas. The spatial frequency estimates themselves can be used to select the correct set for the estimation. The array that is shadowed corresponds to the lowest aperture and therefore, in theory, generates the lowest spatial frequency. Taking the two largest spatial frequency estimates will therefore result in a better estimation performance in the case of shadowing by the structure. For example, when waves are incident close to $\phi \approx 180°$, shadowing can cause an erroneous estimate of $\mu^{(1)}$. As a result Eq. (3.24) and (3.25) on page

Table 3.1: Selection scheme for the best combination of spatial frequencies corresponding to the largest aperture and suffering from the lowest shadowing in the three distinct azimuth areas of the 3-D tilted-cross antenna array.

$\phi \approx$	$60°$			$180/-180°$			$-60°$		
	$\mu^{(1)}$	$\mu^{(2)}$	$\mu^{(3)}$	$\mu^{(1)}$	$\mu^{(2)}$	$\mu^{(3)}$	$\mu^{(1)}$	$\mu^{(2)}$	$\mu^{(3)}$
Largest shadowing	-	-	x	x	-	-	-	x	-
Lowest aperture	-	-	x	x	-	-	-	x	-
Best combination	x	x	-	-	x	x	x	-	x

36 will generate wrong results. Since $\mu^{(1)}$ hardly contributes to the total aperture in this area, using only $\mu^{(2)}$ and $\mu^{(3)}$ will lead to an improved estimate for ϕ and θ as follows

$$\hat{\phi} = \arctan\left\{ \frac{\mu^{(2)}}{\mu^{(3)}} \right\} \tag{3.49}$$

$$\hat{\theta} = \arccos\left\{ \frac{\sqrt{\left(\mu^{(2)}\right)^2 + \left(\mu^{(3)}\right)^2}}{\frac{2\pi\delta}{\lambda}} \right\}, \tag{3.50}$$

where $\hat{\phi}$ and $\hat{\theta}$, are rotated versions of ϕ and θ, the true azimuth and elevation angles of the impinging wave respectively, in correspondence to the tilting angles of the two linear arrays in the resulting 2-D cross geometry. Similar equations can be determined using combinations of $\mu^{(1)}$ and $\mu^{(2)}$ or $\mu^{(1)}$ and $\mu^{(3)}$. To determine whether estimates are unreliable and the shadowing reduction method should be applied, the reliability indicator $\xi_n^{(i)}$ is used.

3.3.6   Summary of the algorithm

In this section the method of obtaining high-resolution AOA estimates from snapshot data measured at the elements of a 3-D tilted-cross array is summarised. After digitising the received and down-converted complex baseband signals at each of the 31 antenna elements, the algorithm proceeds as follows.

1. Correlate the digitised complex signals with a local replica of the original transmitted PN sequence to form the CIRs that are stored in the measurement snapshot matrix $\mathbf{Y}^{(i;r)} \in \mathbb{C}^{M \times K}$, $i = 0, 1, \ldots$, $k = 1, 2, \ldots, K$, $r = 1, 2, 3$.

   For each ith delay interval:

2. Perform FB averaging and real-valued transformation on the measurement snapshot data, as described in Appendix B, to form the composite real-valued snapshot matrices $\mathbf{Z}^{(i;r)}$ and the composite snapshot matrix $\mathbf{Z}^{(i)} \in \mathbb{R}^{3M \times 2K}$, shown in Eq. (3.27) on page 37.

3. Find an estimate for $N^{(i)}$ by finding the last positive value of the cost function $C_{\text{new}}(n)$ described in Eq. (3.46) on page 43.

4. Estimate the signal subspace $\mathbf{E}_s^{(i)}$ from an EVD on $\mathbf{Z}^{(i)}\mathbf{Z}^{(i)H}$.

5. Solve Eq. (3.28) on page 37 for $\boldsymbol{\Upsilon}^{(i;r)} \in \mathbb{R}^{N^{(i)} \times N^{(i)}}$, $r = 1, 2, 3$ using the 3-D I-SLS method presented in Section 3.3.3 on page 39.

6. Determine the spatial frequency estimates $\hat{\mu}_n^{(i;r)}$ as the eigenvalues of $\boldsymbol{\Upsilon}^{(i;r)}$.

7. Detect falsely estimated sources using the reliability criterion in Eq. (3.48) on page 43 and a value for $0.5 < t_{rel} < 3$.

8. Apply the shadowing reduction method presented in Section 3.3.5 on page 44 by discarding erroneous $\hat{\mu}_n^{(i;r)}$ and determine improved AOA estimates using formulas similar to Eqs. (3.49) and (3.50) on page 45.

9. Remove any remaining falsely estimated sources detected in step 7 that could not be improved by step 8.

10. For the remaining estimated sources that are not detected in step 7 determine the AOAs according to Eqs. (3.24) and (3.25) on page 36 and rotate $\hat{\phi}_n^{(i)}$ and $\hat{\theta}_n^{(i)}$ in correspondence to the tilting angles of the array geometry.

11. Determine the signal powers as the diagonal elements of $\frac{1}{K}\left[\hat{\mathbf{S}}^{(i)}\hat{\mathbf{S}}^{(i)H}\right]$.

3.4   Numerical results

3.4.1   Accuracy

In this section the accuracy of the estimation algorithm in combination with the 3-D cross array is analysed to verify the performance of the 3-D I-SLS method in conjunction with multidimensional Unitary ESPRIT. Simulations were performed assuming use of a *non-tilted* 3-D cross array, for a more clearer analysis of the rank-deficient-case as described in Section 3.3.3 on page 39. A number of repetitive simulations (trails) were performed in order to determine the root-mean-square (RMS) estimation error. In the simulations the RMS error was computed from $Q = 1000$ independent trials as

$$\text{RMSE}_n = \sqrt{\frac{1}{Q}\sum_{q=1}^{Q}\sum_{r=1}^{3}\left|\hat{\mu}_{n,q}^{(r)} - \mu_n^{(r)}\right|^2}, \quad n = 1, \ldots, N, \qquad (3.51)$$

where $\mu_n^{(r)}$, $r = 1, 2, 3$, are the known and $\hat{\mu}_{n,q}^{(r)}$ are the estimated spatial frequencies of the nth signal obtained in the qth trial. In the simulations, 10 iterations are used in both the 3-D SLS and 3-D I-SLS procedure to obtain a stable result for the signal subspace, as described in Section 3.3.3 on page 42.

Fig. 3.6 shows the RMS estimation error as a function of signal-to-noise ratio (SNR) for $N = 2$ equally powered waves impinging from +4 and -4 degrees azimuth respectively, i.e., half the Rayleigh resolution limit, and zero elevation. The SNR was varied from -15 to 15 dB and the number of snapshots $K = 100$. The Cramer Rao Bound (CRB) is plotted as a reference in Fig. 3.6, according to expressions presented in [76, Eq. (33)]. Since the two sources are located symmetrically compared to the array geometry, their performance is identical and the result for only one source is presented here.

The results of the LS, TLS and 3-D SLS methods show a large constant RMS error that increases below a SNR value of -5 dB. This large error is caused by the inability of the algorithms to resolve the two sources, due to rank deficiencies occurring in the invariance equations associated with the x- and z-axes of the array, as discussed in Section 3.3.3 on page 39. In Fig. 3.6 it is shown that the 3-D I-SLS method presented herein leads to successful resolution, which results in a lower RMS error that follows the CRB for SNR values higher than -5 dB.

Fig. 3.6: RMS estimation error for either source 1 and 2 as a function of SNR for two equally powered wavefronts impinging from ±4 degrees azimuth and zero elevation.

Fig. 3.7 shows the RMS estimation error as a function of SNR for $N = 2$ equally powered waves impinging from +4 and -4 degrees azimuth respectively and from 0 and 10 degrees elevation. It is interesting to observe that, although theoretically rank deficiency does not occur in this case, the new method still outperforms the other methods due to the additional constraint in Eq. (3.37).
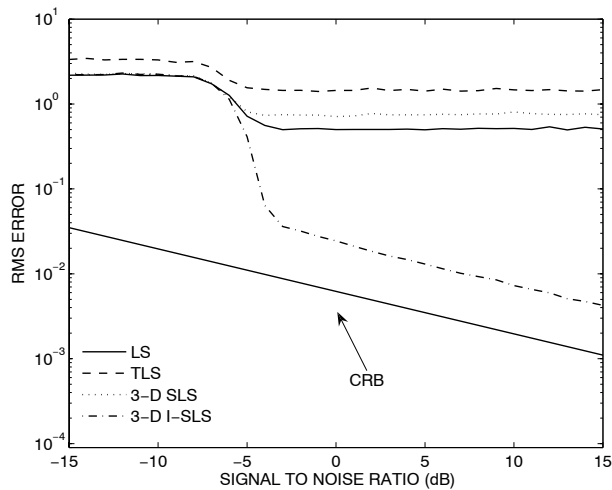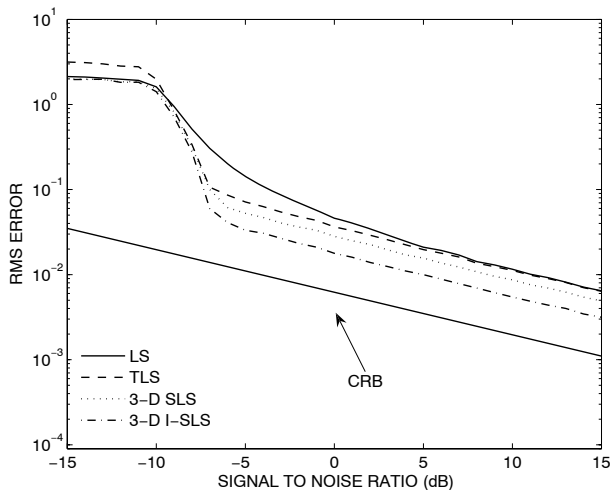
Fig. 3.7: RMS estimation error for source 1 as a function of SNR for two equipowered wavefronts impinging from ± 4 degrees azimuth and 0 degrees elevation. Similar results are obtained for source 2 positioned at 10 degrees elevation.

3.4.2   Resolution

Results of computer simulations of the performance of the Unitary ESPRIT algorithm applied to the 3-D tilted-cross array geometry are presented in this section. The resolution threshold of the system is an important performance measure. It is defined as the SNR below which two equipowered multipath waves (a and b), separated in the angular domain by $\Delta\phi_{a,b}$ degrees, can no longer be "resolved". Here, $\Delta\phi_{a,b}$ defines the resolution of the system, a design goal that was set to be better than $5°$ in Section 2.3 on page 16. In order to use the definition of resolution with parameter-based estimation techniques such as Unitary ESPRIT, the following null hypothesis is used:

Null hypothesis   *Two sources a,b that are estimated by the system are different.*

To test this hypothesis, Monte-carlo simulations need to be performed to determine the maximum RMS angular estimation error of sources a and b, $\max(\mathrm{RMSE}_{a,b})$, at a certain SNR level. Then, two sources a, b that are estimated by the system are different if the null hypothesis cannot be "disproved" statistically with more than 50% probability, i.e.

$$\mathbb{P}_{\mathrm{resolution}}\left\{2\max(\mathrm{RMSE}_{a,b}) < \Delta\phi_{a,b}\right\} > 50\%. \tag{3.52}$$

The 50% confidence level angular resolution in Eq. (3.52) represents twice the angular radius of a circle, circumventing the real sources, that contains 50% of the estimates of

one of the sources. This confidence level is chosen with the assumption that exactly at the resolution threshold threshold the estimated sources either fall inside or outside the circle with 50% probability. It should be noted that this approach is used in a similar way for the determination of angular resolution in other fields, e.g. astrophysics [77].

The SNR is defined as in [26] as

$$\text{SNR}_{1,2}^{(i)} = \frac{1}{\sigma^2 T_c} \int_{iT_c}^{(i+1)T_c} |s_{1,2}^{(i)}(\tau)|^2 d\tau, \tag{3.53}$$

where σ^2 represents the noise variance, T_c is the delay bin duration and $s_{1,2}^{(i)}(\tau)$ is the received signal amplitude due to radiation from source 1 or source 2.

Fig. 3.8 shows simulated resolution threshold values versus the angular separation in both azimuth and elevation for two sources with equal power arriving close to $(\theta = 0°, \phi = 0°)$ at the same delay instance. Simulations were performed with $K = 10$ and 20 snapshots, using the 3-D tilted-cross antenna array configuration with the antenna elements modelled as being infinitely small and having omnidirectional antenna patterns in both azimuth and elevation. The phase difference between the two multipath signals was fixed at $\pi/2$. Each of the simulated threshold values was based on 100 independent trials for each separation until the minimum was found. As ex-
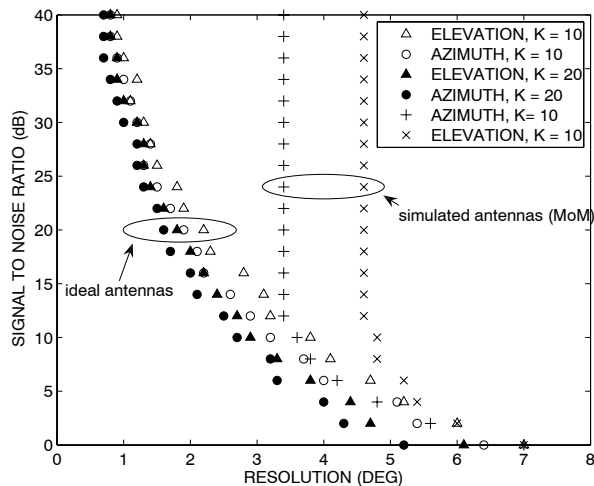
Fig. 3.8: Simulated resolution thresholds for Unitary ESPRIT applied to the 3-D tilted-cross array. Simulated thresholds are based on 100 independent trails.

pected, the results in Fig. 3.8 show that resolution threshold improves with increasing SNR values. Resolution also improves if a better estimate of the covariance matrix is available. This can be achieved by increasing the number of snapshots, K, but this is more effective at low SNR values. Increasing K also increases the measurement duration and decreases the speed at which measurements can be performed, which

means a trade-off has to be made in choosing K. It was found from simulations that at SNR = 10 dB further increasing K above a value of 10 does not contribute significantly to the resolution performance, therefor K was set to $K = 10$ for all the analyses. The results in Fig. 3.8 also show that the resolution performance in elevation is close to that of azimuth. The small differences can be explained by the fact that the aperture in elevation is slightly reduced due to the tilting of the structure. By using a method-of-moments simulation tool, [60], the antennas, the impedance switching method described in Section 2.4 on page 21 and the antenna array support structure were accurately modelled, and it was found that the best azimuth and elevation angle resolutions were constant for SNRs > about 10 dB and were slightly above 3.5 degrees and slightly below 5 degrees, respectively.

Simulations presented in Fig. 3.9 (a) show that the resolution performance in both elevation and azimuth is quite uniform in the entire azimuth range, therefore, the results presented in Fig. 3.8 are representative of the resolution capability over the entire azimuth range and for a large part of the elevation range. The elevation resolution along the elevation range, shown in Fig. 3.9 (b), is the best at low absolute elevation angles, which fulfils the initial design criteria, discussed in Section 2.3 on page 16, and increases up to maximum 8 degrees at larger elevation angles. The azimuth resolution along the elevation range, also shown in Fig. 3.9 (b), is also the best at low absolute elevation angles, but it should be noted that the change in the azimuth resolution along the elevation range is mainly caused by the spherical coordinate system, e.g. at $\theta = 60°$ the absolute angle in azimuth is doubled compared to that at $\theta = 0°$.

(a)   (b)

Fig. 3.9: Simulated resolution thresholds along (a) the azimuth range at $\theta = 0°$ and (b) the elevation range at $\ph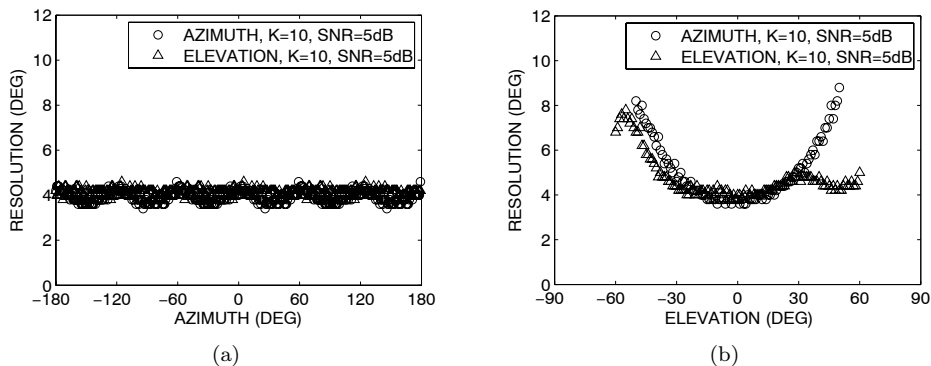i = 0°$ for Unitary ESPRIT applied to the 3-D tilted-cross array. Simulated thresholds are based on 100 independent trails, $K = 10$ snapshots and SNR = 5 dB.

Table 3.2: Theoretical and estimated multipath parameters.

	θ (deg)	ϕ (deg)	SNR (dB)	$|\xi|$
	45.00	150.00	25.00	-
	15.00	75.00	20.00	-
Theory	0.00	0.00	15.00	-
	-15.00	-75.00	10.00	-
	-45.00	-150.00	5.00	-
	45.02	150.12	24.90	0.01
$\hat{N} = 3$	15.09	75.04	20.01	0.00
	-0.11	-0.34	15.03	0.02
	44.94	149.98	25.01	0.01
	15.00	74.75	20.07	0.03
$\hat{N} = 5$	-0.06	0.02	15.10	0.03
	-14.95	-75.04	9.89	0.02
	-44.83	-149.69	5.45	0.07
	44.50	150.98	24.80	0.34
	14.87	73.41	19.61	0.01
	-0.39	-0.94	14.73	0.07
$\hat{N} = 7$	-14.67	-75.37	9.84	0.05
	-44.82	-150.85	7.41	0.01
	-29.70	26.68	-3.17	7.52
	18.74	138.91	-8.01	5.60

3.4.3 Estimation of number of signals

To illustrate the effect of over- and underestimation of N on the AOA estimation, a scenario of five incident waves was simulated. In Table 3.2, the theoretical ($N = 5$) and estimated parameters of the signals are presented including the values for the reliability indicator $|\xi|$. Note that the maximum number of resolvable waves is 10, as described in Section 3.3. As expected, an underestimation of N leads to the vanishing of the weakest multipath contributions, whereas an overestimation leads to spurious estimation results that have a power below the noise level. Furthermore, the reliability indicator $|\xi|$ clearly identifies the falsely detected multipath contributions and supports the use of the criterion described in Section 3.3.4 on page 42 to detect the number of sources.

3.5   Experimental results

In this section results are presented of measurements performed in different controlled lab environments using the 3-D tilted-cross antenna array.

3.5.1   Shadowing and mutual coupling reduction

Continuous-wave (CW) measurements were performed at the David Florida Laboratory (DFL) in Canada in order to investigate the effects of shadowing and scattering by the antenna array support structure, as well as the effect of MC between the antenna elements, on the direction finding accuracy. During these measurements the antenna array was set-up in a half-open anechoic measurement chamber, was fixed on a turn-table and connected to a receive system that was capable of sequentially recording data from all antenna elements. The transmitter was positioned outside, at a distance of approximately 400 m away from the receiving array, in order to create a plane-wave scenario. Measurements were performed in three consecutive steps between $-20° < \theta < 20°$ and the entire azimuth range ($-180° < \phi < 180°$). The recorded measurement data were then used as input to the Unitary ESPRIT algorithm to estimate AOAs of the incident waves.
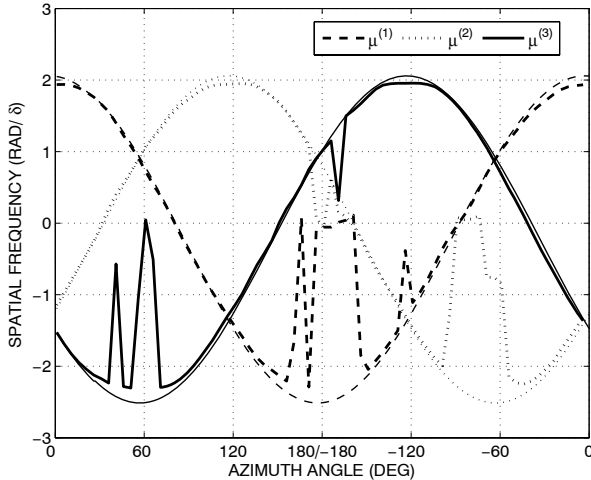
Fig. 3.10: Spatial frequency estimates determined from either simulations, represented in thin lines and from measurements, represented in thick lines

The results presented in Fig. 3.10 show the theoretical and the estimated spatial frequencies resulting from the measurements for $\theta \simeq 5°$. The MC reduction technique presented in Section 2.4 was applied, but the shadowing reduction scheme presented in Section 3.3.5 was not. The effect of the shadowing by the structure can clearly

be observed at $\phi \simeq 60°, 180°/-180°, -60°$. In Fig. 3.11 the absolute estimation error in the azimuth and elevation direction, averaged over the three consecutive measurements are shown. Here, the effects of MC and shadowing and the reduction that is obtained can more clearly be observed. The results show that the impedance switching technique reduces the angular estimation error, although some errors remain in the three distinct areas which coincide with regions where subsequently one of the three antenna arms is shadowed by the antenna support structure.

Fig. 3.11: Estimation error for azimuth and elevation obtained from the analysis of the measurement data. Here, o represents standard operation, + represents MC reduction and * represent shadowing reduction combined with MC reduction.

To circumvent the shadowing effects, the method described in Section 3.3.5 on page 44 was used. The results show a significan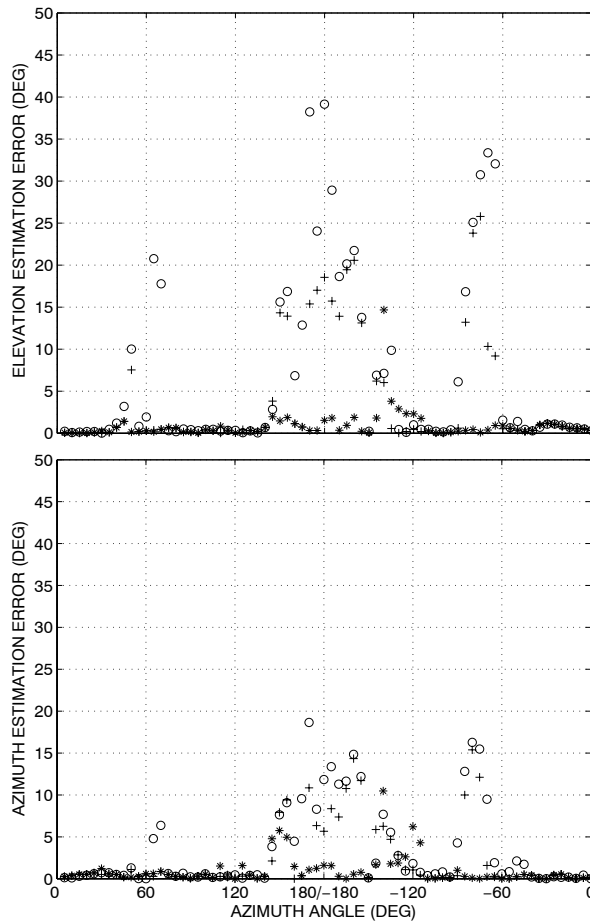t improvement in estimation, although some errors remain visible. Additional measurements have shown that the remaining errors can be reduced by applying better absorbing and shielding material to the antenna switching board. The results presented and explained in Section 3.5.2 were performed after applying the shielding and absorber material.

3.5.2   Multiple source detection

Measurements were performed in a controlled lab environment at the TU/e in Eindhoven, the Netherlands to investigate the ability of the system to detect multiple sources that are incident on the array in a single delay bin. In this measurement setup the entire measurement system from transmitter to receiver was used instead of the CW-method described in the previous section. The lab environment consisted of a 6 by 8 m room that was largely covered with RF-absorbing material. Firstly, a verification measurement was performed using a single transmit antenna, similar to the drooping radial monopole antennas presented in Section 2.4 on page 21, that was aligned using lasers at $\theta = 0°, \phi = 0°$. Secondly, two transmitting antennas were connected to the transmitter using a power spitter. To decorrelate the signals from the two sources, which are each applied to both antennas, different cable lengths were used. The receiving 3-D tilted-cross antenna array was positioned in a more or less random orientation at a distance of 6.2 m from the two transmitting antennas, which were separated by 3.1 m and positioned at slightly different heights. Although the source antennas are closely spaced, their spacing remained greater than that which would lead to AOAs closer in separation than the angular resolution threshold of the system.
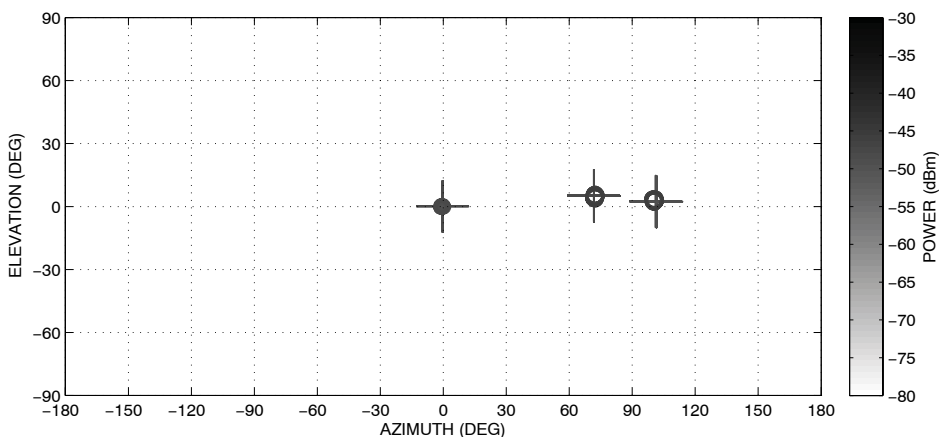

Fig. 3.12: Results of measurements and simulations, represented by o and + respectively, in which a single source was positioned at $\theta = 0°, \phi = 0°$ and two closely spaced sources were positioned at a semi-rondom position.

A configuration, such that the resolution threshold could be determined was not possible due to the limited amount of space in the room, to put the receiver at a larger distance from the sources, and due to the increased signal correlation, which would occur when spacing the source antennas more closely. The results of both measurements are presented in Fig. 3.12, including the results of simulations using the same setup. The results show the excellent identification of the single source at $\theta = 0°, \phi = 0°$. The two sources arriving in the same delay bin are also detected and show good agreement with the simulation results.

3.6   Conclusions

In this chapter, a method was described to obtain high-resolution AOA estimates of multipath waves on physically-nonstationary mobile radio channels using a wideband radio channel sounder and a 3-D tilted-cross switched antenna array. An improved 3-D structured-least-squares (3-D I-SLS) method was described that enables the Unitary ESPRIT algorithm to be applied to the important category of cross arrays. The new method is based on an iterative minimisation procedure similar to that of the 3-D SLS method, but improves upon the 3-D SLS method by requiring the solutions of the invariance equations to share a common set of eigenvectors. The 3-D Unitary ESPRIT algorithm with improved 3-D SLS method was applied to obtain accurate AOA estimations in both azimuth and elevation. The problem of the estimation of the number of signals was solved by applying a method described in [75]. To minimise the shadowing effects of the support structure a method was presented to improve estimation accuracy in the shadowed areas.

The results show that the delay and angular characteristics of incident waves in both azimuth and elevation can be characterised with high resolution. The best azimuth and elevation angle resolutions were constant for SNRs > about 10 dB and were slightly above 3.5 degrees and slightly below 5 degrees, respectively.

In summary, the main contributions and innovations of the work presented in this chapter are:

- A new method to apply 3-D Unitary ESPRIT to the specific category of cross arrays, as presented in Section 3.3.3 and previously published by the author in [39].

- To minimise the effects of shadowing of the antenna array support structure a method was presented to detect and discard erroneous data with minimal loss of performance using a unique reliability criterion. This result was presented in Section 3.3.4 and 3.3.5 and previously published by the author in [36].

- Theoretical and experimental results support the validity of the measurement method and show that multiple sources can be accurately characterised with a resolution performance of less than 5° in both azimuth and elevation.

4

Angle-of-arrival measurement results

4.1 Introduction

The previous two chapters described a method for the estimation of the AOAs of multipath waves with high-resolution and under mobile conditions. Results obtained from simulations and measurements in anechoic chambers and lab-conditions demonstrated that the measurement system and analysis software are capable of estimating the AOAs of incoming waves with high resolution. In order to further verify the performance and to demonstrate that it can be used to identify dominant propagation mechanisms in real-world environments, the measurement equipment was installed in a vehicle, together with additional equipment, and a number of outdoor experiments were performed.

In this chapter, a selection of the results of several outdoor experiments will be presented. Firstly, Section 4.2 describes the additional equipment that is used during the measurements. In particular, the use of an omnidirectional video camera, which helps to identify sources of scattering, reflection or diffraction from the measurement data are reported. Secondly, Section 4.3 presents the results of experiments performed in a rural environment. Results are presented of a measurement in which the receiver is moved along a straight trajectory towards and away from the transmitter. Besides showing that the AOAs of the LOS component are estimated correctly, an attempt is made to estimate the ground reflection. Furthermore, measurements along a circular trajectory are presented to show that the performance is uniform in the azimuth

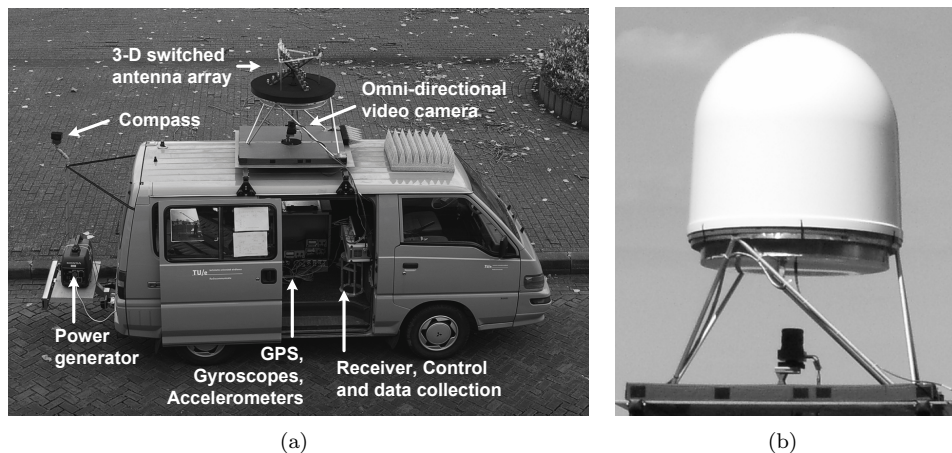(a)   (b)

Fig. 4.1: Photograph of (a) the measurement and auxiliary equipment installed in and on the measurement vehicle and (b) the antenna array covered with a radome.

domain at low elevation angles.

In Section 4.4, experiments in an urban environment are presented where the transmitter is positioned either above or below rooftop. The receiver is moved along different trajectories in LOS and non-LOS scenarios. It is shown that besides specular reflections, scattering or diffraction by irregular and rough surfaces and through-building propagation can cause dispersion of the received waves in the angular and delay domain. Finally, conclusions are drawn in Section 4.5.

4.2   Auxiliary equipment

The control and receiving equipment of the measurement system, described in Chapter 2, were installed in a measurement vehicle together with additional auxiliary equipment, as shown in Fig. 4.1 (a). Electric power for the system is provided by a small generator mounted outside, at the back of the vehicle. The 3-D antenna array is mounted on top of the vehicle at a height of 3.5 m, measured from the centre of the array, and is covered by a radome for protection, as shown in Fig. 4.1 (b).

The radome is manufactured out of two types of dielectric material [78]. The first, the outer material, provides UV and environmental stability. The second internal material is responsible for the mechanical stability. In order to reduce the losses, the radome thickness is as thin as possible, between 2-3 mm. The radome was initially characterised by the manufacturer within the Ku Band (10-15 GHz), where a maximum loss of 0.7 dB and a minimal loss of 0.4 dB were found. The loss tangent of the material was estimated from measurements to be in the order of $\tan\delta = 0.001$ and the relative permittivity in the order of $\epsilon_r = 2.8$. The cited losses include both dielec-
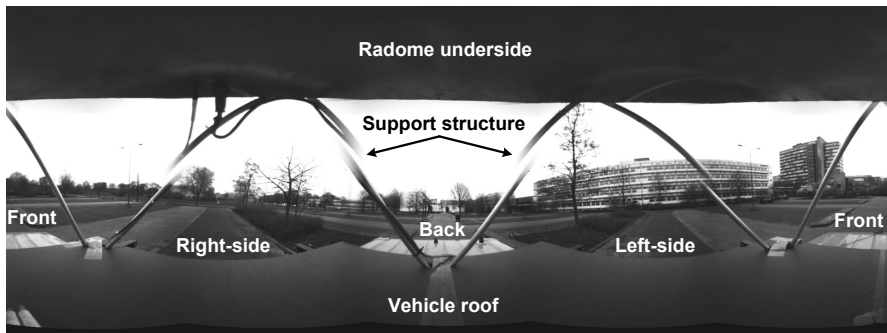
Fig. 4.2: Omnidirectional video sample obtained from the video camera that is mounted directly underneath the antenna array.

tric and reflectional losses. Because the radome may also introduce additional phase distortions, the effects on the angular estimation accuracy were also characterised at 2.25GHz in a lab environment. The influences of the radome were too small to be measured. Therefore, it was concluded that the radome does not cause significant aberrations.

To compare the measurement data with the actual environment, omnidirectional video data were captured from the receiver perspective using an omnidirectional video camera mounted directly underneath the antenna array. An example of such an image is shown in Fig. 4.2. The purchased camera, [79], consists of six closely packed image sensors, each with a resolution of 1024x768 pixels, combined with 2.5 mm lenses that are placed within 20 mm of each other. A fiber-optic digital connection is used to transfer the image data to the data-collection system, where the data are combined to create panoramic images of 1024x512 pixels based on accurate calibration using the physical location, the orientation of the sensors and a distortion model of the lens. The image axes x and y map to the azimuth (ϕ) and elevation (θ) angles, respectively, which allows the superimposition of estimated AOA information onto the video data. The camera is able to collect video data from more than 75% of the sphere surrounding the camera, but due to the obstruction of the vehicle below and the radome construction above, the video data in elevation are effectively limited to a range of $-35° < \theta < 35°$. The supporting structure of the antenna array, that is partly visible in the image data shown in Fig. 4.2, consists of aluminum tubes and is kept as small as possible to reduce further visual obstruction. The "ghosting" and misalignment of the aluminum tubes that are visible in the centre of the image are caused by the merging of the video data of the individual cameras and only occurs when objects are very close (< 6 m) to the camera.

In order to monitor the position and the movement of the measurement vehicle during the measurements, an advanced vehicle navigation system is used. The system consists of a navigation computer and a set of sensors [80]. The sensors include a temperature meter, a triad of calibrated magnetometers mounted outside the vehicle that serve as a digital compass, a triad of accelerometers, a barometric altimeter, a
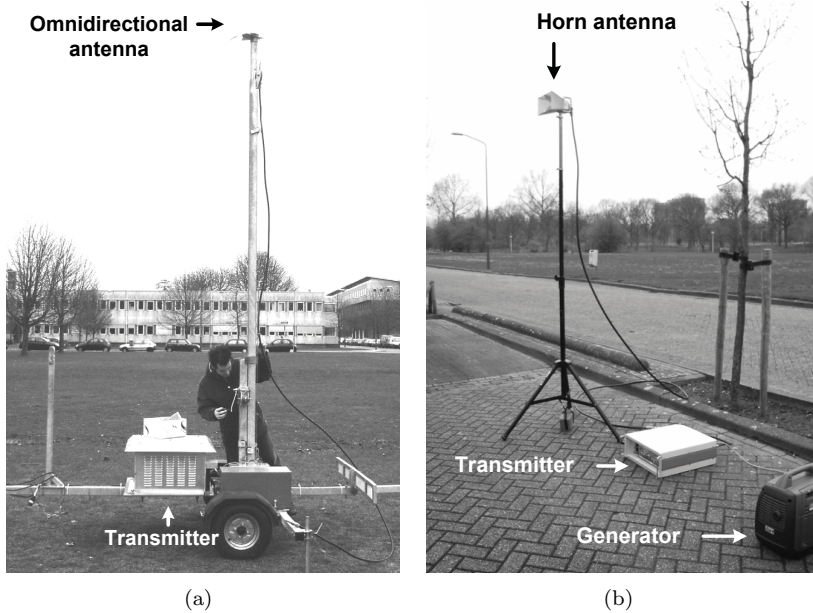
Fig. 4.3: Photograph of the transmitter setup using (a) the directional antenna and (b) the omnidirectional antenna.

gyroscope, an odometer sensor and a GPS receiver with its antenna mounted on the roof of the vehicle. By using the output of the sensors, the navigation computer determines the azimuth orientation, the pitch, roll, speed and positions of the vehicle at 10 Hz rate. Beside the GPS receiver output, the other sensor signals are also used as input to a Kalman filter to reduce the GPS position error. This is especially helpful when GPS reception is limited, e.g., around large buildings in dense urban areas.

The equipment used at the transmitter location is shown in Fig. 4.3 (a) and (b). Two types of transmit antennas were used in the experiments. In the rural experiments, a 2-dBi omnidirectional antenna, shown in Fig. 4.3 (a), was used. In the urban environment, a directional waveguide horn antenna was used, shown in Fig. 4.3 (b). This antenna has an 8 dBi gain in the azimuthal (H) plane, an azimuthal half-power-beamwidth of 55° and a bandwidth ranging from 1 to 18 GHz. Prior to each measurement campaign, a back-to-back measurement was performed to calibrate the system in terms of absolute received power.

4.3   Controlled rural environment

In order to verify the correct operation of the entire measurement system installed in the measurements vehicle, this section presents the results of experiments that

were performed in an open rural area in Boxtel, the Netherlands. A picture of the surroundings and the equipment is shown in Fig. 4.4. The area consists of a large farmer's field with several scattered trees, which are at a large distance from the receiver. Due to the open character of the environment effects of trees can be neglected.

Fig. 4.4: Photograph of the measurement equipment in the open rural area in Boxtel, the Netherlands.

Fig. 4.5 shows the layout of the measurement location. In the experiments the transmit antenna consisted of the vertically polarised 2-dBi omnidirectional antenna mounted on top of a mast, as shown in Fig. 4.3 (a), at a height of 7 m above ground level. The height of the receive antenna array, measured from the centre, is 3.5 m above ground level and the reference of the azimuth angle is the back of the measurement vehicle with the positive angles counter-clockwise. All measurements were performed with a nearly constant velocity and with speeds below 20 km/h.

4.3.1 Straight trajectory

In this experiment the receiver was moved towards the transmitter starting at a distance of 80 m, which corresponds to snapshot set $k = 0$. The receiver passed the transmitter at approximately snapshot 490 ($k = 490$) then continued to a maximum distance of 80 m from it, corresponding to $k = 1000$. A total of 1000 snapshot sets of $K = 10$ snapshots each are used for the AOA estimation along a trajectory of 160 m. This effectively means that a single angle-delay estimate of the channel is available every 0.16 m, which corresponds to 1.23 wavelengths.

Fig. 4.6 shows the power-delay profile obtained from the CIRs measured at all antennas, averaged over $K = 10$ snapshots (time-averaging) and averaged over all 31 antennas (spatial-averaging). The grey levels indicate the average received power levels in dBm in each of the delay bins. The theoretical delay along the trajectory is
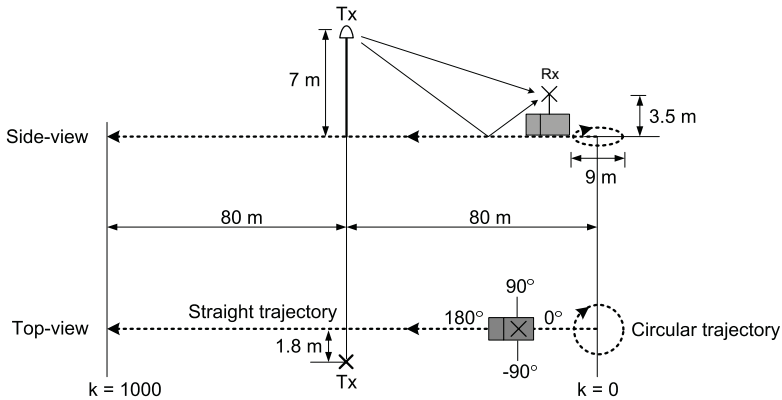
Fig. 4.5: Layout of the measurement location in Boxtel, the Netherlands. The dotted lines represent the measurement trajectories and k corresponds to the snapshot-set index.

also plotted for the LOS and ground reflected wave as a white-solid and white-dotted curve, respectively. Both curves correspond well to the measurements, but due to the limited delay resolution the ground and LOS wave cannot be separated here.
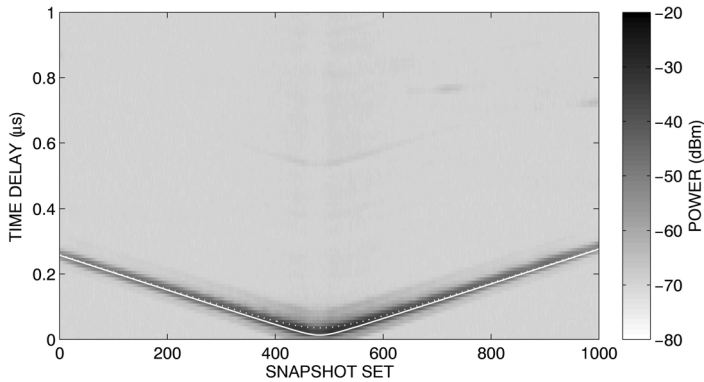
Fig. 4.6: Measured power-delay profiles along the straight trajectory. The theoretical delay along the trajectory for the LOS and ground reflected wave is represented by a white-solid and white-dotted curve, respectively

Before the collected CIR data are fed to the Unitary ESPRIT algorithm they have to be preprocessed by applying thresholds to limit the large number of data samples to be analysed. This is done by eliminating the noise in the CIRs that are obtained on each antenna [81]. In Section 2.2.2 on page 14 an I/Q imbalance compensation method was presented that causes a slight colouring of the noise statistics. Because the effects are very small, the background thermal noise is still assumed to be Gaussian.

The thermal noise standard deviation can then be estimated from samples that are certainly attributed to noise at large delays, where multipath arrivals are unlikely, as $\sigma_N = \sigma_m/\sqrt{\ln 4}$, where σ_m is the median of the amplitude distribution. The threshold level is then determined as $\zeta = \eta \cdot \sigma_N$, where $\eta = 1.8$. Furthermore, large noise samples can be removed by using the fact that they are very likely to be present in only one bin, in contrast to the true multipath components. Thus, if an isolated sample, and neither of its neighbours exceeds the threshold value ζ, it is considered to be attributed to noise, and discarded. Unless stated differently, in all the measurement results presented in this thesis, unreliable estimates are filtered out by using a value for the reliability threshold of $t_{rel} = 1$, as described in Section 3.3.4 on page 42.

Fig. 4.7 shows the estimated multipath components (MPCs) in the delay, elevation and azimuth domain. Theoretical values for the LOS and ground reflected wave are also plotted as a black-solid and black-dotted curve, respectively. Although the estimates in the three domains are interrelated, it is difficult to present them in a single multidimensional figure. The three domains are shown here independently and, as a result, the connection between the different domains is not explicitly visible. Still, the evolution of LOS component can clearly be observed in all domains.

The results show that in the azimuth domain the estimated angles along the trajectory compare well with the theoretical values. The estimated elevation angles are close to the theoretical values, but fluctuate around them. The cause of this effect can be explained by interference of the ground reflection. Although the LOS component is clearly detected, the ground reflection is not directly observed in the estimates. It was found that this is caused by the fact that the ground reflected wave is not always visible to all antennas in the array, due to their position in the array, shadowing by the support structure including the absorber underneath the array and, most dominantly, the obstruction of the measurement vehicle. This is supported by the results in Fig. 4.8, where the received power level along the trajectory of antenna 1, located in the upper part of the array, and antenna 2, located in the lower part of the array, are shown. Additionally the theoretical interference pattern caused by a LOS and reflected wave on medium-dry ground are shown [82]. The comparison of the theoretical and measured interference patterns shows that the ground reflected wave is only visible to antenna 1 along the entire trajectory. For antenna 2, which is positioned more to the back-side of the vehicle, the ground reflected wave is blocked during the first part of the trajectory, due to the obstruction by the front-side vehicle. It is very likely that the partial blocking of the ground reflected wave for the lower part of the antenna array causes phase errors in the received signal, which in turn cause fluctuations in the estimated elevation angles. To confirm this, additional simulations were performed in which the two-path model was used to simulate the effect of the ground reflected wave on the estimations. In these simulations the ground reflected wave was made "invisible" for the antenna elements in the lower part of the antenna array, which is an assumption. The effect on the estimation of the elevation angles for the LOS is shown in Fig. 4.9. The results show that the ground reflected wave can indeed cause a distortion of the estimated elevation angles of the LOS wave.
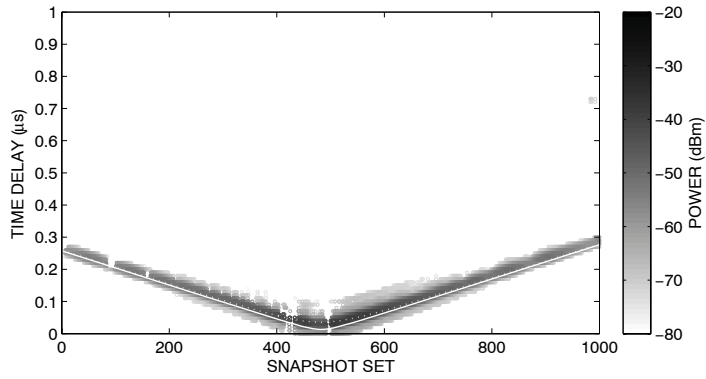
(a)
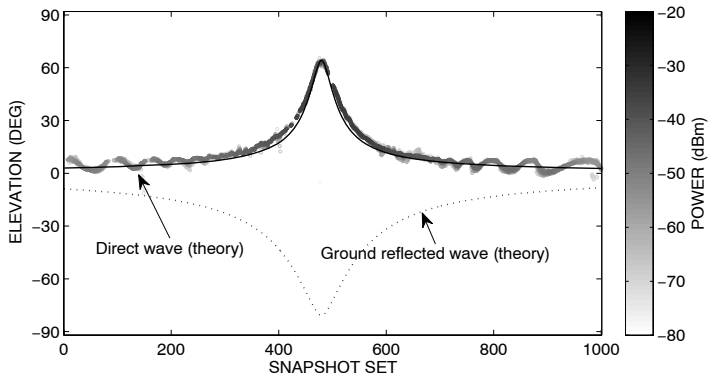
(b)
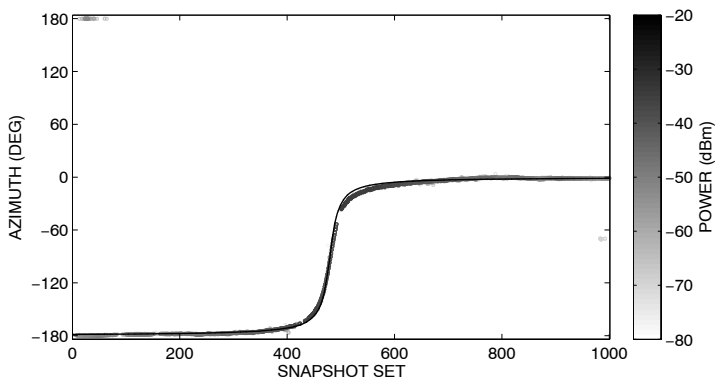
(c)

Fig. 4.7: Estimated MPC in the (a) delay, (b) elevational and (c) azimuthal domain along the straight measurement trajectory. The theoretical delay, elevation and azimuth angles for the LOS (solid black curve) and the ground reflected wave (dotted black curve) are also shown.
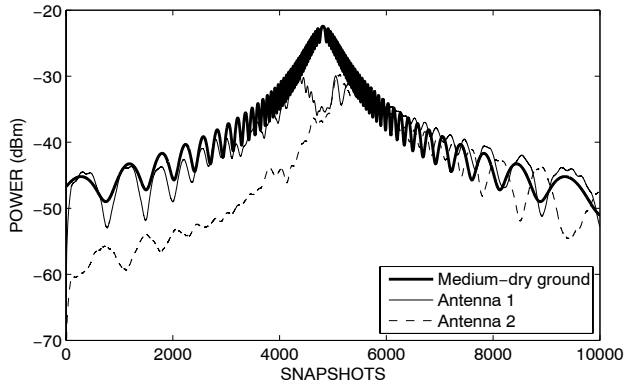
Fig. 4.8: Measured power level along the trajectory of antenna 1, located in the upper part, and antenna 2, located in the lower part of the array. The thick solid line represents the theoretical interference pattern caused by a LOS and reflected wave on medium-dry ground.
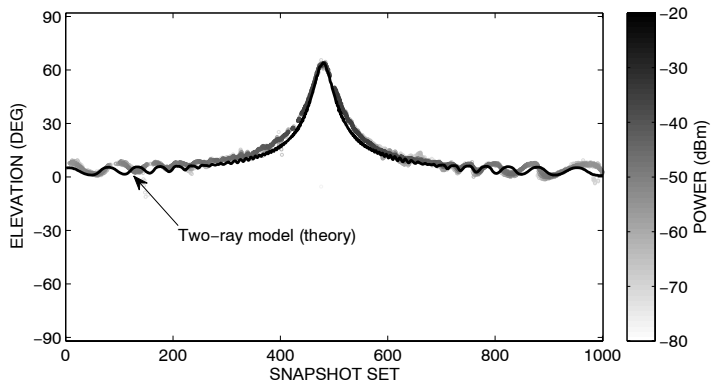
Fig. 4.9: Estimated MPC in the elevational domain along the straight measurement trajectory. The black curve represents the theoretical elevation angle estimated based on the two-path propagation model.

It was found from additional measurements that, when the antenna array is tilted towards the transmitter, thereby extending its negative elevation range, the ground reflection becomes visible. As a result, the range in negative elevation angles is effectively limited down to approximately $-7°$ for waves arriving from the front or the back of the vehicle and to $-15°$ for waves arriving from either the left or right side. Extending the range in the negative elevation area, such that ground reflected waves can be observed in all cases, would require drastic changes, such as a different measurement vehicle and a redesign of the support structure of the antenna array.

4.3.2 Circular trajectory

In this experiment the receiver is moved along a circular trajectory with a radius of 4.5 m at a distance of 80 m from the transmitter, as shown in Fig. 4.5 on page 62. The trajectory is slightly more than a single circumference and a total of 300 snapshot sets of $K = 10$ snapshots each are used. This effectively means that a single angle-delay estimate of the channel is available every 0.1 m, which corresponds to 0.77 wavelengths.

Fig. 4.10 shows the estimated MPCs in the delay, elevation and azimuth domain. Theoretical values for the delay, elevation and azimuth are also plotted in the figure as black curves. The additional contribution, in the delay domain close to 0.9 μs, in the elevation domain close to $0°$ and in the azimuth domain parallel to the LOS and shifted by approximately $75°$, is caused by a reflection from an existing plane metal object, approximately 130 m away from the receiver. In the results for elevation, some fluctuations are visible, which are most likely caused by the partial blocking of the ground reflected wave as well as due to the tilting of the measurement vehicle caused by uneven terrain. The estimates are slightly above and below the theoretical values, each for approximately half of the measurement duration. In the azimuth domain there is a clear transition of the estimated azimuth angles over the entire range and no effects of shadowing by the support structure are visible, as previously discussed in Section 3.3.5 on page 44. The slight discrepancy between the estimated results and the theory within snapshot set 75 and 175 is caused by a temporary reduction in the speed of the measurement vehicle.

(a)

(b)

(c)

Fig. 4.10: Estimated MPC in the (a) delay, (b) elevational and (c) azimuthal domain along the circular measurement trajectory. The black curves represent the theoretical delay, elevation and azimuth angle respectively.

4.4   Urban environment

In addition to the rural scenario, measurements were also carried out in a real-world urban environment on the TU/e campus. The measurement area, depicted in Fig. 4.11, is characterised by several high buildings and scattered vegetation. Two scenarios were considered in which the transmitter was positioned either above, or below the average rooftop level. To reduce disturbing factors, the measurements were carried out at a time when traffic density and the number of parked cars was low. The transmitting antenna (Tx), shown in Fig. 4.3 (b) consisted of an 8-dBi waveguide horn antenna with an azimuthal half-power-beam-width of 55°. During the measurements omnidirectional video data were captured from the receiver perspective using the omnidirectional video camera described in Section 4.2.
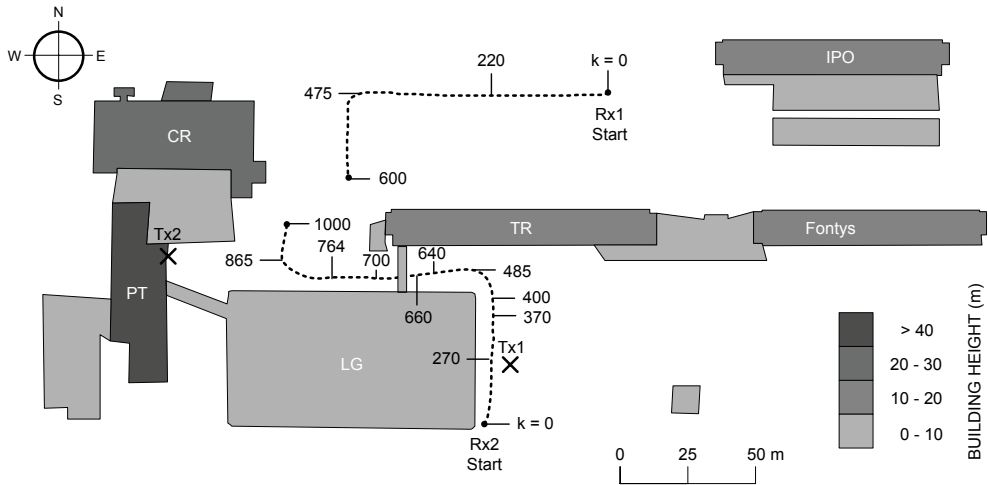
Fig. 4.11: Layout of the measurement location. The dotted line represents the GPS coordinates of the measurement trajectory. Along the trajectory values for k are plotted that correspond to the snapshot set numbers. Grey levels indicate the building heights in metres.

4.4.1   Transmitter below rooftop

The transmitting antenna, marked in Fig. 4.11 as Tx1, was positioned outside, at a height of 3.5 m above ground level and pointed northward. The receiving antenna, marked in Fig. 4.11 as Rx1, was positioned at the other side of building TR, thereby obstructing the LOS path, and was moved at a nearly constant speed of about 7.5 km/h over a trajectory of approximately 125 m, marked with a dotted line in Fig. 4.11. A total of 1000 snapshot sets of $K = 10$ snapshots each are used for the AOA estimation. This effectively means that a single angle-delay estimate of the channel is available every 0.125 m corresponding to 0.96 wavelengths.
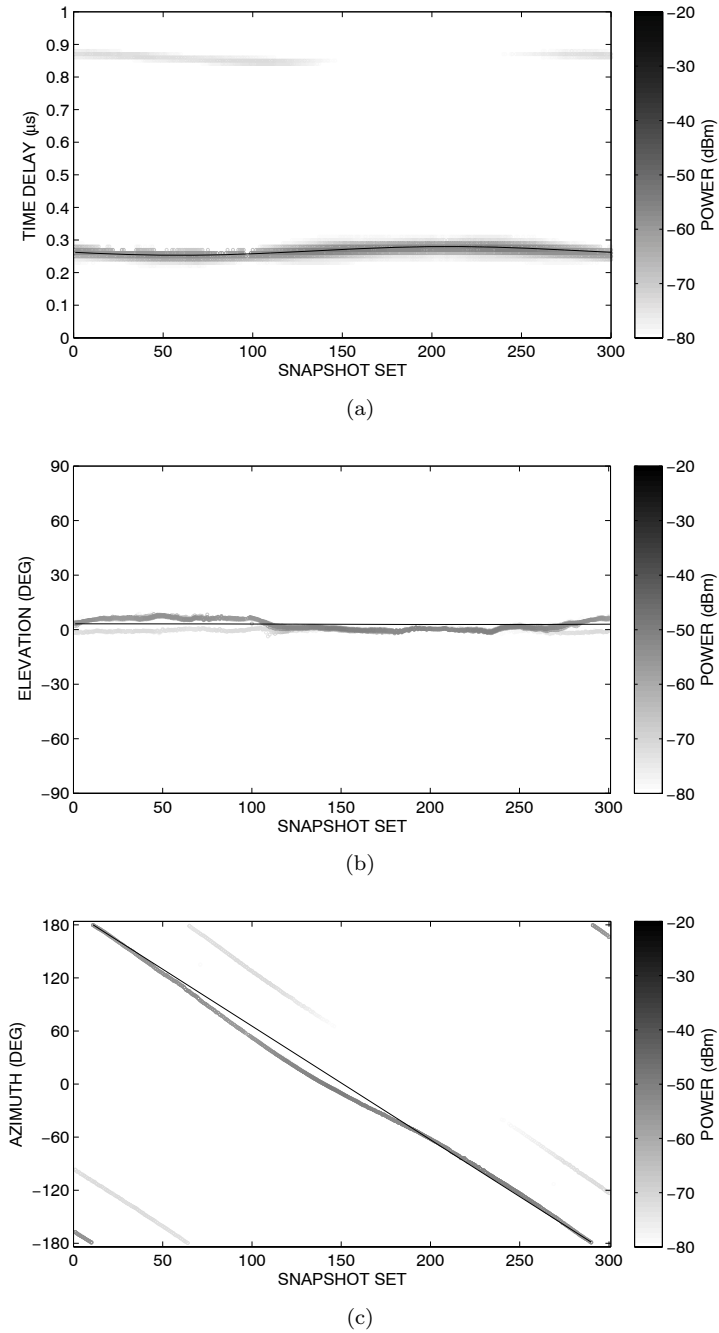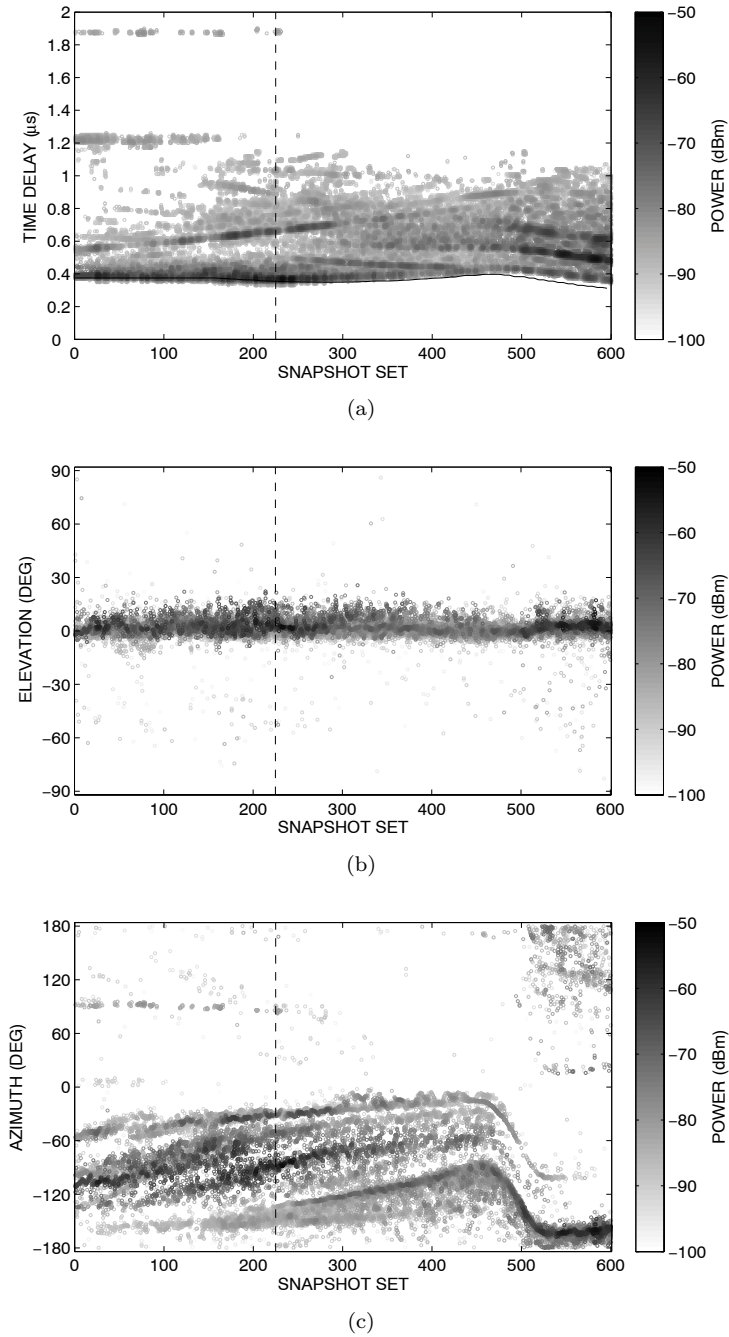
Fig. 4.12: Estimated MPCs in the (a) delay, (b) elevational and (c) azimuthal domain along measurement trajectory Rx1 with the transmitter (Tx1) below rooftop. The black curve in (a) represent the theoretical delay of the LOS and the black dotted vertical line corresponds to snapshot set $k = 225$ shown in Fig. 4.13.

Fig. 4.12 shows the estimated MPCs in the delay and angular domain along the entire trajectory. The grey levels indicate the absolute received power levels of the individual MPCs in dBm. In the first part of the trajectory, up to $k \simeq 275$, most of the contributing power comes from the propagation through-building TR. Because over rooftop propagation is minimal, the estimated elevation angles remain small. In azimuth, however, a large dispersion is observed that can roughly be divided into two dominant clusters. In Fig. 4.13, a single video frame corresponding to snapshot set $k = 225$ is shown combined with the angular estimations. Here, the two clusters are visible close to $\phi \simeq -60°$ and $\phi \simeq -90°$, and are caused by propagation through different parts of building TR. Additional MPCs arrive from close to $\phi \approx -35°$ at $\tau \simeq 0.55\mu s$. This energy can be identified as a reflection from the side of building Fontys. It is clearly visible along the rest of the trajectory. At a position close to $k \simeq 200$ waves begin to arrive due to reflections from building CR. These contributions are most likely caused by multiple reflections between building TR and building LG and eventually become dominant. The contributions also show increased dispersion in the delay domain.

The results above demonstrate that the measurement system can aid in the accurate characterisation of propagation effects along a trajectory in a complex environment. Furthermore, the omnidirectional video data allow accurate identification of the sources of scattering and reflection. The results show that significant dispersion can occur in both the delay and azimuth domain in scenarios where no LOS is available and the transmitter is positioned below the average rooftop level. This is mainly caused by through-building propagation and multiple reflections from irregular building surfaces.
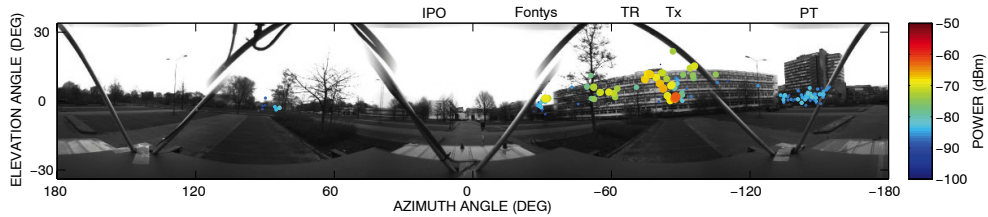
Fig. 4.13: AOAs of MPCs superimposed on omnidirectional video data at snapshot set $k = 225$. The received power is also represented by the size of the markers, where the largest marker corresponds to the highest received power.

4.4.2 Transmitter above rooftop

In this scenario, the transmitting antenna, marked in Fig. 4.11 as Tx2, was positioned above the average rooftop level, inside, against a large window at 40 m above ground level and pointed eastwards at a tilting angle of 20° downward. The receiving antenna, marked in Fig. 4.11 as Rx2, was moved at a nearly constant speed of about 9 km/h over a trajectory of approximately 150 m, marked with a dotted line in Fig. 4.11.

A total of 1000 snapshot sets of $K = 10$ snapshots each are used. This effectively means that a single angle-delay estimate of the channel is available every 0.15 m, which corresponds to 1.1 wavelengths.

Fig. 4.14 shows the estimated MPCs in the delay and angular domain along the trajectory [1]. The first part of the measurement trajectory ($0 < k < 400$) was chosen such that there was an obstructed path from the Tx to the Rx location behind building LG and over-rooftop diffraction could occur. The results show an attenuation of the dominant signal component and an increase in the elevation angle up to $\theta \simeq 30°$ as expected. Other lower powered components with considerable angular spread are also observed and it is believed that they were caused by scattering from trees and other irregular objects. After passing building LG at $k \simeq 400$ the stronger line-of-sight component becomes visible. The measurement vehicle takes a 90°-turn and moves further along the trajectory, which causes the LOS component to change 90° in azimuth, to increase in elevation and to get temporarily obstructed by the elevated walkway ($640 < k < 660$) as expected. Within $485 < k < 865$ a strong component at $\phi \simeq 0°$ originating from the lower part of building TR and a number of scattering components caused by irregularities in the building surface are visible. Some scattering also occurs from building LG together with a number of distinct reflections around $\phi \simeq -80°$, which can be directly related to the corner-shaped parts of building LG. Finally, the effects of passing under the elevated walkway are visible as a reflection starting at $\theta \simeq 40°$ and rapidly decreasing to $\theta \simeq 20°$. In Fig. 4.15, video frames of different locations along the measurement trajectory corresponding to snapshot sets $k = 270, 370, 700$ and 764 are shown combined with the angular estimation results. By combining the estimation results with the captured video data the estimation results can be related directly to the actual environment. When all the frames of the entire trajectory are combined an illustrative video is created in which the MPCs can be observed and tracked. This provides much insight into the different propagation phenomena and their behaviour while moving through the environment.

Compared to the scenario in Section 4.4.1, the above rooftop scenario clearly shows a *less* dispersive behavior of the MPCs in the delay and azimuth domain. The MPCs are, however, less *concentrated* in the azimuth domain. In the elevation domain the MPCs are more clearly visible and more dispersion is observed.

---

[1]Note that in these results, unreliable estimates are filtered out by using a value for the reliability threshold of $t_{rel} = 3$. Although a value of $t_{rel} = 1$ is used throughout this thesis, changing this value between $0.5 < t_{rel} < 3$ does not result in considerable differences.

(a)

(b)

(c)
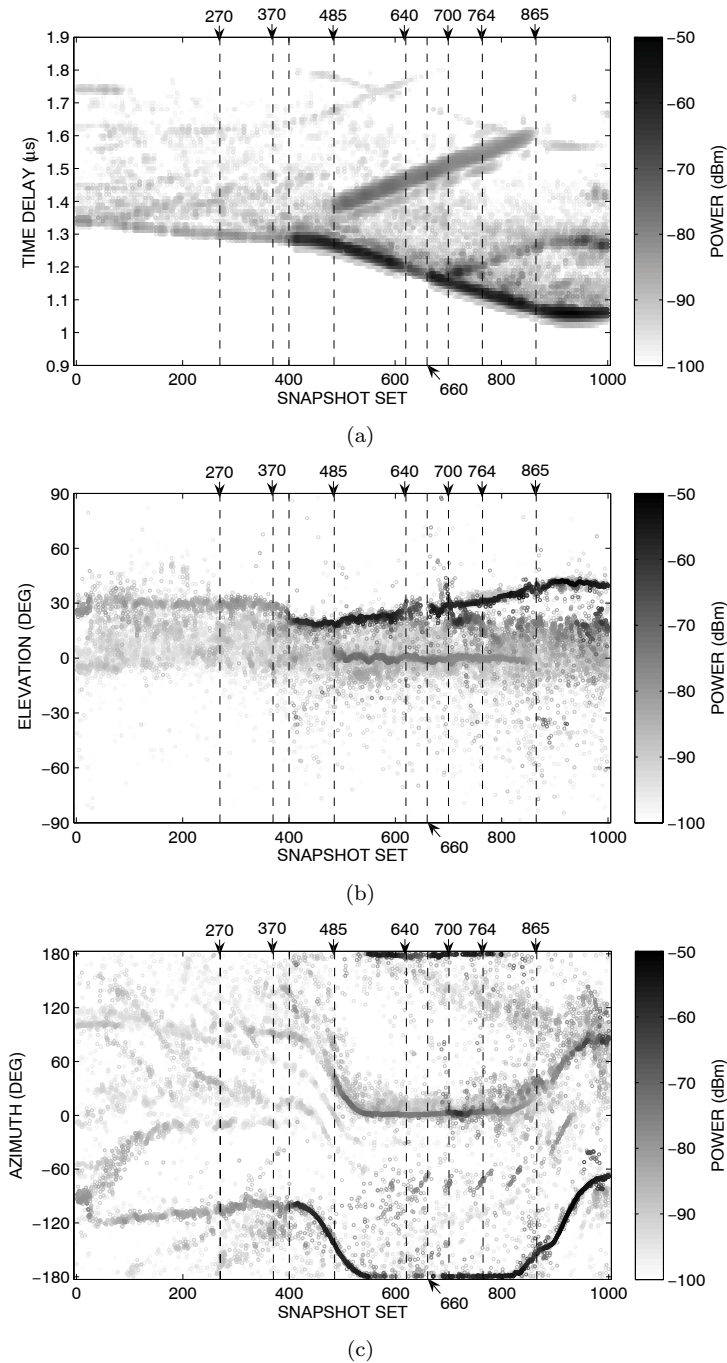
Fig. 4.14: Estimated MPCs in the (a) delay, (b) elevational and (c) azimuthal domain along measurement trajectory Rx2 with the transmitter (Tx2) above rooftop.

(a)

(b)

(c)

(d)
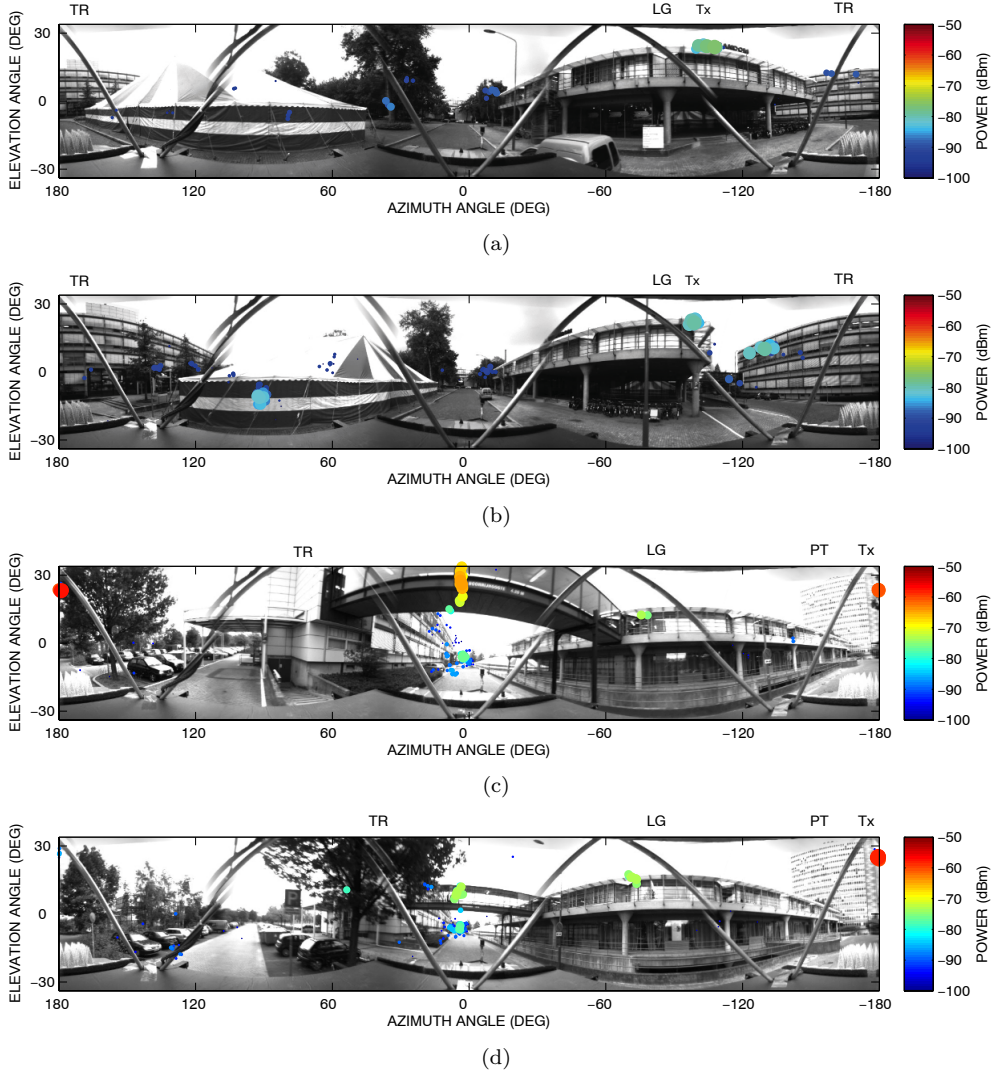
Fig. 4.15: MPC angles of arrival superimposed on omnidirectional video data at snapshot set (a) $k = 270$, (b) $k = 370$, (c) $k = 700$ and (d) $k = 764$. The received power is also represented by the size of the markers, where the largest marker corresponds to the highest received power.

4.5   Conclusions

In this chapter, results of delay and angular characteristics of dominant MPCs are presented that were obtained in several outdoor experiments using the AOA measurement system that was presented in Chapter 2 and 3. The system was installed in a measurement vehicle together with necessary additional equipment, such as an omnidirectional video camera.

The results obtained in a rural environment show that the system can accurately determine the elevation and azimuth AOAs in physically-nonstationary mobile radio channels. It was found that, due to the antenna support structure and measurement vehicle, the measurement range in the negative elevation angles is effectively limited to $\theta \simeq -7°$ in the worst case. As a result, the AOAs of ground reflected waves are generally not detected and phase errors can cause fluctuations in the estimated elevation angles of the LOS. In the azimuthal domain, uniform AOA estimation performance was observed over the entire range ($-180° < \phi < 180°$).

Furthermore, results in an urban environment show that the evolution of the MPCs along a trajectory can be characterised. Omnidirectional video data that were captured during the measurements are used in combination with the measurement results to accurately identify and relate the received radio waves directly to the actual environment while moving through it.

The results also show that significant dispersion can occur in both the delay and azimuth domains in scenarios where the transmitter is positioned below the average rooftop level. The above rooftop scenario clearly shows *less* dispersion in the delay and azimuth domains, but more dispersion is apparent in the elevation domain.

The high-resolution capabilities of the measurement system and the ability to measure physically-nonstationary channels can provide more information about the nature of the propagation mechanisms, such as through-building propagation and irregular surfaces. They can also help to improve deterministic propagation predictions by calibration of reflection and scattering components and by identifying the most significant propagation mechanisms leading to possible decreases in terms of computational complexity. Additionally, the measurement system can also be useful as a diagnostic tool as will be shown in the next chapter.

In summary, the main contributions and innovations of the work presented in this chapter are:

- The result of measurements along a trajectory are presented that show the capabilities and performance of the measurement system in a real-world scenario. Elevation angles are estimated accurately, but waves reflected by the ground are difficult to detect and phase distortions due to ground reflected waves cause a reduction of the estimation performance in elevation.

- The composition of multipath components along a trajectory can be accurately characterised and tracked. Omnidirectional video data that were captured during the measurements are used in combination with the measurement results

to accurately identify and relate the received radio waves directly to the actual environment while moving through it.

- The results from outdoor experiments in an urban environment show that over rooftop diffractions can be identified, as well as reflections from irregular building structures and diffuse scattering effects in the delay and angular domain. The results were previously published by the author in [37].

5

Use of the high-resolution measurement system as a diagnostic tool

5.1 Introduction

The complexity of radio propagation in urban environments makes it increasingly difficult to fully understand and accurately predict propagation behavior in order to achieve an optimal network configuration. As better radio propagation measurement systems become available, the limitations of the propagation prediction tools that network operators use become more apparent, making it also clear that networks designed with such tools have a significant probability of being sub-optimal. It is known to operators that in specific areas in operational radio networks propagation phenomena can cause unexpectedly poor performance, which includes limited coverage, dropped calls, decreased data-rates and unexpected handovers. In order to obtain better insight and possibly solve these issues, more knowledge about the actual propagation effects is required. Although the results of "drive-tests" are sometimes used in an attempt to obtain more insight into the propagation effects, they merely give an observation of the effects. The quality and resolution of these results are limited and only signal strengths are measured.

To date, only very few methods exist that can accurately identify the propagation effects in mobile scenarios. The measurement approach presented in the previous chapters is capable making very accurate AOA and delay measurements, enabling the

accurate characterisation of the dominant propagation effects with high resolution and under mobile conditions. This approach can be very helpful in obtaining more insight into propagation phenomena and the use of video data allows to relate the propagation effects directly to the environment. In the framework of a collaboration between TU/e, TNO ICT and KPN the measurement system was used as a diagnostic tool in a dense urban environment. In this specific environment poor performance was previously observed from the results obtained from "drive tests". The poor performance is caused by unexpected reduction of the power of the desired base-station (BS) signal and interference from a neighbouring BS. The propagation phenomena that cause these effects are not predicted by the type of propagation models that are currently used by most mobile system operators, including KPN. This means that it is impossible to improve the network performance in these areas based on the current propagation models. In order to identify the propagation phenomena that cause the poor performance, the high-resolution measurement system was configured such that it generates similar propagation behavior as the actual network and measurements were performed in the area.

This chapter describes the diagnostic survey and the results of the analysis. The results obtained in the scenarios presented here are especially important for mobile system operators. It is shown that the measurement approach can be used to generate a real network scenario and is capable of accurately identifying the dominant propagation effects with high-resolution while moving through a real-world urban scenario. Furthermore, the results directly show the limitations of the propagation prediction model currently used by KPN and the importance of accurate propagation knowledge and modelling.

Firstly, Section 5.2 describes the scenario, the environment and the problems in terms of poor performance and interference. Secondly, Section 5.3 discusses the initial propagation prediction results, used for the network design. In Section 5.4, the measurement setup and procedure, as well as the results of the measurements are then presented. Here, the effects of shadowing and, moreover, reflections by irregular surfaces are shown to be significant. Furthermore, the limitations of the currently used propagation prediction model, and the importance of improved propagation modelling are illustrated. Finally, conclusions are drawn in Section 5.5.

5.2   Scenario description

The area that was selected for measurements is shown in Fig. 5.1. It is located close to the Amsterdam Arena Stadium near the city of Amsterdam. The area is characterised by a main wide street (20-25 m) and a number of railway crossovers. In the area several three- to seven-storey high buildings can be found consisting of concrete and steel and with irregular faces caused by balconies and windows. Trees are found along the main street and also scattered across the entire area. The traffic density during the measurements was low (5-10 cars per minute). A single frequency UMTS network is operational in the area, with two base-stations (BSs) located at
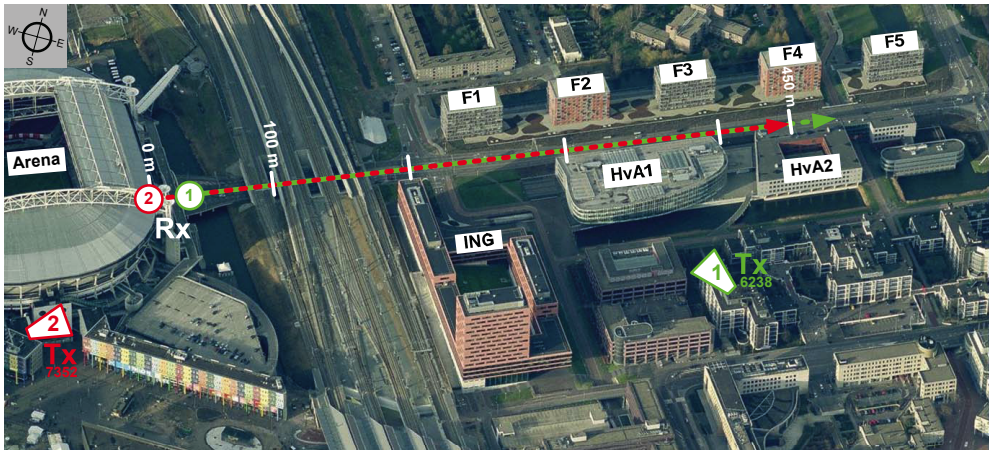
Fig. 5.1: Layout of the measurement site. The red and green dotted lines represent the measurement trajectories with the transmitter active at BS 7352 and BS 6238, respectively. Copyright: Microsoft Virtual Earth, `http://www.microsoft.com/virtualearth`.

positions marked by 7352 and 6238, shown in Fig. 5.1. The frequencies for the downlink and uplink channels are 2132.2 MHz and 1942.2 MHz respectively, for both BSs. At each BS directional antennas are used as sector antennas, which exhibit a horizontal half-power beamwidth of 88° and a gain of 16.7 dBi. The antennas are driven by a +43 dBm signal. A mobile UMTS user (receiver) that moves in the area close to the trajectory marked with the red and green dotted lines should be served by one of these BSs.

5.3   Stochastic empirical prediction results

The network is designed such that the area along the main wide street is served best by BS 6238. This is confirmed by the results in Fig. 5.2 (b), which shows the best server area for BS 6238 (orange) and BS 7352 (light grey). The simulation results are obtained from a stochastic empirical propagation model. The empirical model was developed by KPN for field strength predictions and is a modification of the widely used Okumura-Hata model [83]. In order to increase the accuracy of the Okumura-Hata model, KPN expanded the model by including more detailed information about the propagation environment. Therefore, the area is subdivided into a grid of square subdomains of dimension 20 x 20 m, each with its own environment classification, shown in Fig. 5.2 (a). The different classifications range from open area (white), water (blue), vegetation (green) to urban (brown), and each of the classifications is related to a certain amount of propagation loss. Because of confidentiality reasons, KPN can not provide exact details of the classifications. Signal powers are determined by using different propagation loss models, chosen according to the area classifications.
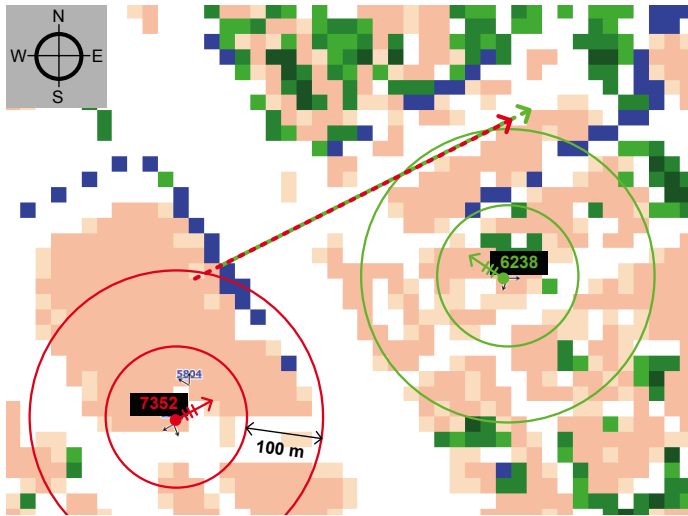
(a)
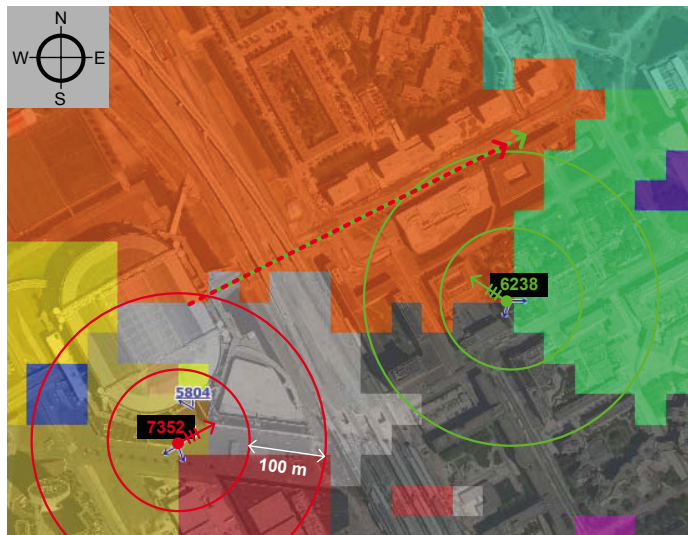
(b)

Fig. 5.2: Layout of measurement site with (a), the grid of environment classifications with open area (white), water (blue), vegetation (green) and urban (brown) and (b), the best served areas for BS 6238 (orange) and BS 7352 (light grey), determined using the stochastic empirical propagation model discussed in Section 5.3.

Although this takes local information into account in a broad sense, no information about reflections, backscattering, delay spread or angular spread is considered. As a result, propagation predictions for dense urban areas often contain errors.

5.4   Measurements

In an earlier study by KPN, measurements were performed in the area. The results for the received power along the trajectory, as well as the predicted values, are shown in Fig. 5.3 (a). For BS 6238 the received power is considerably below the predicted value, whereas for BS 7352 the power at some positions is above the predicted value. As a result, the received power of the undesired BS is above that of the desired BS at several positions, which causes undesired handovers and a reduction in performance. Measurements were performed using the high-resolution measurement system described in the foregoing chapters to obtain more insight into the propagation phenomena that are significant in this area, and to find possible causes for propagation prediction error.

5.4.1   Setup and procedure

Two independent measurements were performed in which the transmitter was placed at both BS locations. The transmitting antenna consisted of an 8-dBi waveguide horn antenna with an azimuthal half-power-beam-width of $55°$. A tripod is used to elevate the antenna such that it is in almost the same position and has the same orientation as the original BS antenna, as shown in Fig. 5.4 for BS 7352 as an example.

- In the *first* experiment the transmitting antenna was positioned outside, at a height of 29 m above ground level close to BS 6238 marked in green in Fig. 5.1. The direction of the main beam was pointed towards $-60°$, where $0°$ corresponds to the north and the positive angles are clockwise.

- In the *second* experiment the transmitting antenna was positioned outside, at a height of 27 m above ground level close to BS 7352 marked in red in Fig. 5.1. The direction of the main beam was pointed towards $70°$.

The receiving antenna, mounted on top of a vehicle at a height of 3.5 m, was moved at a nearly constant speed of about 27 km/h over a trajectory of approximately 450 m, indicated with a green and a red dotted line in Fig. 5.1 for the first and second experiment, respectively. A total of 9900 snapshot-sets of $K = 10$ snapshots are used for the AOA estimation, which means that a channel estimate is available every 4.5 cm, corresponding to 0.34 wavelengths.
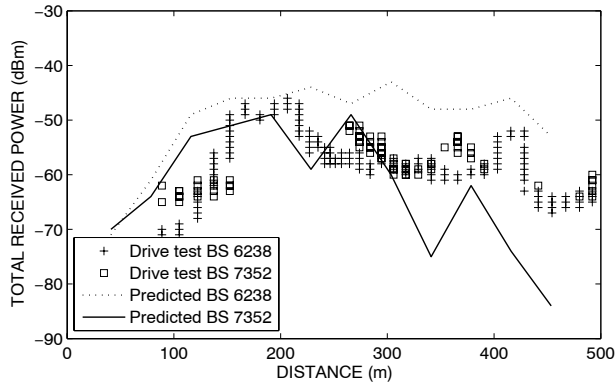
(a)
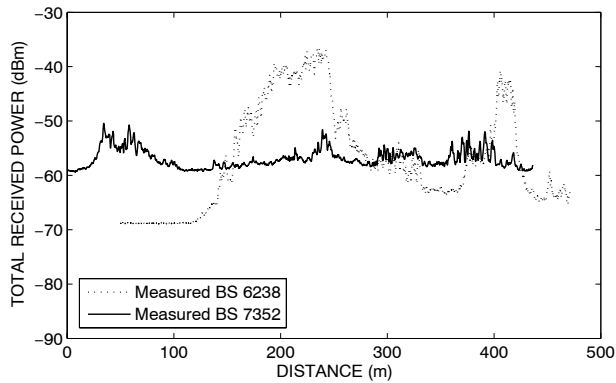
(b)

Fig. 5.3: Measured power of both BSs along the trajectory obtained from (a), a previous KPN drivetest and predictions using the stochastic empirical model discussed in Section 5.3 and (b), using the high-resolution measurement system.

Fig. 5.4: Transmitting antenna positioned outside, close to BS 7352 and pointed in the same direction.

5.4.2 Results

In Fig. 5.3 (b), the results of the total received power, in both experiments, along the trajectory are presented. The large scale fluctuations of the power received of BS 6238 are similar to the KPN drive test results in Fig. 5.3 (a), obtained from an earlier study. Furthermore, a more constant received power level of BS 7352 is observed, which exceeds the level of BS 6238 along several parts of the trajectory. The difference in absolute power levels between the KPN drive test and the high-resolution measurements in Fig. 5.3 (a) and (b) is mainly due to insufficient information about the measurement equipment (e.g. cable attenuation, antenna patterns) used in the KPN drive test.

The results in Fig. 5.5 show the estimated multipath components (MPCs) in the delay and angular domain along the trajectory obtained from the signals received by BS 6238. Up to $k \simeq 2000$, the received signal is very weak. Visual inspection of the environment shows that this is mainly caused by the obstruction of building ING. Apart from small reflections by building Arena and the railway infra-structure, through-building propagation is dominant in this area. Between $2000 < k < 5000$ the receiver moves into and out of the LOS region and the received power, as well as the delay spread and angular spread, increase. Particularly in the azimuth domain, a number of distinct components are visible that seem to change rapidly in the azimuth direction. From the omnidirectional video data it was found that these distinct components are caused by reflections from lampposts, traffic signs and plane metallic objects.

Fig. 5.5: Estimated MPCs along the measurement trajectory from the signals received from BS 6238 in the (a) delay, (b) elevational and (c) azimuthal domain.

A number of other more diffuse and less rapidly changing components are also visible. By using the omnidirectional camera data, these components can be related to reflections from irregular (building) surfaces and objects and through-building propagation. Fig. 5.6 shows the estimation results of snapshot $k = 3900$ superimposed on a video frame. Here, the LOS component is clearly visible as well as other components caused by reflections from buildings, traffic signs and other objects.

During the remaining part of the trajectory the receiver remains mainly in the NLOS region. Reflections from mainly the upper parts of buildings F1 to F4, shown in Fig. 5.1, are also visible in the elevation domain as consecutive collections of MPCs at larger elevation angles. These collections of MPCs are visible in the azimuth domain as bands that change from $\phi \simeq -180°$ to $0°$. These bands of MPCs consist of a stronger specular component as well as a more diffuse part. The scattering in the diffuse part is caused by the irregular structure of the buildings, consisting of irregularly distributed windows and steel balconies. The results in Fig. 5.7 and 5.8 show the estimates at $k = 6720$ and $k = 7890$, respectively. In the short interval between $8250 < k < 8750$, a LOS between HvA1 and HvA2 exists. The moment just before the LOS region is also shown in Fig. 5.9.

(a)

(b)
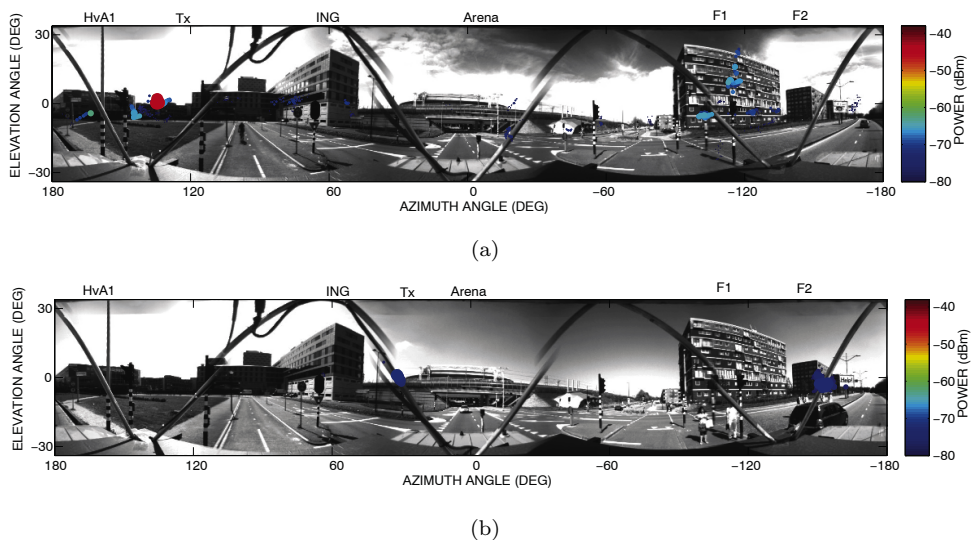
Fig. 5.6: MPC angles of arrival superimposed on omnidirectional video data for (a), Tx at BS 6238 and $k = 3900$ and (b), Tx at BS 7352 and $k = 4995$. The received power is represented by the colour as well as the size of the markers, where the largest marker corresponds to the highest received power.
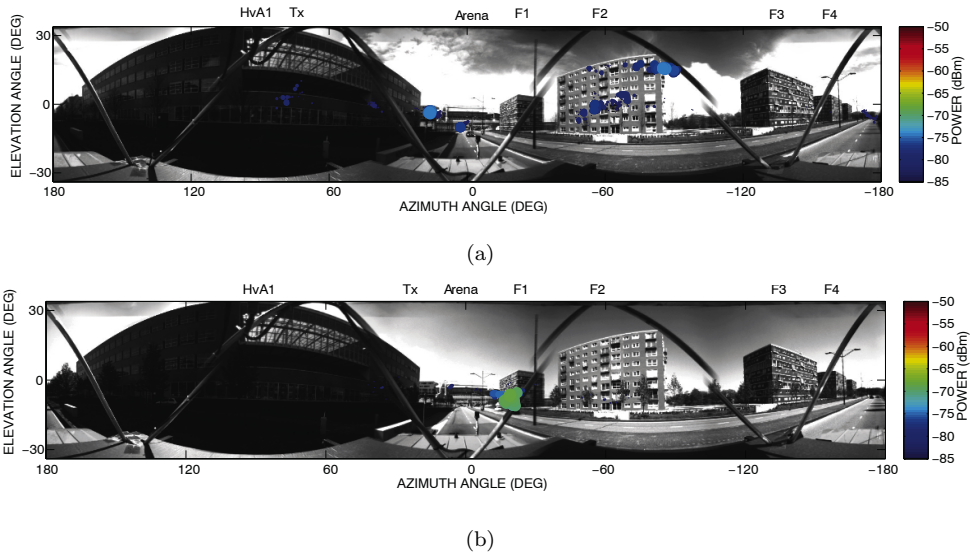
Fig. 5.7: MPC angles of arrival superimposed on omnidirectional video data for (a), Tx at BS 6238 and $k = 6720$ and (b), Tx at BS 7352 and $k = 7590$. The received power is represented by the colour as well as the size of the markers, where the largest marker corresponds to the highest received power.
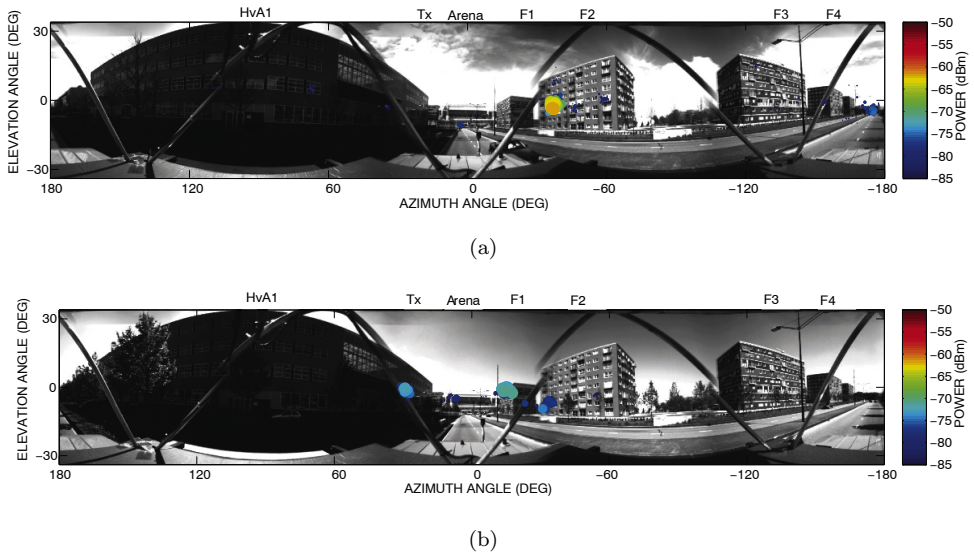
Fig. 5.8: MPC angles of arrival superimposed on omnidirectional video data for (a), Tx at BS 6238 and $k = 7020$ and (b), Tx at BS 7352 and $k = 7890$. The received power is represented by the colour as well as the size of the markers, where the largest marker corresponds to the highest received power.

The results in Fig. 5.10 show the estimated MPCs in the delay and angular domain along the trajectory obtained from the signals received by BS 7352. Up to $k = 3500$, most of the received power is received via reflections by the railway infrastructure and crossovers, as well as via propagation around and through building Arena. The vertical spikes in the elevation domain result from propagation through the vertical open parts of the railway crossovers. This is visualised in Fig. 5.11. From $3500 < k < 6000$, two more dominant contributions are visible. The strongest contribution varying from $\phi \simeq 30°$ to $0°$ is caused by propagation over the railway crossovers. The other lower and more diffuse contribution is caused by the front and side face of building F2, perpendicular to the trajectory. This is visualised in Fig. 5.6 (b), where the two components are clearly visible. Although no specular path exists from Tx to Rx via building F2, scattering caused by the irregularities still causes significant power to reach the receiver. In the second part of the trajectory significant contributions by reflections from building F1 and F2 are visible as well as second-order reflections most likely from the buildings HvA1 and HvA2 and the trees in front of them. This is also visualised in Figs. 5.7, 5.8 and 5.9.

(a)

(b)
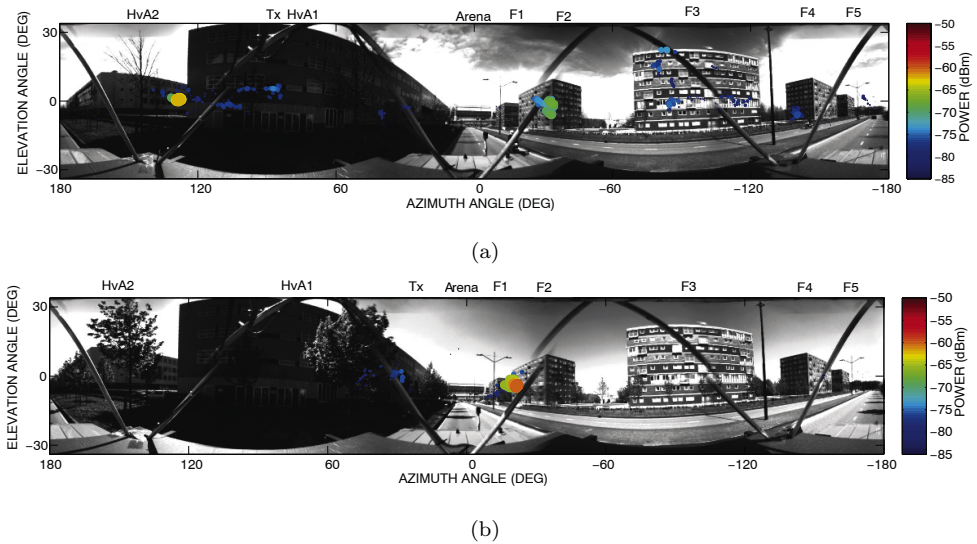
Fig. 5.9: MPC angles of arrival superimposed on omnidirectional video data for (a), Tx at BS 6238 and $k = 7725$ and (b), Tx at BS 7352 and $k = 8490$. The received power is represented by the colour as well as the size of the markers, where the largest marker corresponds to the highest received power.
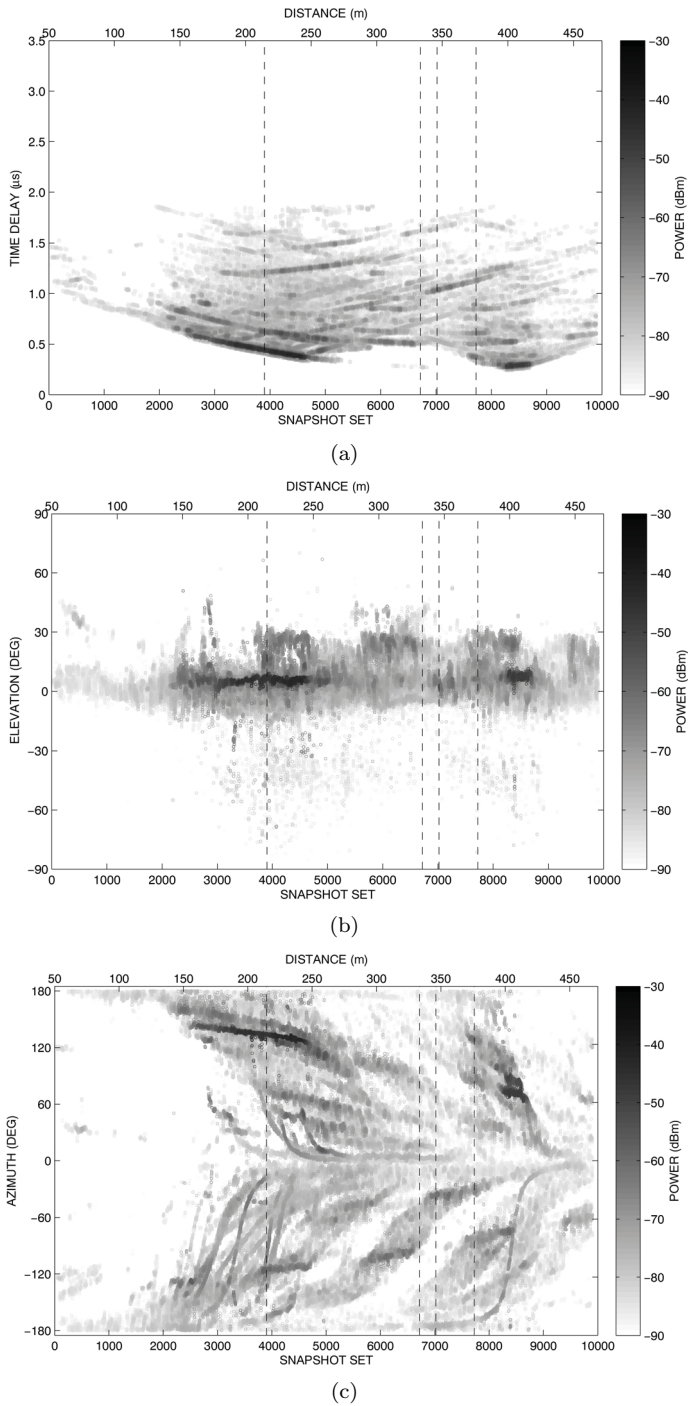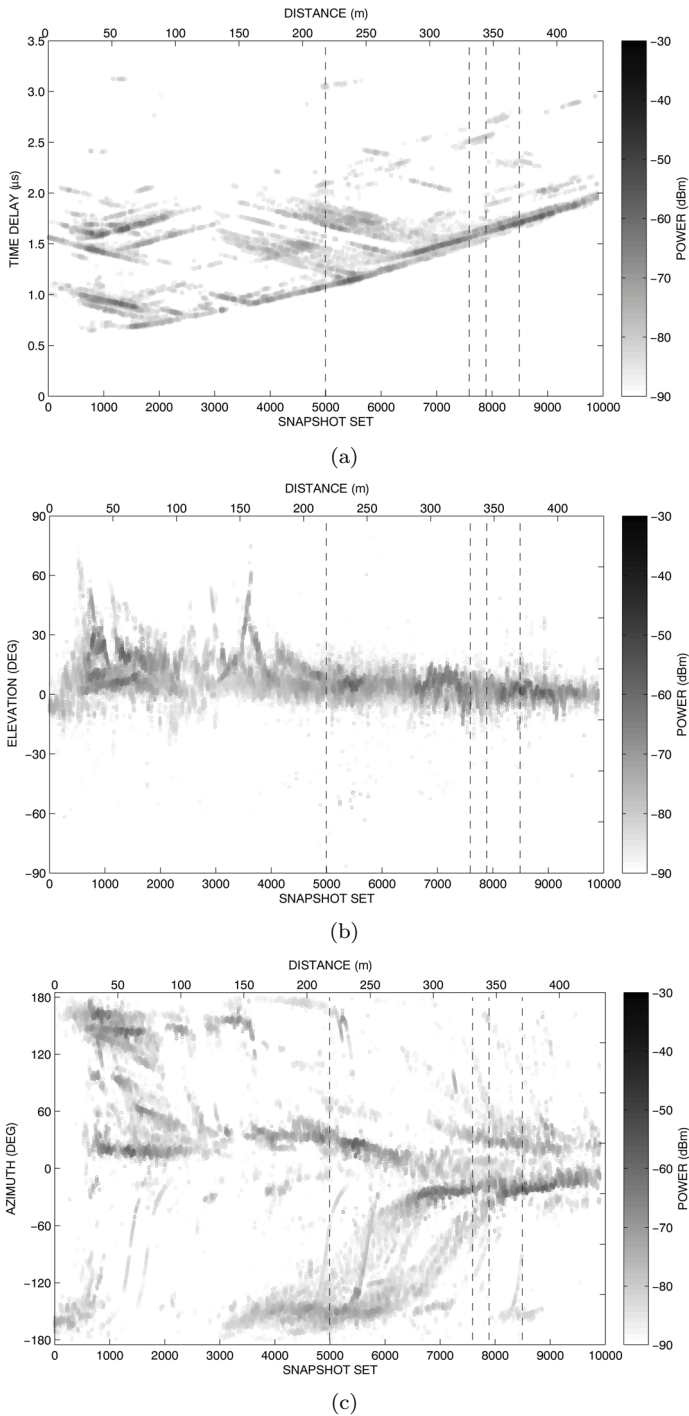
Fig. 5.10: Estimated MPCs along the measurement trajectory from the signals received from BS 7352 in the (a) delay, (b) elevational and (c) azimuthal domain.

Fig. 5.11: MPC angles of arrival superimposed on omnidirectional video data for Tx at BS 7352 and $k = 3100$. The received power is represented by the colour as well as the size of the markers, where the largest marker corresponds to the highest received power.

From the results discussed above it becomes clear that the received power, overestimated by the propagation prediction model, and the large-scale signal fluctuations of the received signal from BS 6238 are mainly caused by the strong shadowing effects by buildings HvA1 and HvA2. Although in the shadowed areas part of the energy is reflected back via the upper half of buildings F1-F4, the total amount of received power is below that of BS 7352. The underestimated, or relatively high received power from BS 7352, is mainly caused by through-building propagation, reflections from rough building surfaces (F1-F4) and higher-order reflections. These effects cause the waves to propagate rather easily into and through this street.

The results also show that the prediction errors in the stochastic empirical propagation prediction model are mainly caused by the limited amount of information about the environment that is taken into account and important propagation mechanisms, such as reflections, that are not included directly in the model. Furthermore, it is shown that in case of irregular surfaces the effects of an entire surface can be important instead of those from a single specular point. Other type of models, e.g., ray-based models, will need to be considered in order to include propagation effects that cause energy to arrive via other paths than the direct path only. When a more in-depth analysis of a specific area is required, the use of a ray-based prediction tool can then be used to improve the network configuration.

5.5 Conclusions

In this chapter, the 3-D high-resolution channel sounder was used in the framework of a collaboration between TU/e, TNO ICT and KPN as a diagnostic tool in a dense urban environment in order to identify the causes of unexpected interference and signal degradation in an active cellular network. It was shown that the novel measurement system can be configured so as to operate in similar propagation conditions to those that influence the operation of live operating systems in order to identify the causes of unexpected interference and desired signal degradation in the corresponding active cellular system. The high-resolution capabilities and the combination of omnidirectional video images and measurement data make it possible to directly identify propagation effects in a real network scenario while moving through it.

The results underline the limitations of current propagation models used by operators in existing and, even more importantly, future networks. It was shown that shadowing and reflections from irregular building structures are important phenomena that are currently not accurately modelled and this can lead to network problems in more complex environments. More accurate propagation modelling is needed in complex environments and the use of advanced propagation measurements can help provide the insight needed for their development. The next chapter describes a multidimensional data clustering technique that can aid in this process.

In summary, the main contributions and innovations of the work presented in this chapter are:

- Results were presented from a diagnostic analysis of the propagation effects inside an operational network using the recently developed high-resolution measurement system. The main propagation mechanisms and the causes of unexpected signal degradation and interference were successfully identified with the help of omnidirectional video data.

- It was shown that shadowing and reflections from irregular building structures can be dominant propagation mechanisms.

- Current propagation models used by operators are not suitable and accurate enough to predict propagation behavior in complex urban environments. It is thus concluded that more accurate propagation modelling is required.

6

Multipath cluster identification

6.1   Introduction

The results in the previous chapter confirmed the need for more accurate propagation
knowledge and improved propagation modelling. The results obtained using the 3-D
high-resolution channel sounder measurement system described in Chapters 4 and
5 are of significant importance in the field of propagation research, but additional
processing is required before the results can be used for further analysis. Since the
multipath estimates obtained in physically nonstationary radio channels tend to ap-
pear in elongated cluster-like structures within the multidimensional space, see for
example Fig. 5.5 on page 84, clustering of the multidimensional data can significantly
improve the data representation and support further data analysis. Since clustering
by visual inspection of the data becomes difficult due to the size and the multidimen-
sional nature of the data, automatic clustering becomes necessary. Once clusters are
obtained, they can be related to physical objects that interact with the propagating
waves. The results are important for the understanding of the propagation mecha-
nisms and the modelling of scattering, as well as the verification and calibration of
deterministic propagation prediction models. This information can also be very help-
ful for the identification of multidimensional scattering sources, which is information
that is used as input to geometrical-based channel models, such as the Ilmprop model
described in [8, 9].

This chapter describes the clustering of multidimensional measurement data. Firstly,
Section 6.2 introduces multipath clustering and presents the method used to cluster
the estimation results. Subsequently, the definition of intra-cluster angular spread

is presented. Secondly Section 6.3 presents the scenario and the procedure of several experiments in which the transmitter is placed above and below average rooftop level. The results of these experiments and their analysis are presented in Sections 6.4 and 6.5. The results in Section 6.4 include a comparison with simulation results obtained from a commercially available deterministic propagation prediction tool. The results in Section 6.5 include the analyses of the inter-cluster angular spread, related to specific objects, in both the azimuth and elevation domain using the clustered measurement data. Finally, conclusions are drawn in Section 6.6.

6.2   Multipath clustering

The automatic clustering of measurement channel data obtained in physically nonstationary radio channels was recently addressed [84,85]. A method was proposed that is based on the sequential clustering of windowed multipath estimates using a K-means clustering algorithm, [86], and the tracking of cluster centroids in consecutive data windows. Although the algorithm is fast and useful for analysing large measurement records, its application is limited. Because K-means is a heuristic (initial guess), hill-climbing algorithm, the algorithm is guaranteed to converge to a local, but not necessarily global optimum. This means that the clusters found can not be optimal and the choices of the initial clusters affect the quality of the results. Although this problem can be mitigated by doing multiple restarts, the result is that the shapes of the clusters may vary between multiple runs. The pairing of the clusters between two consecutive windows can be difficult because it requires the size of the sliding window to be correctly selected to prevent merging of multiple clusters to one, or creating too many clusters.

6.2.1   Clustering method

Instead of clustering the measurement data using sliding windows, as described in [85], this section proposes a hierarchical clustering method to cluster the measurement data. Although this method is not fast, the data pool is clustered as a whole, which guarantees the convergence to a global optimum and prevents any difficulties with pairing clusters from consecutive windows. The problem of scaling data with different dimensions is circumvented.

The data to be clustered consist of a total of W estimated multipath components (MPCs), each of which is described by a position in a four-dimensional space, i.e. time-delay (τ), AOA in azimuth (ϕ), AOA in elevation (θ) and measurement snapshot-set number (k). Additionally, the estimated power (P) is also available for each estimate. The task of the clustering algorithm will be to group estimates that have similar angles and delays that slowly evolve over time, i.e., that are close together in the four-dimensional space. Since the acquired data are obtained with a moving receiver, multipath components will evolve over time and will tend to appear in strings or elongated clusters within the four-dimensional space.

Set cluster $c = 1$

All data
assigned to
clusters?

YES

STOP

NO

Find **MPC**$_i$ with
highest power not yet
assigned to a cluster

**MPC
data**

Assign **MPC**$_i$
to cluster c

Find nearest
neighbour, **MPC**$_j$, of
cluster c not yet
assigned to a cluster

$\vartheta_{ij} \leq t_\vartheta$
$\Delta\tau_{ij} \leq t_\tau$
$\Delta\mathbf{k}_{ij} \leq t_k$

NO

$c = c + 1$

YES

Assign **MPC**$_j$
to cluster c
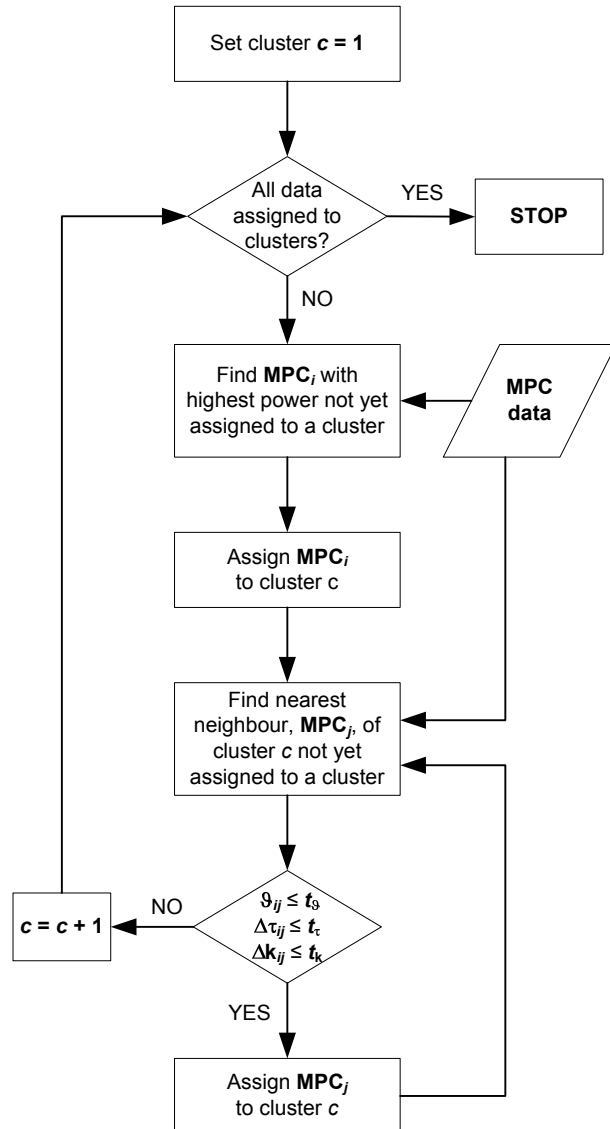
Fig. 6.1: Single linkage clustering algorithm.

Single linkage clustering, also called the nearest-neighbour method of clustering, is an agglomerative hierarchical clustering method and known to be well suited to detect chains or elongated data structures [87]. The single linkage algorithm used here is given in Fig. 6.1. Here, the angle (ϑ_{ab}) between MPC_a and MPC_b is defined as the angle between the two three-dimensional vectors pointing in the direction of the estimates a and b, as shown in Fig. 6.2. The angle ϑ_{ab} is defined by their azimuth and elevation angles, in the following manner

$$\vartheta_{ab} = \cos^{-1} \left\{ \begin{pmatrix} \cos\phi_a \cos\theta_a \\ \sin\phi_a \cos\theta_a \\ \sin\theta_a \end{pmatrix} \cdot \begin{pmatrix} \cos\phi_b \cos\theta_b \\ \sin\phi_b \cos\theta_b \\ \sin\theta_b \end{pmatrix} \right\}. \tag{6.1}$$
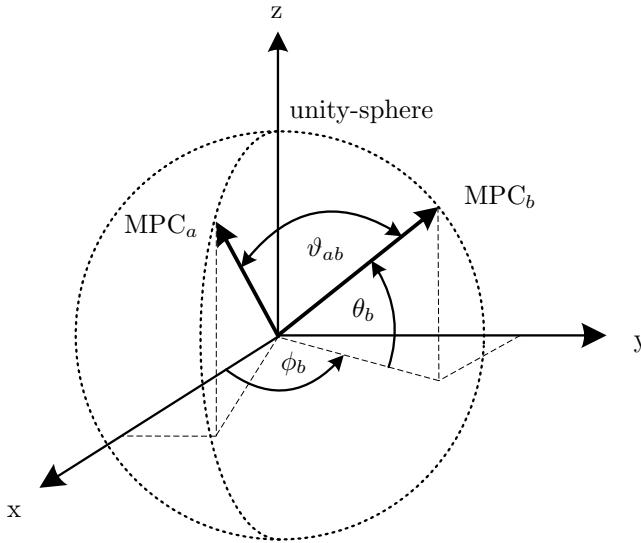
Fig. 6.2: Geometrical definition of the angle (ϑ_{ab}) between MPC_a and MPC_b that point in the direction of the estimates a and b.

The distances in delay and snapshot sets are obtained as $\Delta\tau_{ab} = |\tau_a - \tau_b|$ and $\Delta k_{ab} = |k_a - k_b|$, respectively. Furthermore, t_ϑ, t_τ and t_k are the thresholds for each domain. The values for t_ϑ and t_τ are set according to the resolution of the measurement system, i.e. $t_\vartheta = 5°$ and $t_\tau = 20$ ns. The value for t_k was set to 10 snapshot sets since it was found to produce satisfying clustering results. The algorithm will proceed in clustering all data into clusters according to the thresholds set for each domain, meanwhile reducing the data set that needs to be searched for nearest neighbours.

6.2.2   Cluster angular spread

The clustered estimation data contain high-resolution azimuth as well as elevation information, which makes it possible to analyse the intra-cluster angular spread in both domains, i.e., RMS cluster azimuth spread (CAS) and RMS cluster elevation spread (CES). The mean azimuth angle in a cluster, $<\phi>$, can be determined as [88]

$$<\phi> = \frac{\int_{-\pi}^{\pi} \phi P(\phi) d\phi}{\int_{-\pi}^{\pi} P(\phi) d\phi}, \tag{6.2}$$

and the CAS, σ_ϕ, is determined as

$$\sigma_\phi = \sqrt{\frac{\int_{-\pi}^{\pi} (\phi - <\phi>)^2 P(\phi) d\phi}{\int_{-\pi}^{\pi} P(\phi)}}, \tag{6.3}$$

where $P(\phi)$ represents the continuous-power azimuth spectrum.

For each cluster only a limited number of MPCs are available, and as a result the power azimuth spectrum for each cluster is discrete. The CAS is therefore determined by rewriting Eq. (6.2) and (6.3) as

$$<\phi> = \frac{\sum_{i=1}^{I} \sum_{n=1}^{N^{(i)}} \hat{\phi}_n^{(i)} P_{\phi_n}^{(i)}}{\sum_{i=1}^{I} \sum_{n=1}^{N^{(i)}} P_{\phi_n}^{(i)}}, \tag{6.4}$$

and

$$\hat{\sigma}_\phi = \sqrt{\frac{\sum_{i=1}^{I} \sum_{n=1}^{N^{(i)}} |\hat{\phi}_n^{(i)} - <\phi>|^2 P_{\phi_n}^{(i)}}{\sum_{i=1}^{I} \sum_{n=1}^{N^{(i)}} P_{\phi_n}^{(i)}}}. \tag{6.5}$$

Here, N represents the number of estimated MPCs in the ith delay bin out of a total of I delay-bins that belong to the corresponding cluster. $\hat{\phi}_n^{(i)}$ represents the estimated azimuth angle of the nth MPC in the ith delay-bin. The value for $P_{\phi_n}^{(i)}$ corresponds to the power of $\hat{\phi}_n^{(i)}$. Values for the CES are determined in a similar way.

It would be of interest to analyse the power-azimuth and power-elevation *distribution functions* for the different MPC clusters. However, the specular-wave model, used in the estimation of the MPCs, prevents reliable estimates for these distribution functions [89].

6.3   Experiments

This section presents the scenario and the procedure used to obtain clustered measurement results by applying the clustering method presented in Section 6.2.1. The scenario and procedure apply to the results that are presented in Sections 6.4 and 6.5. The data are obtained from outdoor experiments performed on the campus of the Technische Universiteit Eindhoven (TU/e) in Eindhoven, the Netherlands using the 3-D high-resolution channel sounder presented in Chapters 2 and 3.

6.3.1   Scenario

The measurement scenario is presented in Figs. 6.3 and Fig. 6.4, where Tx(1) and Tx(2) mark the transmitter positions for the above and below rooftop scenario, respectively. The scenario is characterised by several high buildings and scattered vegetation. The transmitting antenna (Tx) consisted of an 8-dBi waveguide horn antenna with an azimuthal half-power-beam-width of 55°. In the above rooftop scenario, the Tx antenna, Tx(1), was positioned outside, at 57 m above ground level and pointed southwards at a tilting angle of 20° downward. In the below rooftop scenario, the Tx antenna, Tx(2), was positioned inside a steel, elevated walkway, behind glass, at 5 m above ground level and pointed eastwards at a tilting angle of 20° downward. In the case of the moving receiver Rx(1) marks the beginning of the first measurement trajectory in combination with Tx(1) and Rx(2a) marks the beginning of the second measurement trajectory in combination with Tx(2). Additionally, measurements are performed with a static receiver, marked with Rx(2b). The measurement trajectories are represented by the white dotted lines and the numbers along the trajectory correspond to the snapshot set numbers. The white solid lines represent building database information that is used in simulations that are presented in Section 6.4.2 on page 101.
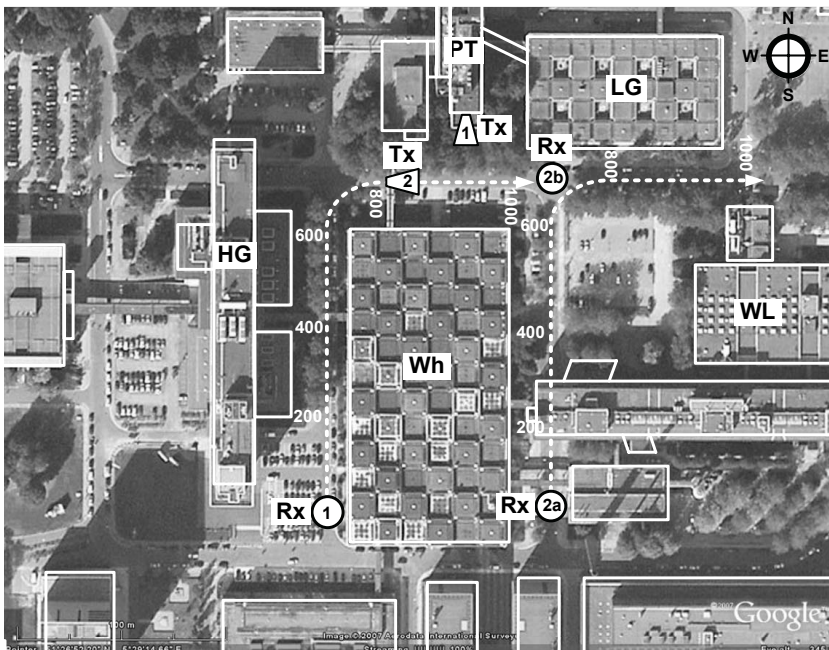
Fig. 6.3: Layout of the measurement site. The white dotted lines represent the measurement trajectories of scenario 1 and 2. The values along the trajectory correspond to the snapshot set numbers. The white solid lines represent building database information. Copyright: Google Earth, http://earth.google.com

(a)   (b)
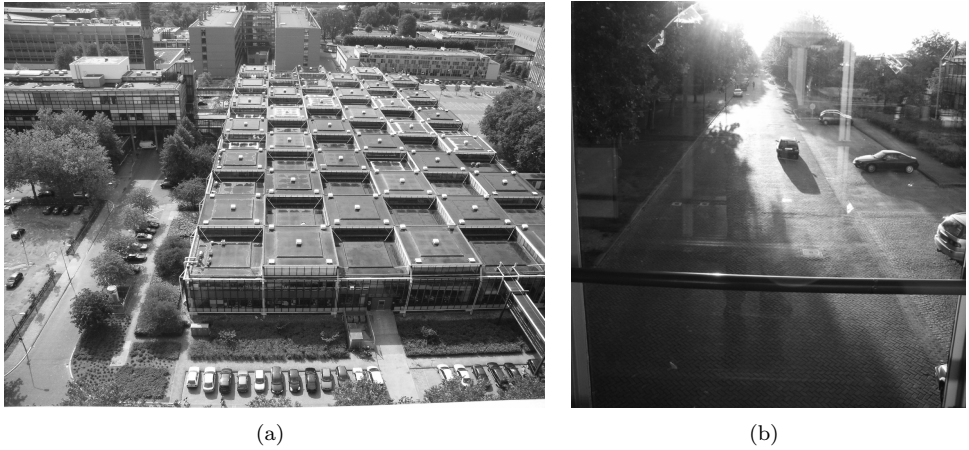
Fig. 6.4: Photo from the transmitter point of view at (a), transmitter setup Tx(1) and (b) transmitter setup Tx(2).

6.3.2   Procedure

A single measurement snapshot is taken every 6.5 μs and sets of $K = 10$ consecutive snapshots are used as input for the Unitary ESPRIT algorithm. As a result, the angle-delay characteristics of the channel are estimated every 65 μs. In each of the measurement scenarios presented herein a total number of 1000 snapshot sets are used, which results in a measurement duration of 65 seconds. In the scenarios with a moving receiver, the receiving antenna (Rx) was moved at a nearly constant speed of about 13.5 km/h along a trajectory of approximately 245 m. This effectively means that a single angle-delay estimate of the channel is available every 0.25 m, which corresponds to 1.875 wavelengths. MPCs with very low power ($<$ -100 dBm) are removed from the data set since they do not contribute significantly. The clustering algorithm is applied to the resulting data set. During the measurement campaign omnidirectional video data were captured from the receiver perspective using a omnidirectional video camera mounted directly underneath the antenna array. The azimuth angles are in accordance with the orientation of the measurement vehicle, where 0° corresponds to the back of the vehicle and $180/-180°$ corresponds to the front.

6.4   Comparing measurements and predictions

This section presents the processed measurement results and the clusters obtained from it for the scenario where the transmitter is positioned above the average rooftop level with Tx(1) and Rx(1). Additionally, the results are compared with those from a deterministic propagation prediction tool.

(a)

(b)
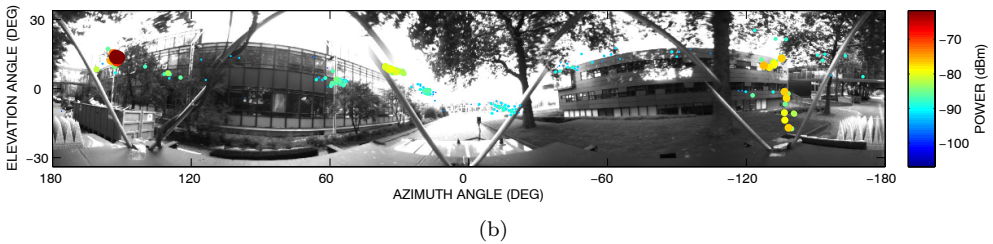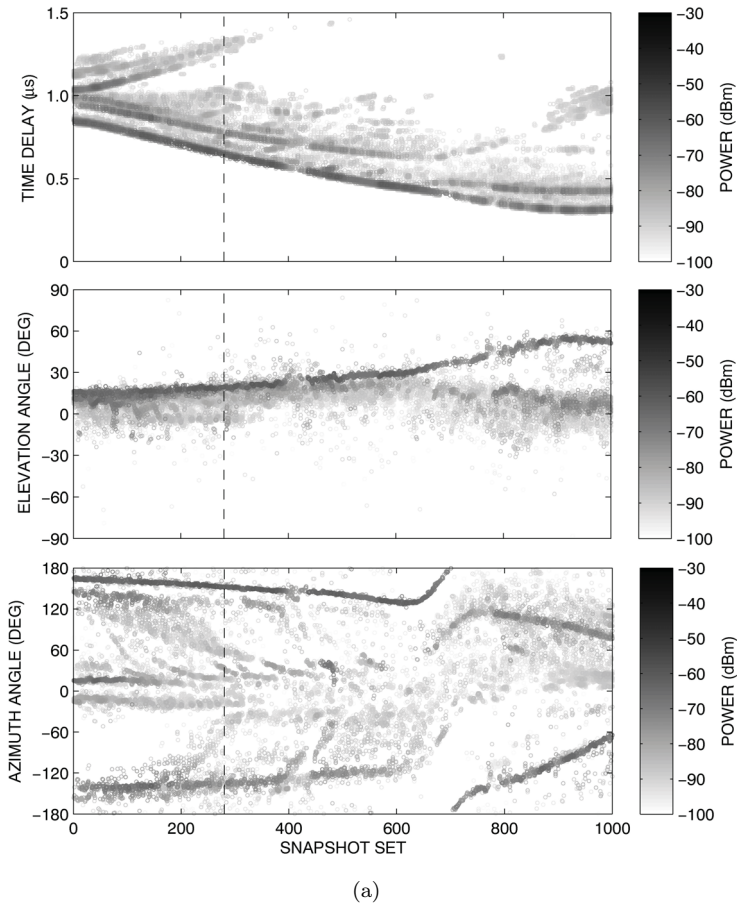
Fig. 6.5: Results of (a) estimated AOAs and delays of MPCs for the scenario with Tx(1) and Rx(1) and (b) AOAs of MPCs superimposed on omnidirectional video data at snapshot set $k = 280$.
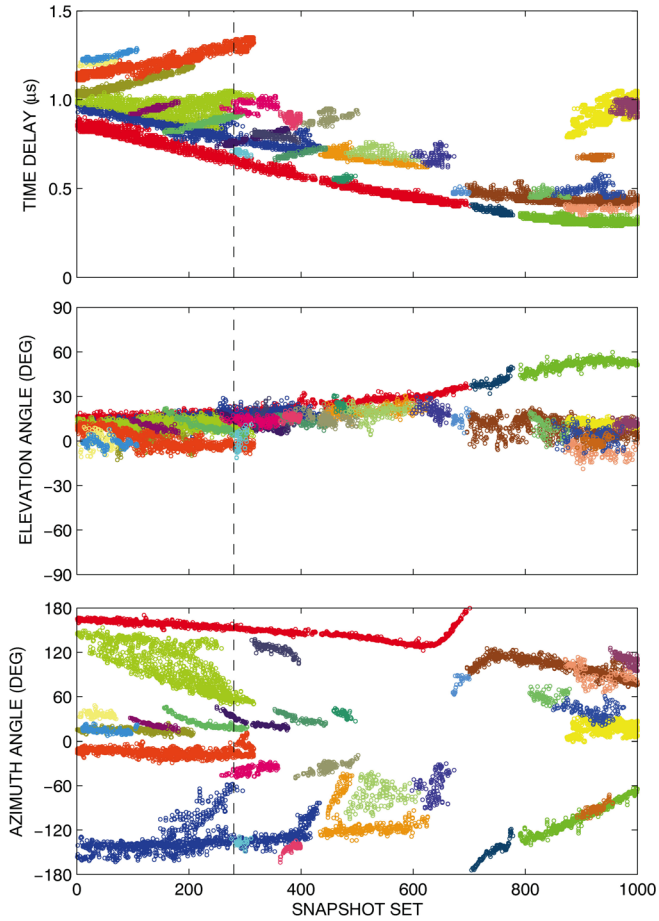
(a)

(b)

Fig. 6.6: Results of (a) the estimated AOAs and delays of the 30 largest MPC clusters, each in their own colour, determined from the estimated MPCs for the scenario with Tx(1) and Rx(1) and (b) AOAs of MPCs clusters superimposed on omnidirectional video data at snapshot set $k = 280$.

6.4.1   Measurement results

The results in Fig. 6.5 (a) present a set of $W = 20288$ MPC estimates in the angle-delay domain obtained by applying 3-D Unitary ESPRIT to the measurement data. The grey levels indicate the absolute received power levels of the individual MPCs in dBm. The evolution of several strong MPCs, the strongest being the line-of-sight (LOS) component, can clearly be observed in all domains. The change in delay and angle of the LOS component is in agreement with the scenario: the time delay decreases, the elevation angle increases and the azimuth angle changes with respect to the orientation of the receiver as the receiver moves towards the transmitter. Close to snapshot set $k \simeq 400$ a short and sudden drop is observed in the signal level of the LOS component. This is caused by passing underneath an elevated walkway made out of steel. After the turn ($k \simeq 700$) the elevation angle increases by $50°$ and the level of the direct component drops again since LOS is obstructed. In addition to several strong MPCs, many weaker and scattered components are visible throughout the measurement; their components can be related to trees and other objects by using the captured video data. An increase of these scattered components is observed when the receiver is surrounded by vegetation (starting close to $k \simeq 200$). Fig. 6.5 (b) presents an example of a single video frame of snapshot set $k = 280$ with the angular estimation results superimposed on it. The size and the grey-level of the markers represent the signal intensity. The dotted line in Fig. 6.5 (a) corresponds to snapshot set $k = 280$.

In Fig. 6.6 (a) the results of applying the clustering algorithm to the measurement data are presented. The colours indicate the different MPC clusters and connect them across the different domains. The 30 largest clusters in terms of total cluster size and total cluster power are presented. The results show that the clustering method can successfully distinguish many different clusters of different size and life-time within the data. These clusters can be related directly to the physical environment by comparing them with the captured omnidirectional video data. For example, between the interval $100 \leq k \leq 500$ a series of 5 clusters appear and disappear in sequence (•, •, •, •, •). They are arc shaped in both angular domains and have a linearly increasing delay. These clusters are caused by reflections from the vertical elevated sections of building Wh in the center of Fig. 6.3 and are also visible in Fig. 6.4 (a). A scattering effect caused by through-building propagation of the same building is visible between $0 \leq k \leq 300$ (•). This cluster has a large delay and angular spread in azimuth with the center of the cluster moving from $\phi \simeq 160°$ to $50°$. Although the lifetimes of all MPC clusters are different, they generally tend to evolve rather slowly along the trajectory. In Fig. 6.6 (b) the clusters obtained from the measurements superimposed on omnidirectional video data are presented. Here, the colour of the markers represents the different clusters in accordance to Fig. 6.6 (a). This representation directly relates the estimation results and the clusters to the actual environment. When all the frames of the entire trajectory are combined an illustrative video is created in which the MPCs and MPC clusters can be observed and tracked.

6.4.2   Simulation results

In Chapter 5 it was observed that the use of deterministic propagation models is expected to improve propagation prediction results. To compare measurements against the results obtained from such a model, a commercial deterministic propagation prediction tool was used [90]. Simulations were performed for the above rooftop scenario using information from a 3-D building database, the top view of which is shown by white solid lines in Fig. 6.3. A trajectory, of 245 m, similar to the measurement trajectory was defined and a step size of 1.8 wavelengths was used in accordance to the measurements. The height and orientation of the receiver and transmitter were correctly set and the actual antenna patterns were used. Values for the signal parameters and cable losses were in accordance with the measurements. The simulation is based on the principle of ray launching and considers reflection, penetration and diffraction as the most dominant phenomena. For the building walls a thickness of 0.5 m was assumed along with a relative permittivity $\epsilon_r = 3 - 0.4j$, corresponding to reinforced concrete [91]. In accordance with the measurements, the noise floor was set to -100 dBm. Except for the minimum power level, no other limitations on the number of interactions were set. The simulation results are presented in Fig. 6.7. In Fig. 6.8 the results from clustering the prediction data show that cluster boundaries can be determined to isolate the effects and to compare the clusters with those from the measurements. The results show that there is a good agreement for the LOS component between the simulations and the measurements presented in Fig. 6.5 and 6.6 on pages 98 and 99, in power as well as in angle-delay domain. Some of the other weaker components have a lower predicted power, are less spread in the angle-delay domain or are missing completely in the simulation results. Possible reasons for the mismatch between the measurements and the predictions are an inaccurate or incomplete building database, incorrect (building) material properties (ϵ_r), incorrect modelling of irregular surfaces, vegetation and small objects. The effects of errors in the predictions, especially in the angular domain, can have a large impact on the design of multi-antenna systems for cellular networks and again illustrates the need for improving propagation predictions. The results from clustered high-resolution AOA measurements, as presented here, can be very helpful for the identification, improvement and calibration of deterministic propagation prediction models. The intra-cluster properties from clusters obtained from measurements can, for instance, be used to calibrate simulation parameters related to corresponding clusters from the simulations.
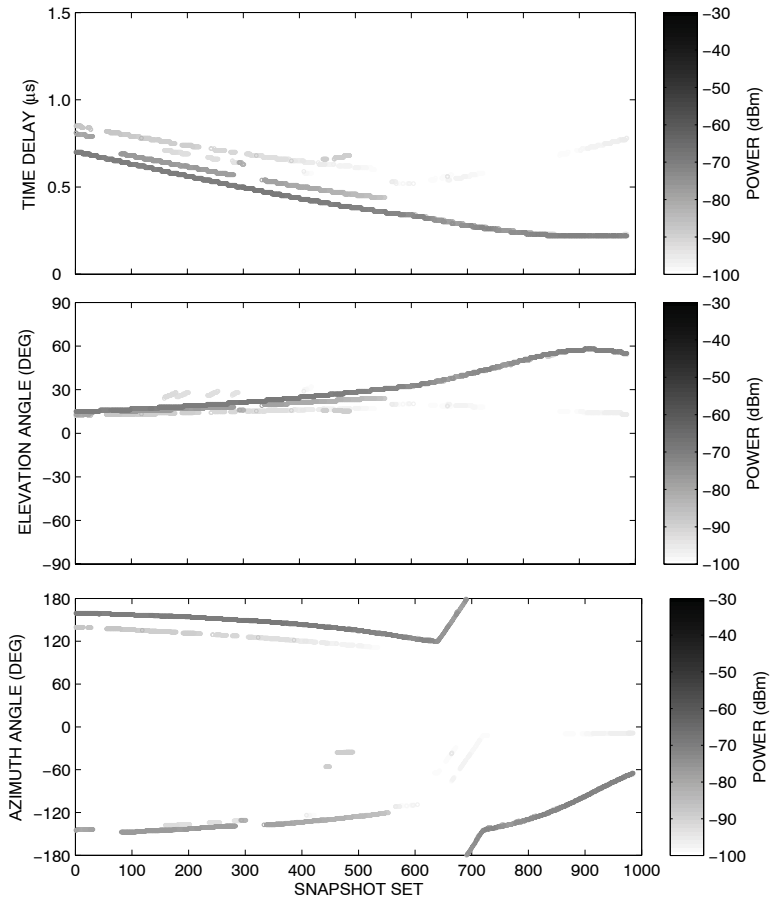
Fig. 6.7: Results of the AOAs and delays of the MPCs determined from ray-launching simulations for the scenario with Tx(1) and Rx(1).
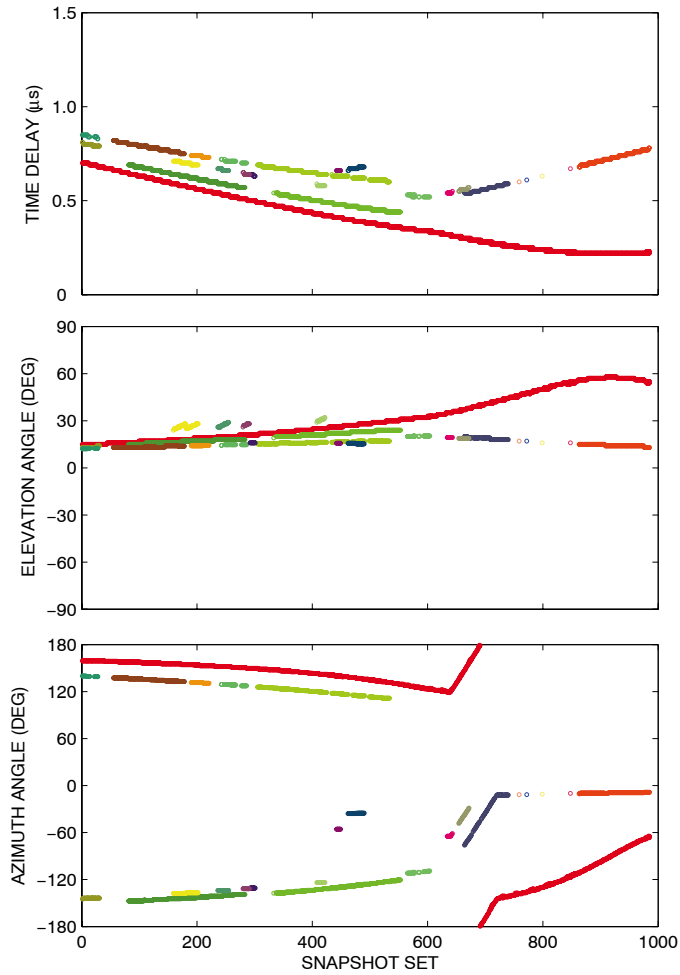
Fig. 6.8: Results of the AOAs and delays of all the MPC clusters, each in their own colour, determined by applying the ray-launching simulation results to the clustering algorithm for the scenario with Tx(1) and Rx(1).

6.5   Effects of receiver movement

This section reports the results from measurements and modelling conducted for the below rooftop scenario in which the transmitter antenna was located at position Tx(2). In addition, intra-cluster angular dispersion is observed and evaluated. In order to investigate the effect of a *moving* receiver on the results in the same environment, the results of both a moving and a static receiver are presented, Rx(2a) and Rx(2b), respectively. Furthermore, the CAS and CES are determined for clusters that can be related directly to specific objects. Note that an accurate estimate for the intra-cluster delay-spread cannot determined, because the *delay* resolution of the measurement system is limited to 10 ns.

6.5.1   Moving receiver

The results in Fig. 6.9 present the thirty strongest MPC clusters that contribute to 98% of the total power available in the MPCs for the experiment using Tx(2) and Rx(2a). At the beginning of the trajectory building obstructions cause a significant reduction in the received power. After snapshot set $k \simeq 300$, changes in the channel caused by moving the receiver along the trajectory are immediately visible in the data. The change of several strong MPC clusters, the strongest being the LOS component , can clearly be observed. The change in delay and angle of the LOS component is in agreement with the scenario, i.e. the time-delay first decreases and then increases again after taking the turn, and the azimuth angle changes with respect to the orientation of the receiver as the receiver takes the turn and moves away from the transmitter. Beside several strong MPC clusters, many weaker and scattered components, caused by trees and other objects, are also visible throughout the measurement. At snapshot set $k \simeq 650$ the receiver is closest to the position of static receiver setup Rx(2b), presented in the next section. In order to characterise the dispersive effects of the individual clusters, mean values for CAS and CES of different clusters that can be related to specific buildings and objects are determined and summarised in Table 6.1. Note that due to the plane wave assumption in the Unitary ESPRIT model only valid estimates for the angular spread can be determined, while estimations for the angular distribution function are not reliable [89]. The CAS and CES values presented here serve merely as an indication and show that they can be characterised by using measurements obtained while moving trough an urban environment. Although the values for the angular spread are small, differences between clusters are observed that can be related to their origin. More details on the cluster origin and the effect of the movement of the transmitter on the angular spread are discussed in the next section, where measurements using a static receiver are presented.
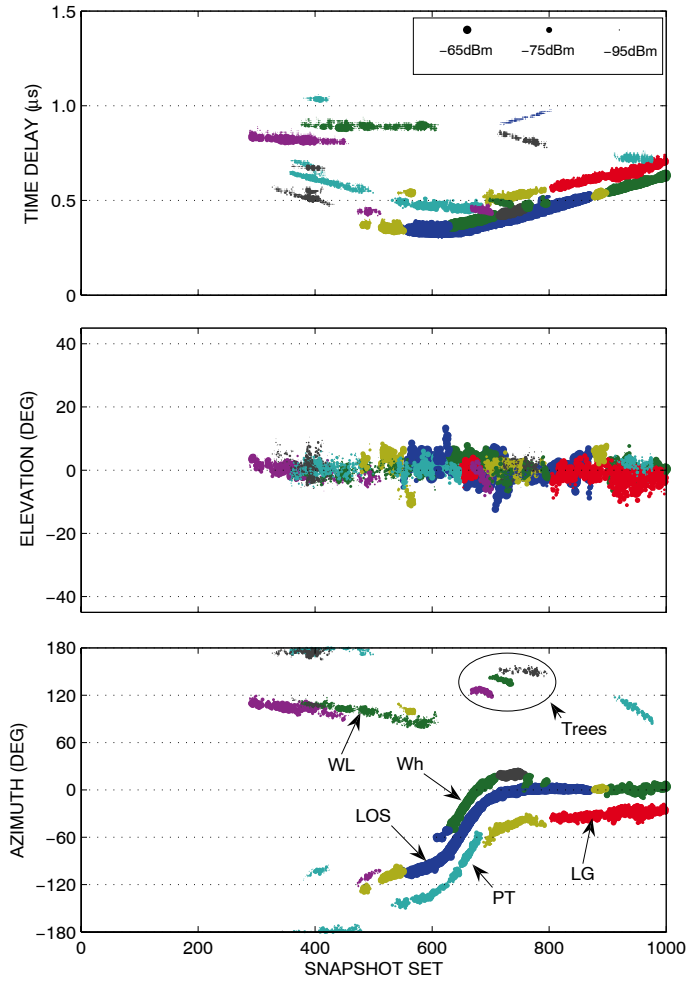
Fig. 6.9: Results of the AOAs and delays of the MPC clusters for the scenario with Tx(2) and Rx(2a). The thirty most dominant clusters are presented, each in their own colour. The size of the markers corresponds to the power of the MPCs, where the largest marker corresponds to the highest received power.

Table 6.1: Mean values for CAS and CES for different objects determined from measurements.

Receiver setup: Rx (2a)	Mean CAS (deg)	Mean CES (deg)
LOS	0.4	0.6
Building Wh	0.6	0.4
Building PT	0.8	0.5
Building WL	1.1	0.5
Building LG	1.7	1.0
Tree trunks	0.6	0.6
Receiver setup: Rx (2b)	Mean CAS (deg)	Mean CES (deg)
LOS	0.3	0.7
Building Wh	0.6	0.5
Building PT	0.4	0.3
Building HG	0.9	2.4
Moving truck 1	0.5	0.5
Moving truck 2	1.2	0.7
Moving car	0.7	0.9
Moving bicycle	1.2	0.8
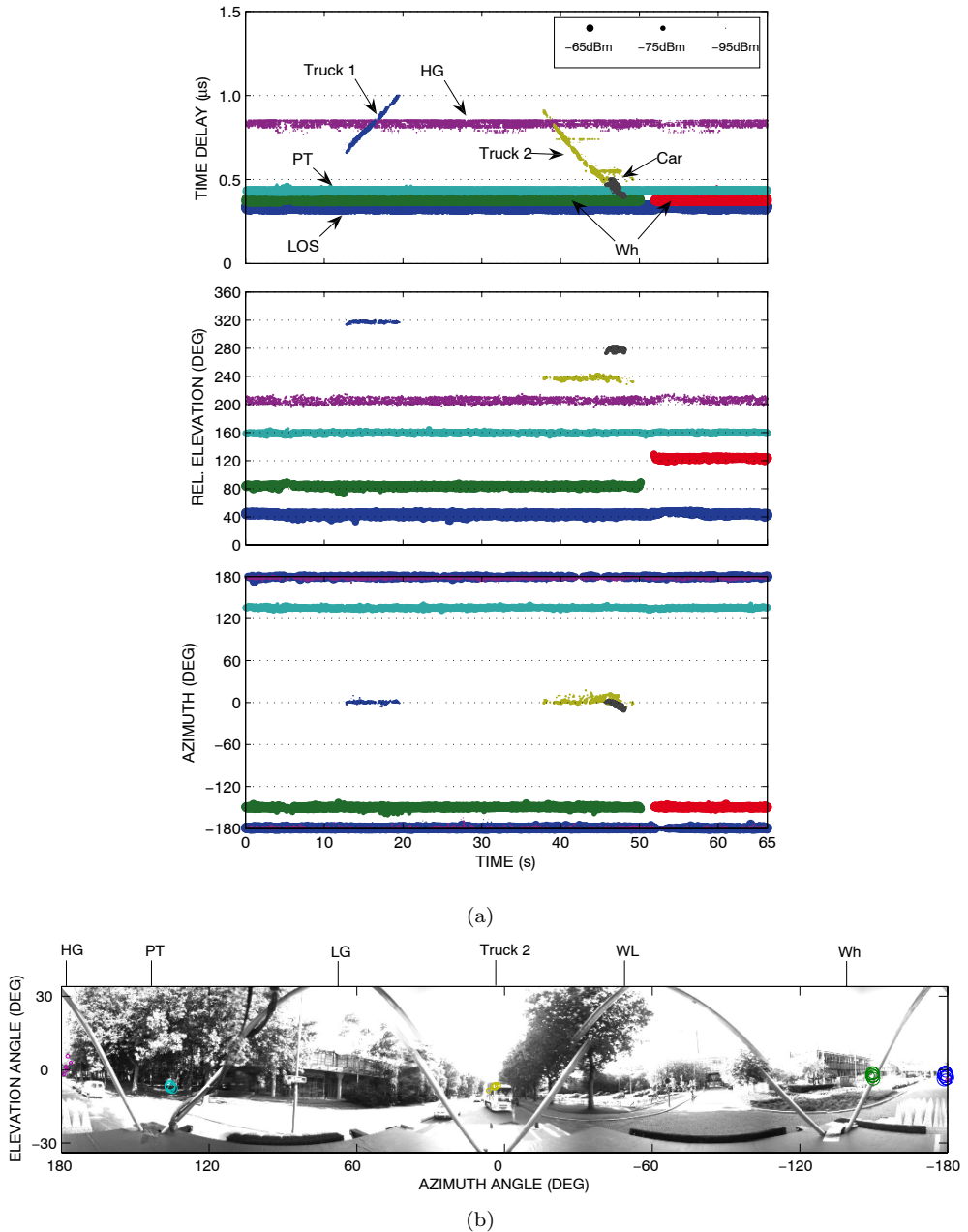
Fig. 6.10: Results of (a) the eight most dominant clusters for the scenario with Tx(2) and Rx(2b), each in their own colour and (b) clusters superimposed on omnidirectional video data at time instance 45 s. The received power is represented by the size of the markers, where the largest marker corresponds to the highest received power. Note that in (a) the elevation values for each cluster are offset by multiples of 40 degrees.

6.5.2   Static receiver

The results in Fig. 6.10 (a) present the eight strongest MPC clusters in the angle-delay domain that contribute to 97% of the total power available in the MPCs in the case of Rx(2a). Each MPC cluster is represented by its own colour. The size of the marker indicates the absolute received power levels of the individual MPCs in dBm. Note that in Fig. 6.10 (a) the elevation angles are offset by multiples of 40 degrees for each cluster for a better representation. Although the measurement is performed under static conditions channel fluctuations are visible in the measurements. The line-of-sight (LOS) component, (●), visible near $\phi \simeq 180/\text{-}180$, has the shortest delay and the highest received power. By using the captured video data, shown in Fig. 6.10 (b), the other MPC clusters can be related to the physical environment to find their physical scattering sources. The MPC clusters result from interactions with building Wh, (●,●), building PT, (●) and building HG, (●). The two clusters that are visible as slopes in the time-delay domain, (●,●), are caused by trucks moving towards and away from the transmitter. One of the trucks also causes the discontinuity related to the cluster from building Wh. Although the effects of trucks were most dominant, cars, (●), and even bicycles, traffic signs and lamp posts can be identified as physical scattering sources using the captured video data. In all clusters, rapid variations of the spread, caused by small subtle movements of the environment are visible as well as larger variations caused by moving objects such as cars and trucks. Mean values for CAS and CES of different buildings and objects in the measurements are summarised in Table 6.1. In Fig. 6.11 the CAS and CES over time of the four most dominant clusters are presented. Here, the rapid variations of the spread are more clearly visible. Apart from the larger fluctuations that are caused by the changing environment, small variations are caused by the variance of the estimator due to the limited accuracy and resolution. These effects are minimised by averaging the CAS and CES values over a large number of snapshots and makes the identification of the mean CAS and CES values acceptable.

It can be observed that the mean CAS and CES values can be different within a cluster and vary between different clusters. The LOS component, which ideally should have a very low angular spread, has a mean CAS of 0.3° and a mean CES of 0.7°. Although quite small, the observed angular spread can be explained by the fact that the Tx antenna is positioned inside an elevated walkway, shown in Fig. 6.4 (b), with a steel floor and ceiling which causes additional reflections, more dominantly in elevation. The second cluster, related to building WH (●), shows a lower CES but an increased CAS. The spread is probably caused by the irregularities of the building, which contain vertical steel tubes at regular intervals. The cluster related to building PT, (●), shows only a small angular spread in both domains. This can be explained by the fact that the face of the building is almost plane metal at the reflection point, which creates a more specular reflection. The cluster related to building HG, (●), which can also be identified due to its larger propagation delay, has much more spread in both elevation and azimuth. This can be explained by the irregular surface.
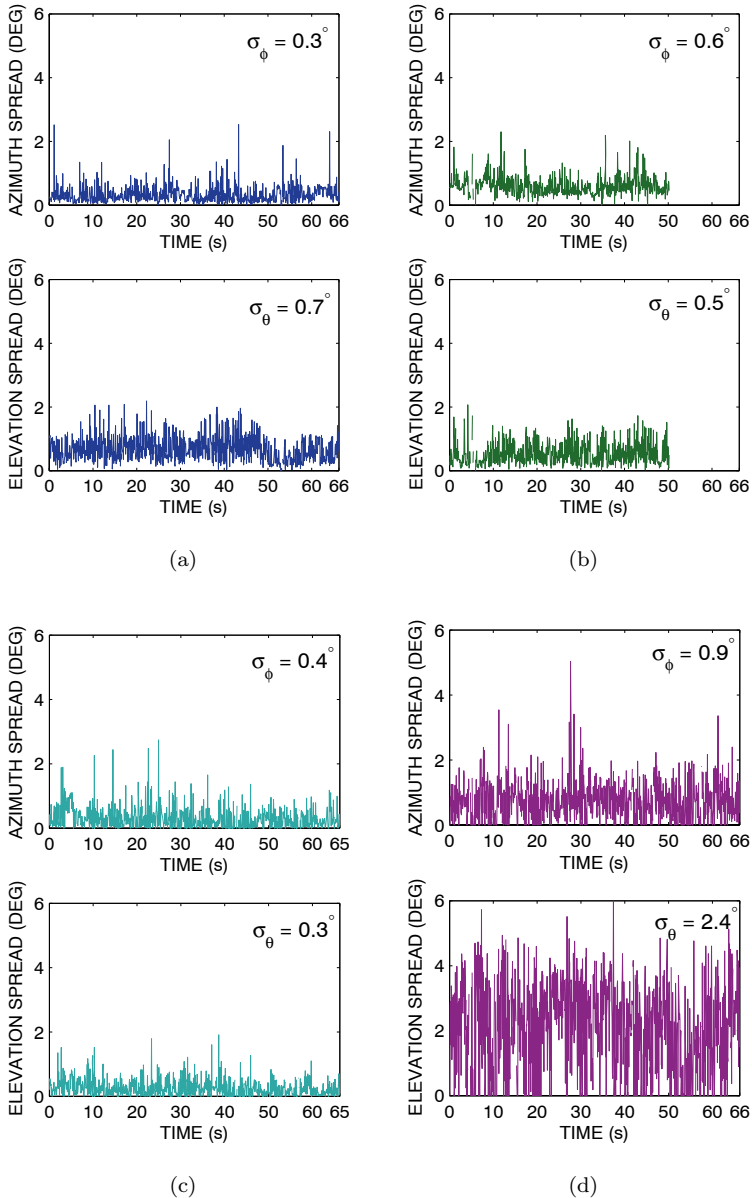
Fig. 6.11: Values for CAS and CES over time for the scenario with Tx(2) and Rx(2b), for (a) cluster LOS, (b) cluster Wh, (c) cluster PT and (d) cluster HG. The colours correspond to those in Fig. 6.10 on page 107.

In general, the mean values of the CAS and CES are similar in both the mobile and the static measurement. It was found that the values for the CAS range between $0.3°$ and $1.7°$, and for the CES between $0.3°$ and $2.4°$. Although larger values are observed in other measurements, the mean values presented here are generally smaller than for example the results in [92, 93], where similar analyses in the azimuth domain were performed. Here, values for the azimuthal spread vary between $2° - 11°$.

6.6   Conclusions

In this chapter, a method to cluster multidimensional estimation data obtained with a 3-D high-resolution channel sounder is presented. It was shown that the method can successfully separate clusters in multidimensional MPC estimation data obtained in physically nonstationary radio channels. From the clusters, the scattering effects of specific objects can be isolated and the angular dispersion caused by scattering by these objects in azimuth as well as in elevation can be analysed.

The results of the measurements and the clustered data were compared with the results obtained from a 3-D deterministic propagation prediction tool and it was found that in the simulations a significant number of MPCs were absent from the prediction results. Additionally, it was found that angular spreads predicted from measurements are generally greater.

It was shown that, in a static scenario, subtle changes in the channel cause small but rapid variations of the angular spread, whereas the movement of objects causes larger but more gentle variations. The amount of angular spread in azimuth or elevation can be quite different and values for the CAS range between $0.3°$ and $1.7°$, and for the CES between $0.3°$ and $2.4°$. The angular spread may be included in propagation predictions as an additional statistical component to improve the quality of the propagation prediction models, as will be explained in the next chapter.

In summary, the main contributions and innovations of the work presented in this chapter are:

- A method to cluster multidimensional estimation data obtained with a 3-D high-resolution channel sounder is presented in Section 6.2 and was previously published by the author in [40, 41].

- The results from several outdoor experiments are presented and used to demonstrate application of the clustering algorithm. The results from this are then compared to the results from a 3-D deterministic propagation prediction tool, as presented in Section 6.4. The scattering effects of specific objects can be isolated and the angular dispersion of these objects in azimuth as well as in elevation can be analysed, as presented in Section and 6.5. The results were previously published by the author in [40, 42].

7

Modelling stochastic scattering for ray-tracing

The prediction of radio propagation by ray-tracing or ray-launching generally assumes that reflections from buildings and other seemingly plane surfaces occur as specular reflections. The effects of diffuse scattering and angular dispersion caused by material irregularities are often not accounted for. The results in the previous chapters have demonstrated that in reality the specular reflection component exhibits angular dispersion. This causes multiple rays to arrive at the receiver from the specular direction and in a small angular sector centered on it. Until recently, these effects were not considered important enough for consideration in the design of mobile radio systems, and their inclusion in modelling was avoided, as it was considered that this would result in a dramatic increase in model complexity.

For next generation 4G radio systems (using e.g. smart-antennas, MIMO) the angular dispersion of radiowaves is becoming increasingly important. Due to dispersion, waves no longer have well-defined AOAs. In beamforming systems this strongly influences the effect of nulling out interference or directing a beam to obtain a maximum signal level [21]. In MIMO systems the angular dispersion also has a major effect on capacity and diversity gain [23].

These effects, need to be incorporated in deterministic propagation prediction models in an efficient way. The problem is addressed in several recent publications and methods have been proposed that include diffuse scattering, which causes angular dispersion [16, 19, 20, 94–98]. The reduction of the model complexity and the ability to calibrate them using only a limited number of measurements are important issues.

This chapter describes the modelling of scattering, caused by surfaces which have "random" irregularities, for implementation in ray-tracing software. Firstly, Section 7.1 gives a short introduction to the topic of scattering by rough surfaces. Secondly, in Section 7.2 two recently proposed methods to include the effects of rough surface scattering into ray-based propagation prediction models are discussed. In Section 7.3 a new approach is proposed in which angular dispersion is determined directly at the receiving position using a stochastic effective roughness method. The model is described as a canonical model and simulation results are presented. Furthermore, the possibility of implementing the method into a ray-tracing model is discussed. In Section 7.4 the results of measurements that are used to calibrate the model and to compare with simulations are reported. The results show that the model is capable of including the effects of rough surface scattering and that accurate calibration can be performed using high-resolution measurements. Finally, conclusions are drawn in Section 7.5.

7.1   Scattering from rough surfaces

When a plane wave is incident on a smooth surface, a secondary field is generated that may be regarded as resulting from secondary sources across the surface (Huygen's principle) [99]. Each of these sources has its own phase, ψ, which is determined from the position on the surface, as shown in Fig. 7.1. In the specular direction, the waves generated by the sources constructively interfere, because their resulting phase differences $\Delta\psi = 0$. Away from this direction, destructive interference will lead to cancellation of the scattered fields. An infinite flat surface will reflect in the specular direction only, whereas a flat surface of finite extent scatters in and around the specular direction (beam broadening or angular dispersion), in a manner that depends on the dimensions of the surface with respect to the wavelength of the impinging waves. The scattered field from such a finite surface is fully coherent, e.g. the average received field, determined as a time average over a changing surface, is non-zero. This is because the phases of the secondary sources are preserved and will always constructively interfere in specific directions.

If a rough surface is considered, conditions of constructive interference in the specular direction and destructive interference in all other directions will not always be maintained, because $\Delta\psi$ also depends on the height difference, Δh. As a result, energy is also scattered in other directions than the specular direction. The Rayleigh criterion states that if $\Delta\psi < \pi/2$ in the specular direction, the surface is considered smooth. To simplify further analysis, consider a *statistically* rough surface with a random height distribution. An incident wave on such a surface will cause the average reflected field in the specular direction to be reduced. This reduction occurs, because not all secondary sources will always constructively interfere in this direction, $\Delta\psi \neq 0$. This average is determined as an ensemble average over many surfaces with the same statistics, or a time average over a changing surface [100]. Energy is also scattered in other directions, where destructive interference is not maintained.
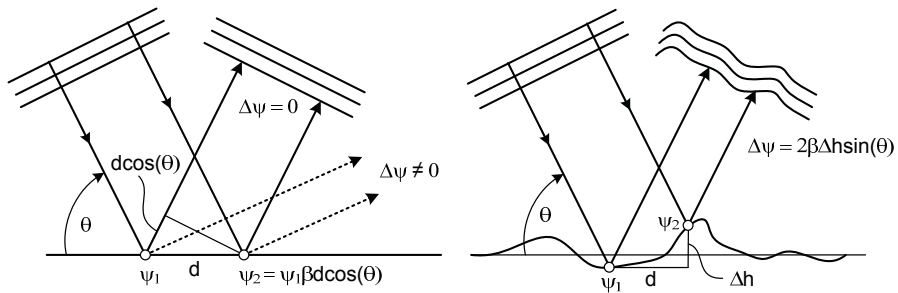
Fig. 7.1: Phase differences between reflected waves from a flat (left) and rough surface (right).

If the phases of the secondary sources are assumed to be randomly and uniformly distributed ($0 < \psi \leq 2\pi$), the specular field disappears completely and the resulting field is therefore called the incoherent or diffuse field. One should note that if the phases are randomly but not uniformly distributed the field has both a coherent and an incoherent part [101]. This last situation is more likely in real scenarios, since the surface irregularities of man-made structures are generally not fully random. In Fig. 7.2 the effects of scattering from different surfaces are shown schematically.

Similar scattering effects are also observed when a surface is non-homogeneous, and composed of different materials, with various different dielectric and conducting properties. The amplitudes and phases of the individual Huygen's sources of such a surface are distorted. A surface that is seemingly smooth, but is composed of different materials may, therefore, still cause scattering that suffers from angular dispersion. In real-world scenarios, building surfaces likely consist of *both* surface height fluctuations and irregular material properties.

In Chapter 5 the effects of angular dispersion by rough surfaces are illustrated from measurements. In Chapter 6 the angular dispersion of the specularly reflected field by specific buildings and other objects are identified and the results showed angular spread values of several degrees. The next section discusses the modelling of these effects for inclusion in ray-based propagation models.

7.2 Existing methods

A large number of methods have been proposed in literature to solve the problem of scattering by a rough surface [100–102]. Each of the methods has its own complexity and domain of validity. For deterministic ray-based prediction models the modelling of rough surface properties in a deterministic manner can become highly complex due to the large number of interactions that need to be considered. Therefore, the effects of rough surfaces can only be included if low complexity (statistical) models are used. For this reason, geometrical optics (GO) approximations or modified reflection

(a)

(b)

(c)

(d)

Fig. 7.2: Reflected and scattered fields from (a) an infinite flat surface, (b) a finite sized flat surface, (c) a very rough infinite surface and (d) an infinite surface with either a slight roughness consisting of a single material, or a flat surface composed of different materials or both.

and scattering coefficients are sometimes used. Because modelling both the physical roughness and the changes in the internal structure in ray-based propagati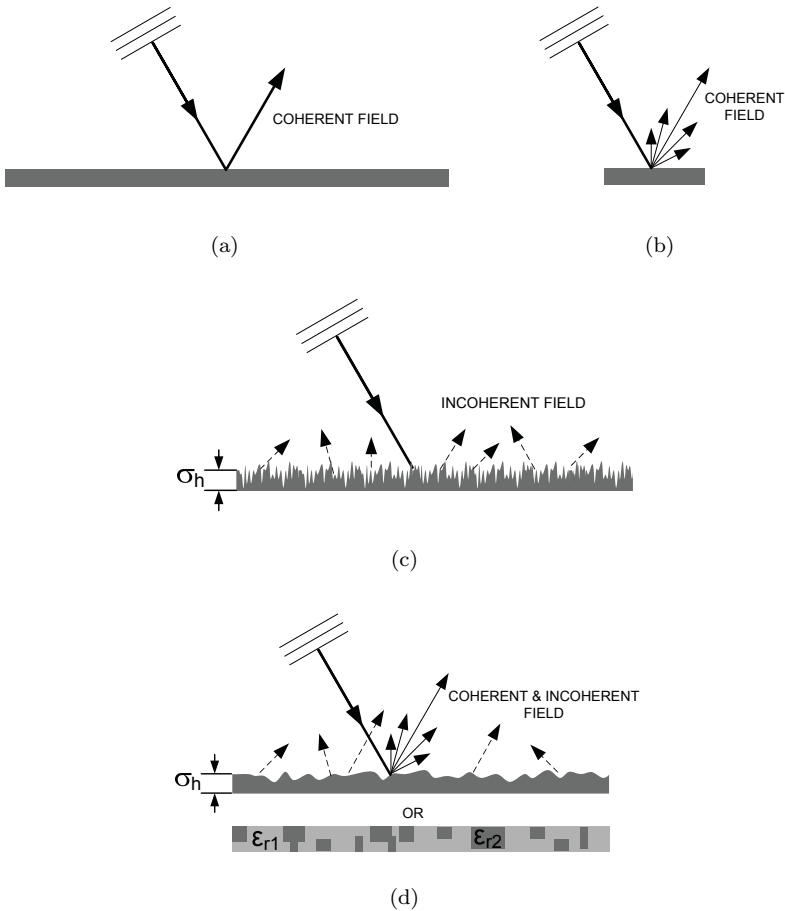on models is highly complex, it has been proposed to model the combined effects (roughness and building material properties) in an *effective* height distribution for a statistically rough surface. In the next two sections, two important methods are discussed that, to a certain extent, allow models to account for the effects of statistically rough surfaces in ray-based prediction procedures. The second method is discussed in more detail, because it is used in the new approach in Section 7.3.

7.2.1 Rough surface as an effective roughness

In [16, 96–98] a method has been described that is based on associating an effective roughness to each building wall. The method is based on dividing the surface into infinitesimal surface elements. For each of these surface elements the scattering pattern can be considered to be a Lambertian pattern, i.e., a non-uniform spherical wave with amplitude $E_s = E_{s0}\sqrt{\cos(\phi_s)}$. Here, ϕ_s represents the direction of the scattered field measured perpendicular to the surface. Furthermore, a scattering coefficient $S = E_s/E_{inc}$ and a reflection loss factor R, that accounts for the loss of power in the specular direction, is associated with each wall and $R \cong \sqrt{1 - S^2}$. A value of $S = 0.4$ was determined to be a realistic value for field predictions in suburban areas [98]. Measurement-based tuning can be performed by changing the value for S. The scattered field is assumed to be completely incoherent or diffuse. If the scattering surface is far from the observation point, ϕ_s is almost the same for all surface elements, which means that instead of only an infinitesimal surface, the entire wall now creates a Lambertian scattering pattern. The effective roughness method is implemented in a ray-tracing model (imaging method), as shown in Fig. 7.3 (a). Besides reflection and diffraction, scattering is also considered as a method of interaction. The field of a ray that experiences scattering decays with the product of the distances between transmitter-scatterer and scatterer-receiver and is therefore only considered if it occurs *at the end of an interaction sequence*. Because diffuse scattering is considered incoherent, a uniformly distributed random phase is attributed to each ray that experiences a diffuse scattering interaction. By using a visibility algorithm the scattering objects are found and scattered rays are supposed to spring from the barycentre of the wall, if far walls are considered. The delay information is obtained via ray information.

In addition to the non-directive Lambertian pattern, a more directive pattern, with and without backscattering, has also been proposed that assumes that the scattering lobe is steered towards the direction of the specular reflection. This assumption is not fully consistent with the previous assumption of incoherent scattering, but measurements show that this model is better than the non-directive model, which implies that the scattering cannot be considered fully diffuse.

In [103], a similar approach based on the above method is proposed and implemented in a ray-launching tool. As shown in Fig. 7.3 (b), the surface of a (close) wall is subdivided into surface elements dS. When a ray impinges upon a surface element,
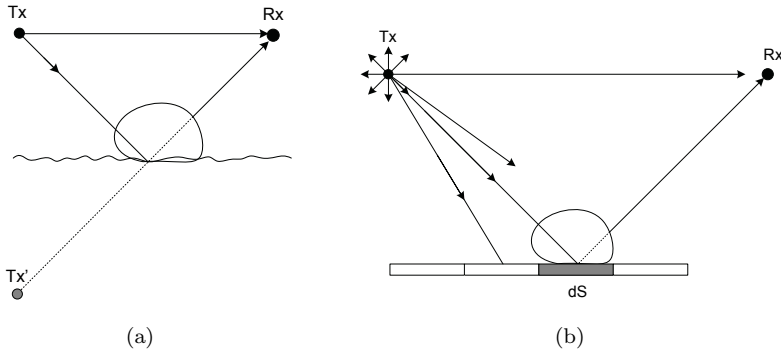
Fig. 7.3: The Lambertian scattering approach (a), using ray-tracing and (b), using ray-launching.

a new ray is generated that reaches Rx with an amplitude according to the surface scatter pattern. It is shown here that this has an important impact on the delay profile. The number of subdivisions into which the wall is subdivided is determined by the distance of the transmitter and the receiver from the wall and the resolution of the ray-launching procedure.

7.2.2   Rough surface as a random array of elements

Several theories and methods exist that are based on modelling the effect of a statistically rough surface as a random array of elements (e.g. facets), the individual scattering characteristics of which, are known. The distribution of the elements then determines the overal scattering effect of the surface in the delay and angular domain.

A statistically rough surface can be described by the standard deviation of the surface height σ_h and the correlation length, L_c, of the irregularities, the latter being a measure for the statistical dependence of the heights at two points on the surface. Assume a Gaussian surface, i.e. the surface height is normally distributed with zero mean and standard deviation σ_h, as shown in Fig. 7.4 (a). The distribution for the heights is then given by

$$\mathbb{P}_h(h) = \frac{1}{\sqrt{2\pi}\sigma_h} \exp\left\{ -\frac{1}{2}\left(\frac{h}{\sigma_h}\right)^2 \right\}. \tag{7.1}$$

The autocorrelation coefficient $\rho_{hh'}(\ell)$ defines the correlation between two heights h, h' separated by a distance ℓ. From the Gaussian surface assumption $\rho_{hh'}(\ell)$ is Gaussian and defined as

$$\rho_{hh'}(\ell) = \exp\left\{ -\left(\frac{\ell}{L_c}\right)^2 \right\}. \tag{7.2}$$

(a)

(b)
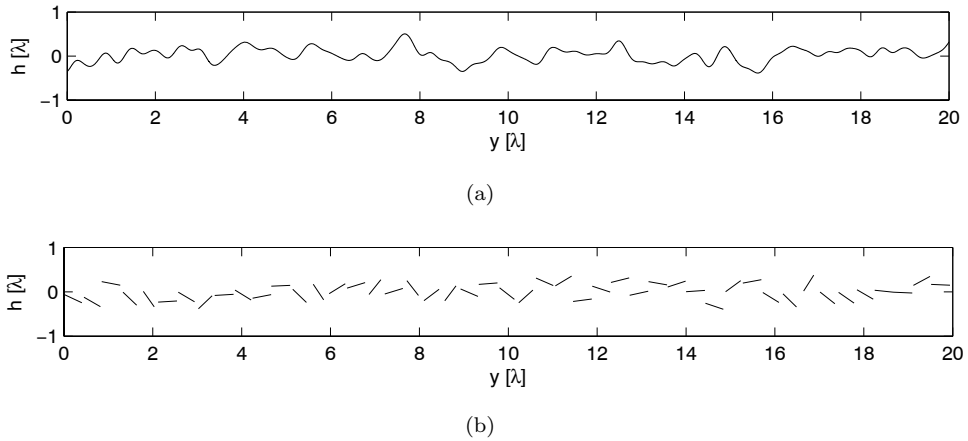
Fig. 7.4: Example of (a), a Gaussian rough surface with $\sigma_h = \lambda$ and $L_c = 0.3\lambda$ and (b), random planes with an orientation and an independent height that correspond to the same statistical properties as the Gaussian rough surface.

With the application of ray-launching, the above statistical description of the rough surface was used in [19]. There, a method is presented that is based on a tangential-plane approximation, which means that the curvature and, therefore, the correlation length of the surface is assumed to be large compared to the wavelength. The total field at any point on the surface can be determined as if the wave were impinging in the tangential plane, at that point on the surface. The different orientations of the tangential planes (slopes) and the varying heights at the point of reflection then determine the scattering in directions other than the specular direction.

The slopes s of the rough surface are defined as

$$s = \tan \vartheta = \frac{dh}{dy}, \tag{7.3}$$

and, according to the Gaussian surface assumption, are normally distributed with variance [101]

$$\sigma_s^2 = -\sigma_h^2 \cdot \rho_{hh'}^{''}(0) = \frac{2\sigma_h^2}{L_c^2}. \tag{7.4}$$

Hence, the distribution of s equals

$$\mathbb{P}_s(s) = \frac{1}{\sqrt{2\pi}\sigma_s} \exp\left\{ -\frac{1}{2} \left(\frac{s}{\sigma_s} \right)^2 \right\}. \tag{7.5}$$

Using Eq.(7.4) and the fact that the variance is given by

$$\sigma_s^2 = \mathbb{E}\left\{ (s - \mathbb{E}\{s\})^2 \right\} = \mathbb{E}\{s^2\} - \mathbb{E}\{s\}^2 = \mathbb{E}\{s^2\} - 0, \tag{7.6}$$

allows writing the RMS gradient of a 2-D surface with $h = h(x, y)$ as

$$\sigma_{s_{xy}} = \sqrt{\mathbb{E}\{s_x^2 + s_y^2\}} = \sqrt{\mathbb{E}\{s_x^2\} + \mathbb{E}\{s_y^2\}} = \frac{2\sigma_h}{L_c} =$$
$$\sqrt{\mathbb{E}\left\{\left(\frac{\sqrt{2}dh_x}{L_c}\right)^2 + \left(\frac{\sqrt{2}dh_y}{L_c}\right)^2\right\}} = \sqrt{\mathbb{E}\left\{\frac{dh_x^2}{dx^2} + \frac{h_y^2}{dy^2}\right\}}, \quad (7.7)$$

where the first moment of a 2-D chi-square distribution is used to write the variance of the height distribution as

$$\sigma_h^2 = \frac{\mathbb{E}\{dh_x^2 + dh_y^2\}}{2}. \tag{7.8}$$

The RMS gradient of the 2-D surface defined in Eq. (7.7) can be interpreted as a plane of dimensions $\frac{2L_c}{\sqrt{2}} \times \frac{2L_c}{\sqrt{2}}$ having a random orientation with the same statistical properties as the Gaussian rough surface. Thus, a normally distributed surface described by surface height σ_h and correlation length L_c can also be described by planes of size $\frac{2L_c}{\sqrt{2}}$ with a random slope described by Eq. (7.5) and a random height with a normal distribution. It was shown in [19] that the scattered field from such a surface can be approximated by performing a ray-launching procedure as follows.

Assume that N parallel rays (locally plane wave assumption) impinge upon a surface that is considered rough. Each ray is reflected according to the stochastic orientation of the local tangential plane, a Gaussian height variation and Fresnel reflection coefficients. At the observation point arriving rays are collected and, since the ray density is proportional to the power density, the electric field is weighted according to the square root of the ray density. The method is depicted in Fig. 7.5 (a). To produce the scattering pattern, the procedure of generating planes, shooting rays and collecting them at the receive point is repeated M times for averaging. The temporal average electric field (a measure for the coherent field) and the power sum of the temporal varying electric field (a measure for the incoherent field) for a time changing surface can be determined. Although the method is based on facets of size $\frac{2L_c}{\sqrt{2}} \times \frac{2L_c}{\sqrt{2}}$, in the examples the facets are much smaller, i.e. $\frac{2L_c}{81}$ or $\lambda/10$ [19]. Due to this small size, the validity of ray-based analysis is questionable.

The method presented in [20,94,95], depicted in Fig. 7.5 (b), is also based on describing the rough surface by a height distribution and correlation length and transforming this to slopes of tilted planes that describe the same statistical properties. The surfaces are, however, not subdivided into facets and no local plane wave assumption is used. The method is used in a ray-launching concept and proceeds by launching rays into the environment of interest, and when they impinge upon a rough surface, reflecting them in a random direction according to the statistical properties of the surface (the slopes). If a line of sight exists between the point where the wave impinges and the observation point, a second ray is launched to the observation point with a magnitude weighted by the probability of having a well-directed plane (path-tracing).
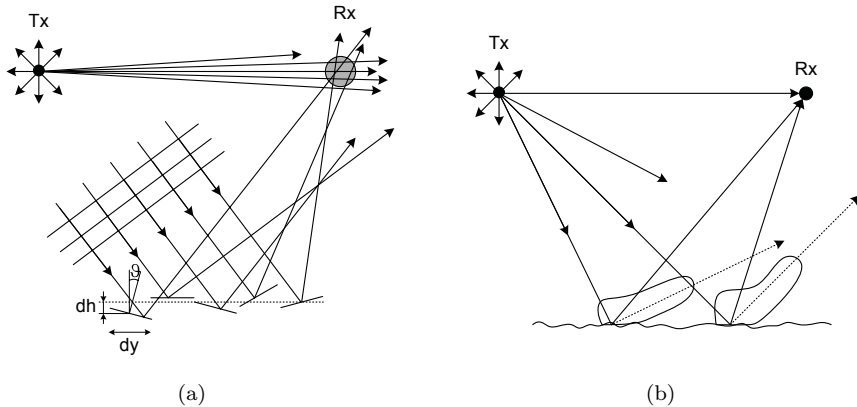
Fig. 7.5: The stochastic scattering approach (a), from reflections at randomly oriented tangential planes and (b), using probability distributions and path-tracing.

This process is repeated a fixed number of times. To determine the angular scattering pattern, a coherent sum is made of all contributions in a small solid angle $d\phi$, taking into account their individual phases, which are influenced by the height distribution of the surface and the propagation path.

In both of the above methods, the angular distribution of the scattered waves is independent of frequency and the stochastic height variation is determined independently of the slopes, which is an approximate. This is visualised in Fig. 7.4 (b) where local tangential planes with the same statistical properties for the slopes and for the heights as in Fig. 7.4 (a) are shown. It is, however, shown in [20, 94, 95] that this approximation remains in good agreement with the deterministic approach. Although both are approximation methods, comparisons with the Kirchhoff models with scalar approximation and stationary phase approximation in [19] show good qualitative and quantitative agreement.

7.3 An approach to modelling angular dispersion at the receiver

The methods discussed in the previous sections both model the scattering caused by surface roughness as a sort of effective roughness. The method in Section 7.2.1 is used in both ray-launching and ray-tracing. It assumes the diffuse scattering to be fully incoherent and directive, which is somewhat inconsistent. It can be calibrated by changing the relation between S and R, but this calibration is less accurate in the angular domain.

The method in Section 7.2.2 is applicable to ray-launching. Rays are launched from

the transmitter and are reflected from a rough surface in different directions by tangential planes according to statistical surface parameters. Both the coherently and the incoherently scattered components are included. Calibration in the angular domain can be done by changing the surface roughness parameters. Because the method generates a large number of rays based on ray-launching and Monte-carlo type simulations, it becomes computationally complex.

Although computationally more complex, the method in Section 7.2.2 is interesting because it includes both the incoherent and coherent components and allows for accurate calibration in the angular domain. The method in Section 7.2.1 has some limitations, but is also attractive because it is applicable to ray-tracing (image method) type models, which helps to reduce complexity.

In order to find a way to model the effects of surface scattering in a ray-tracing model more accurately and to allow for better calibration, the model in Section 7.2.2 was used, during the work for this thesis project, as a starting point. The scattering effects are included in a similar stochastic manner, but the angular dispersion is modelled directly at the receiver position instead of determining it via the reflective surface. The scattering caused by surfaces is modelled as resulting from an effective surface roughness, which means that the scattering caused by the real physical properties (height fluctuations and material properties) of the surfaces are modelled via a rough surface with properties that reflect the same scattering behaviour as the real surface. Summarising, the proposed approach involves the following assumptions.

- Real-world scattering, which is dependent upon many variables, can be approximated as being dependent upon only one effective surface roughness.

- The curvature of the effective surface is large compared to the wavelength.

- Waves are incident upon randomly oriented planes that are oriented tangentially to surface segments with random slopes and orientations.

- The height of planes is determined from σ_h, *independently* of the slopes s.

- The infinite plane and high frequency approximations are valid.

- There is no shadowing or multiple scattering.

- Both incoherent and coherent energy is scattered.

In the next section a canonical problem is used to describe the method.

7.3.1   Canonical problem

Consider the scenario in Fig. 7.6. A surface is illuminated by a spherical wave that originates from the Tx. It is assumed that there is no line of sight between the Tx and the Rx, and that each ray has only a single interaction with the surface on its path between the Tx and the Rx. This simplified model uses only a single interaction and is therefore considered as the canonical problem. If the surface is smooth, the reflection
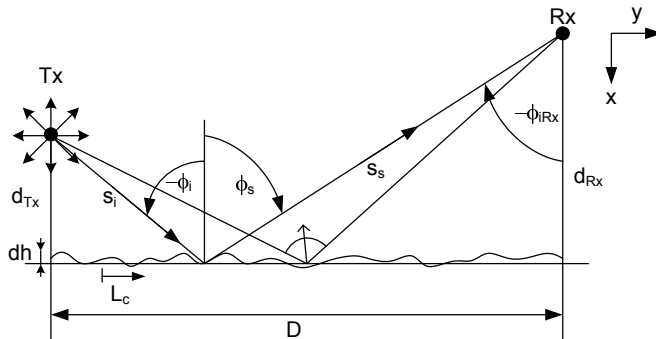
Fig. 7.6: Scenario of transmitter (Tx), receiver (Rx) and a rough surface which causes different rays to arrive at the receiver from different directions.

can be modelled as a single ray that is reflected towards the Rx at the surface with the aid of geometric optics (GO). The field incident at Rx can be determined as

$$E_{iRx} = E_0 A(s_i + s_s) R(\phi_i, \phi_s) e^{-jk(s_i + s_s)}, \qquad (7.9)$$

where E_0 is the field at a reference distance from Tx, $R(\phi_i, \phi_s)$ represents the Fresnel reflection coefficient, $e^{-jk(s_i+s_s)}$ represents the total phase shift due to the free-space propagation before and after the interaction with the surface and $A(s_i, s_s)$ represents the divergence factor corresponding to the total path length travelled by any ray between the Tx and the Rx.

Instead of a single specularly reflected ray, multiple reflected rays may arrive at the receiver when the surface has a physical roughness and when it is composed of different materials. Both effects can be accounted for simultaneously through the consideration of an effective surface roughness that results in scattering characteristics that are similar to those of the real-world surface. To determine the scattering effect, incident rays are reflected at the surface according to the stochastic orientation of a local tangential plane and a height variation. Although it is possible to determine the number of arriving rays and their direction from Monte-Carlo simulations, this is computationally inefficient. Instead, it is considered better to determine the probability of arriving rays directly at the receiver.

If a Gaussian rough surface is considered, as described in Section 7.2.2, the distribution of surface element slopes, given by Eq. (7.5) on page 117, can be used to describe the distribution for the reflected direction of departure from the surface, ϕ_s as [95]

$$\mathbb{P}_{\phi_s}(\phi_s) = \frac{L_c}{4\sigma_h \sqrt{\pi} \cos^2\left(\frac{\phi_i + \phi_s}{2}\right)} \exp\left\{ - \left(\frac{L_c \tan\left(\frac{\phi_i + \phi_s}{2}\right)}{2\sigma_h} \right)^2 \right\}. \qquad (7.10)$$

This distribution is valid when a plane wave is incident from direction ϕ_i.

In the scenario depicted in Fig. 7.6, the angle ϕ_{iRx} from which each ray arrives at the Rx is uniquely related to an angle ϕ_i, with which the same wave is incident on the surface. The relationship between ϕ_i and ϕ_s can be written as:

$$\phi_i = -\tan^{-1}\left(\frac{D - d_{rx}\tan(\phi_s)}{d_{tx}}\right).\tag{7.11}$$

As a result, the distribution of the incoming scattered waves at the receiver can be determined in closed form using Eq. (7.10) and $\phi_{iRx} = -\phi_s$ as

$$\mathbb{P}_{\phi_{iRx}}(\phi_{Rx}) = \exp\left\{-\left(\frac{L_c \tan\left(\frac{\phi_i - \phi_{iRx}}{2}\right)}{2\sigma_h}\right)^2\right\}\cdot$$

$$\frac{L_c\left\{1 + \tan^2\left(\frac{\phi_i - \phi_{iRx}}{2}\right)\right\}\left\{d_{Rx}(1 + \tan^2(-\phi_{iRx})) + d_{Tx}(1 + \tan^2(\phi_i))\right\}}{4\sigma_h\sqrt{\pi}\,d_{Tx}(1 + \tan^2(\phi_i))},\tag{7.12}$$

where the relationships

$$\mathbb{P}_a(a)|da| = \mathbb{P}_b(b)|db|,\tag{7.13}$$

[19, 104], and

$$\frac{d}{d\phi_{iRx}}\tan\left(\frac{\phi_i - \phi_{iRx}}{2}\right) =$$

$$\frac{\left\{1 + \tan^2\left(\frac{\phi_i - \phi_{iRx}}{2}\right)\right\}\left\{d_{Rx}(1 + \tan^2(-\phi_{iRx})) + d_{Tx}(1 + \tan^2(\phi_i))\right\}}{2d_{Tx}(1 + \tan^2(\phi_i))},\tag{7.14}$$

have been used to re-write Eq. (7.10) in terms of ϕ_{iRx}, rather than ϕ_s.

Now that the probability distribution function for the direction of incoming waves is known at the receiver, the scattering behavior of a rough surface can be determined directly at the receiver. Since the power density of an incoming wave in a small solid angle $d\phi$ around direction ϕ_{iRx} is proportional to the probability, the electric field is weighted by the square-root of the probability. An independent random phase shift, related to the height distribution, can also be added to the electric field through multiplication by $e^{-j\psi_i}$. The electric field in terms of ϕ_{iRx} can then be written as:

$$E_{iRx}(\phi_{iRx}) = E_0 A(s_i, s_s)e^{-jk(s_i+s_s)}R(\phi_i, \phi_{iRx})\sqrt{\mathbb{P}(\phi_{iRx})}e^{-j\psi_i}.\tag{7.15}$$

Here, ψ_i is determined from

$$\psi_i = \frac{-2\pi h}{\lambda\left(\cos\phi_i + \cos\phi_{iRx}\right)}.\tag{7.16}$$

The results for the coherent and incoherent part of the received power, relative to that of a specular reflection, are determined from a large number of realisations, in which

the phase shift caused by the random height fluctuations is changed in accordance with the change in path lengths brought about by the surface irregularities.

Using the new approach, the angular dispersive effects of rough surface scattering can be included directly at the receiver, which otherwise would require many more complex Monte-Carlo simulations. Instead of only the specular component, a stochastic contribution is added according to the surface parameters, which includes both the coherent and incoherent scattered energy.

7.3.2   Simulation results

The results of the reflected power in four scenarios with different Rx and Tx setups and surface roughness parameters are presented in Figs. 7.7 and 7.8. At the receiver the total, coherent and incoherent power scattered by the surface is determined. The resulting angular spread, σ_ϕ, for the total received power is also shown. The results are obtained from 1000 realisations with quantisation $d\phi = 1°$. The properties of the surfaces represent a moderately rough surface, for which $\sigma_h = 0.1$, and in which case the incoherent component is dominant and a smoother surface, for $\sigma_h = 0.05$, and in which case the coherent component is dominant. The well known scalar reflection reduction factor for Gaussian rough surfaces [101], defined as

$$R_r = e^{-2(k\sigma_h \cos \phi)^2},\qquad(7.17)$$

is also plotted for comparison. The validity of R_r assumes $L_c \to 0$ and is limited up to approximately four times the Rayleigh criterion, which means $\sigma_h < 0.125\lambda$. Note that the absolute value of R_r depends on $d\phi$ and is not important here.

The results show that the coherent component is indeed dominant in the case of the smoother surface ($\sigma_h = 0.05$) and the incoherent component in the case of the rougher surface ($\sigma_h = 0.1$). It is also observed that doubling the surface roughness ($\sigma_h \to 2\sigma_h$) causes approximately a double angular spread ($\sigma_\phi \to 2\sigma_\phi$). The effect on σ_ϕ due to the position of the Tx, with respect to the surface, is also observed. In this scenario, moving the Tx closer to the surface increases σ_ϕ, which is mainly caused by the difference in the specular reflection direction. In all scenarios a similar behaviour of R_r, the reduction of the specular component, is observed. Instead of giving a reduction for the specular component, the proposed approach produces both coherent and incoherent components in the scattered field and accounts for the divergence of the power in the angular domain.

The results presented above are determined for a 1-D surface. For a 2-D surface the roughness can be described by the slopes of the surface in two orthogonal directions $\overrightarrow{x}$ and $\overrightarrow{y}$. If the variables are assumed to be independent, the joint probability can be used as

$$\mathbb{P}(\theta_{iRx}, \phi_{iRx}) = \mathbb{P}(\theta_{iRx})\mathbb{P}(\phi_{iRx})\qquad(7.18)$$

where $\mathbb{P}(\theta_{iRx})$ and $\mathbb{P}(\phi_{iRx})$ correspond to surface fluctuations in perpendicular direc-
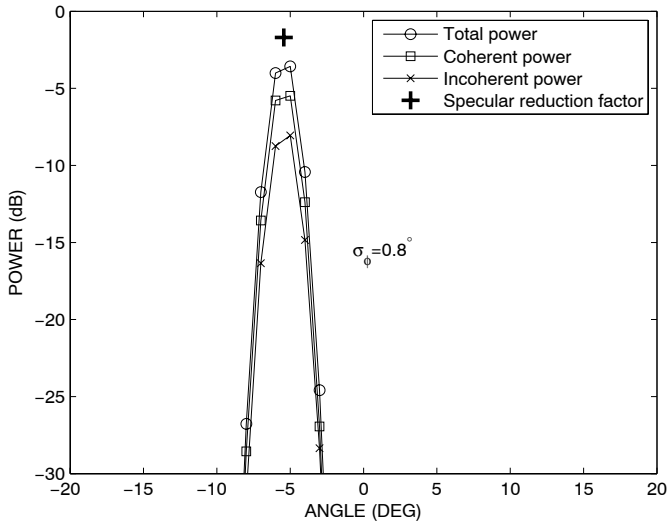
(a)
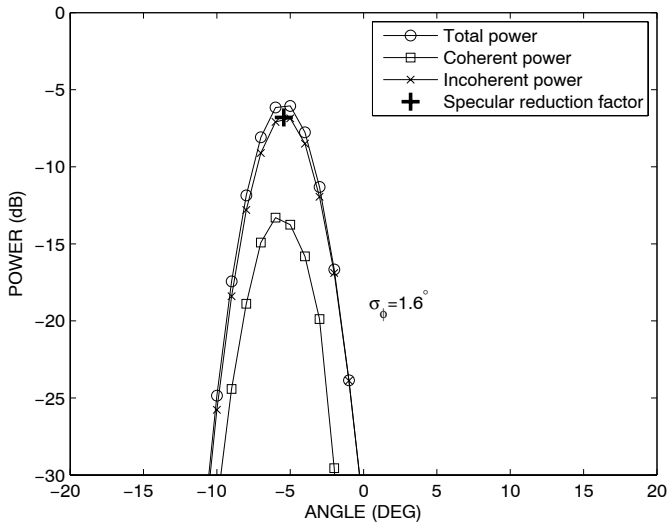
(b)

Fig. 7.7: Simulation results of received power versus the angle of incidence at the receiver using the scenario presented in Fig. 7.6 and the following parameters expressed in terms of λ: $dTx = 10, dRx = 5, D = 10, L_c = 10$. In (a), $\sigma_h = 0.05$ and in (b) $\sigma_h = 0.1$. The angular spread for the total power is represented by σ_ϕ.
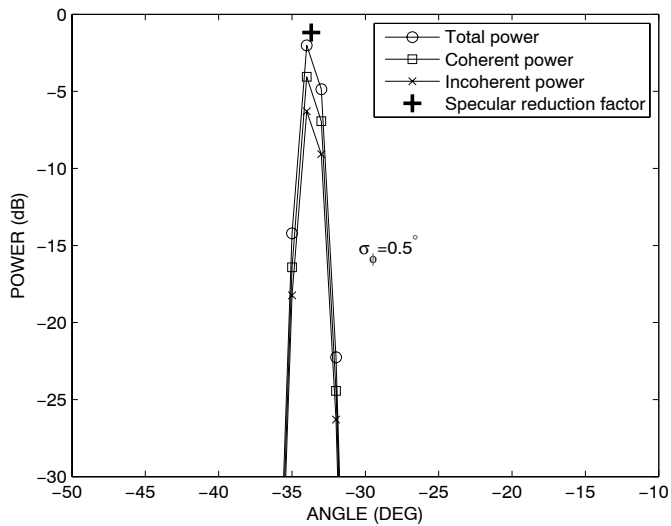
(a)
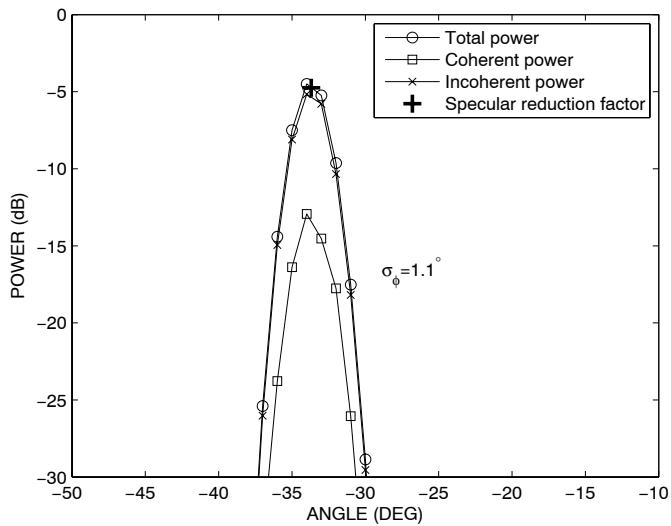
(b)

Fig. 7.8: Simulation results of received power versus the angle of incidence at the receiver using the scenario presented in Fig. 7.6 and the following parameters expressed in terms of λ: $dTx = 100, dRx = 5, D = 10, L_c = 10$. In (a), $\sigma_h = 0.05$ and in (b) $\sigma_h = 0.1$. The angular spread for the total power is represented by σ_ϕ.
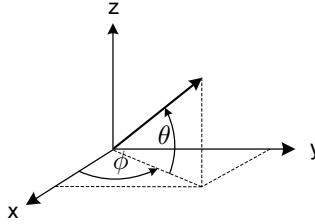
Fig. 7.9: Definition of angles ϕ and θ for the receiver.

tions and where θ_i is determined from

$$\theta_i = -\tan^{-1}\left\{\frac{\frac{-dTx\tan(\theta_{iRx})}{\sin(\phi_{iRx})} + hTx - hRx}{\sqrt{(\frac{dTx}{\tan(\theta_{iRx})} + D)^2 + (dRx - 2dTx)^2}}\right\}. \tag{7.19}$$

Here, hTx and hRx correspond to the transmitter and receiver heights in the z direction, respectively, and the angles from the receiver perspective are defined according to figure 7.9.

Because the Gaussian surface assumption may not reflect the real scattering properties of the surface in both angle and delay for the same parameters, the slopes and the heights can also be characterised directly and independently. This means that the distribution for the slopes and the heights may be chosen differently and different distributions for the slopes and the height distributions may be used.

7.3.3   Incorporation of results into a ray-tracing model

In order to apply the model described in Section 7.3.1 into a ray-tracing type of model additional assumptions are required. The canonical model includes the effects of a single interaction with a rough surface, and cannot account for all dispersive effects of multiple interactions that occur along the path between transmitter and receiver. A possible way to integrate the method in a ray-tracer, however, is to account for the scattering effects in the angular domain only at the last interaction of each arriving ray, initially determined by the ray-tracing procedure. For all the other interactions only a scattering reduction factor for the specular direction is taken into account. Here it is assumed that diffuse fields decay with the product of the distance between the transmitter and the scatterer and that between the scatterer and the receiver, similar as in [16], therefore only the last interaction is considered important. As a result, the ray-tracing procedure is used op to the last interaction, as shown in Fig. 7.10 and is followed by the procedure in Section 7.3.1, where different realisations are generated. This is done for all arriving rays obtained from the ray-tracing procedure and as such the combined scattering effects of the surfaces seen by the receiver is taken into account.
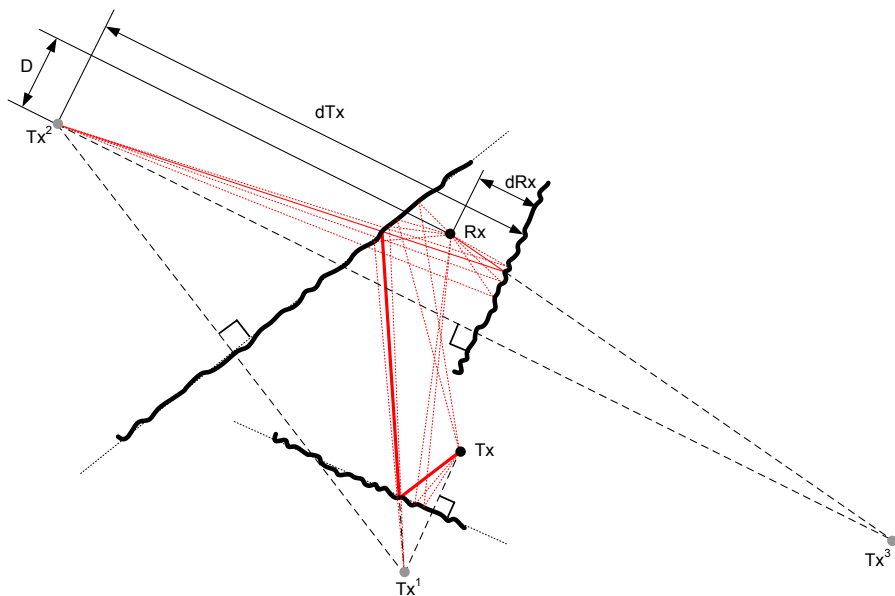
Fig. 7.10: Scenario of transmitter, receiver, multiple reflections and dispersion caused by rough surfaces. To include the effects of rough surfaces, ray-tracing is used up to the last interaction. Then the approach in Section 7.3.1 is applied to determine the different rays and their arriving directions at the receiver.

It should be mentioned that the method presented here is based on a SIMO approach. Although a similar procedure can be used to determine the angular dispersion of the departing rays at the transmitter location, there is no unique relation between the transmitting and receiving rays and the power balance is not maintained. Additional effort is required in order to extend the current model towards a full double-directional (MIMO) channel representation. Still, the effects of angular dispersion at the receiver are taken into account using the new model, which can give an approximation of the MIMO performance [105].

Furthermore, the method initially assumes infinite surfaces. If the sizes of the surfaces become smaller and surface irregularities increase this becomes more important. For implementation in a ray-tracer the finiteness of the surfaces needs to be taken into account using a visibility algorithm, in which rays that depart from outside the surface with limited dimensions are discarded.

In order to calibrate the model in Section 7.3.1 in terms of effective surfaces roughness, high-resolution channel data can be used. If measurements are performed at a known distance from the surface, the angular spread values can be used to calibrate the statistical properties of the surface. The next section describes the calibration and verification in more detail.

7.4 Calibration and verification by measurements

With the aid of the model presented in Section 7.3.1, it is possible to include angular dispersive effects directly at the receiver in ray tracing based propagation prediction models. Because the model is based on assuming an effective roughness for each surface, characterisation and calibration by measurements is necessary. In order to calibrate the model in terms of effective surfaces roughness, high resolution channel data can be used. If measurements are performed at a known distance from the surface, the angular spread and power can be used to calibrate the statistical properties of the surface.

The measurement system and methods presented in the previous chapters allow to characterise and isolate the scattering effects of specific building faces with high resolution. In order to perform a first characterisation and calibration, this section presents the results of measurements that were performed on a large building face at the campus area of the Technische Universiteit Eindhoven (TU/e) in Eindhoven, the Netherlands. The results were used to calibrate the model and to compare with the simulation results.

7.4.1 Measurement setup

The measurement scenario is presented in Fig. 7.11. The transmitter position is marked by Tx. The transmitting antenna consisted of an 8-dBi waveguide horn antenna with an azimuthal half-power-beam-width of 55° and was positioned at a height of 3.5 m. The main beam of the transmitting antenna was pointed southward, such that it illuminates building TR, shown in Fig. 7.12. Building TR is a four-storey high building of approximately 100 m long with a rough surface consisting mainly of windows and steel bars. Several scattered trees and cars are also located close to building TR. The reflections and scattering effects of building TR were characterised by moving the receiver over a trajectory of 116 m along side building TR, the beginning of which is marked by Rx1. Measurements were also performed over a trajectory of 60 m perpendicular to the long side of building TR, the beginning of which is marked by Rx2. The measurement trajectories are represented by dotted lines and the numbers along the trajectory correspond to the snapshot-set numbers. The receiving antenna, mounted on top of a vehicle at a height of 3.5 m, was moved at a nearly constant speed of about 12 and 9 km/h for the first and second trajectory, respectively.

For the first measurement trajectory 5990 and for the second 3990 snapshot sets of $K = 10$ snapshots are used for the AOA estimation, which means a channel estimate is available at least every 2 cm corresponding to 0.15 wavelengths.

7.4.2 Results

To isolate the scattering effects of building TR the MPC estimates from the measurements were clustered using the clustering algorithm presented in Chapter 6. The
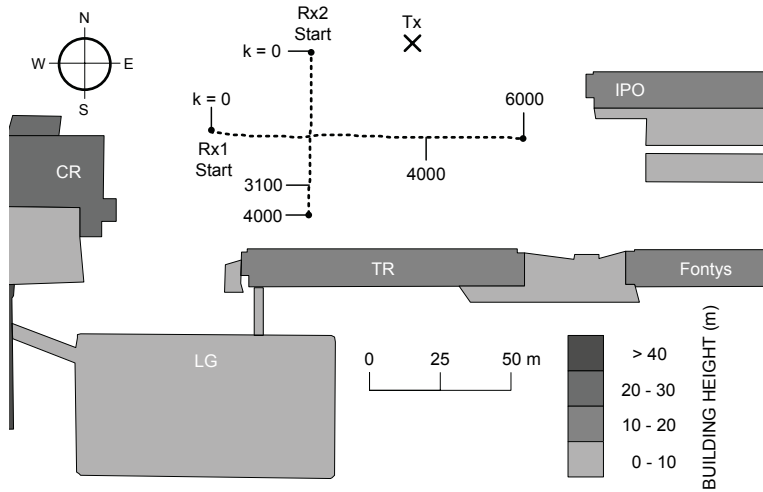
Fig. 7.11: Layout of the measurement site. The dotted line represents the GPS coordinates of the measurement trajectory. Along the trajectory values for k are plotted that correspond to the snapshot set numbers. Grey levels indicate the building heights in metres.

Fig. 7.12: Photo of the illuminated face of building TR.

azimuth angles along both trajectories of the MPC cluster corresponding to building TR are presented in Fig. 7.13. Here, the separate multipath contributions are summed with a resolution of $d\phi = 1°$ for a fair comparison with the simulation results. The effect of dispersion in the angular domain is clearly visible in both scenarios. The results of Rx1 show a stronger more specular component as well as a large band of MPCs, the centre of which changes along the trajectory. Apart from the first 25 m, the band of MPCs exists mainly on both sides around the specular component. Because the building is finite, during the first 25 m additional scattering effects only occur at the side of the specular component where the building is visible. The results of Rx2 also show a stronger more specular component and a band of MPCs that extends in the angular domain when the receiver moves towards building TR. Here, the effects of the finite building are also visible in that the band of MPCs exists mainly on one side of the specular component. For simplification, only the azimuth angles will be considered in this analysis.

7.4.3   Calibration

The results of ray-based propagation models are highly influenced by the electromagnetic properties of the materials of the reflective surfaces. In order to obtain valid results, the calibration of these models is necessary [15]. The material parameters, in terms of relative permittivity ϵ_r, can be determined from channel sounding measurements by relating the corresponding multipath contributions from the simulations to the measurements. The difference in power of the individual contributions can then be used to change the values for ϵ_r. When the roughness of surfaces is also considered, the surface roughness parameters need calibration as well. This can be done by using the results from accurate directional measurements and comparing values for the angular spread and the total cluster power in the simulations to the measurements at one or more points along the trajectory.

To calibrate the surface roughness from the measurements, the average intra-cluster angular spread is determined along a part of the trajectory of Rx1. This is done in order to average out the additional scattering and shadowing effects caused by other objects in the environment such as vegetation and cars. The angular spread is determined between $3000 \leq k \leq 4000$ for each k from a total of 50 snapshots $k - 25 < k < k + 25$. These 50 snapshots are taken along a trajectory of less than a metre, where the composition of the arriving waves is assumed to be stationary. The estimates from these 50 snapshots are used to determine the power-angular profile with $d\phi = 1°$, from which the actual angular spread is determined. The result of such an angular profile for $k = 4000$ is visualised in Fig. 7.14. The average angular spread is determined to be $< \sigma_\phi >= 9.9°$ and the averaged total power in the cluster is $< P_{tot} >= -27.9 \text{dBm}$. These parameters are used to calibrate the model such that it has the same angular spread and total power.

The roughness parameters of the model are set to generate the same angular spread as in the measurements. This is done by fixing $L_c = 10\lambda$ and tuning σ_h to $\sigma_h = 1.08\lambda$, which results in $\sigma_\phi = 9.9°$.
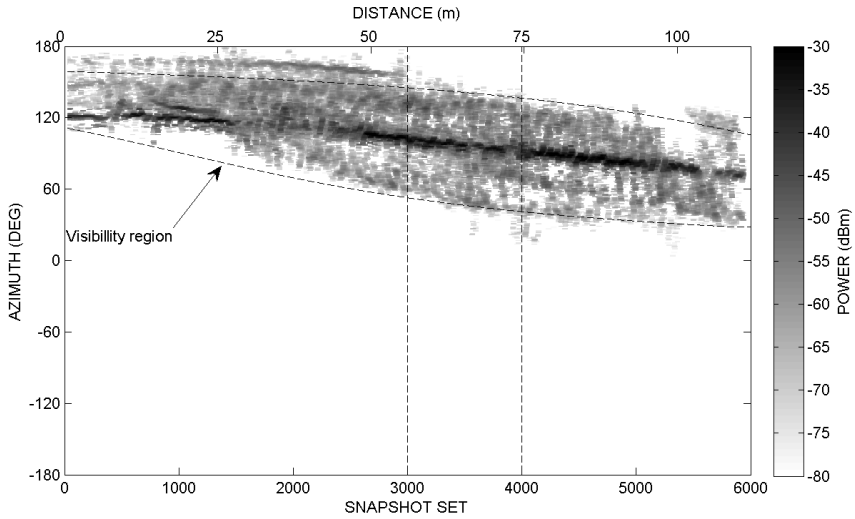
(a)
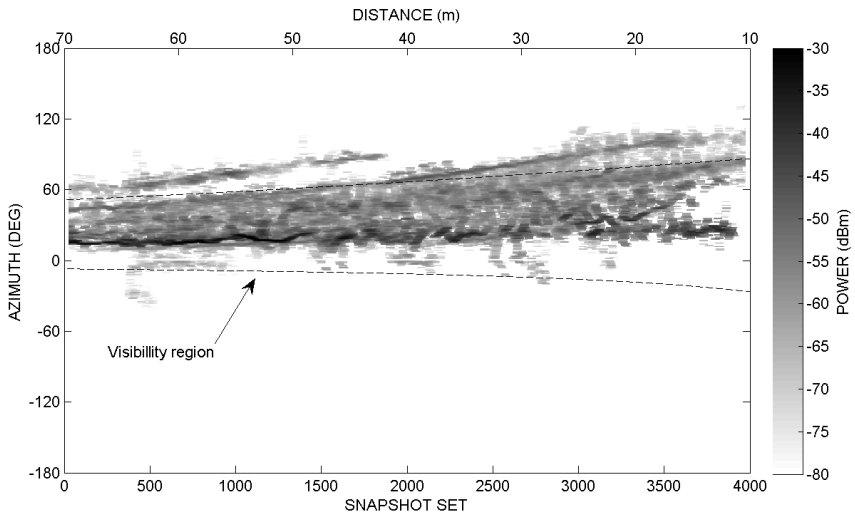
(b)

Fig. 7.13: Estimated azimuth angles from the measurements for the MPC cluster correspond-
ing to building TR for (a) receiver setup Rx1 and (b) receiver setup Rx2. The horizontal
black dotted lines represent the visibility regions obtained from the building geometry and
the measurement scenario.
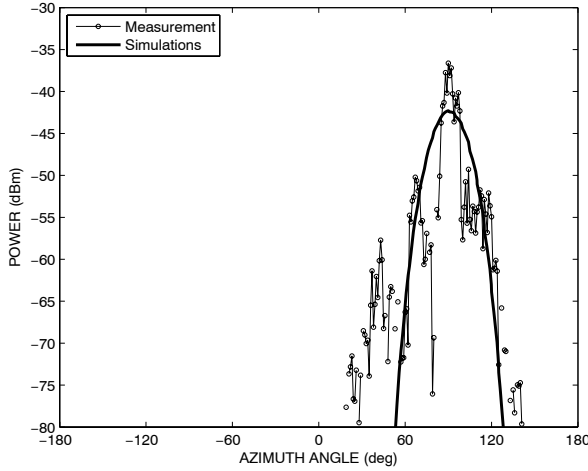
Fig. 7.14: Power-angular profile determined from the estimated AOAs for receiver setup Rx1 between $3975 < k < 4025$ and determined from calibrated simulations.

The Fresnell reflection coefficient for vertical polarisation R_v is to be calibrated such that the simulated total power of the cluster matches that of the measurements. The face of building Tr mainly consists of metal plating and structures, therefore R_v is expected to be close to one ($\epsilon_r \to -\mathrm{j}\infty$). The value for ϵ_r was set to $\epsilon_r = 1 - 10^6 j$, which results in $R_v = 1$. This value for ϵ_r corresponds to the reflection from a 3 cm thick metal wall at 1.8 GHz as reported in [91]. The resulting average power from the simulation is now close to that of the measurements and equal to $P = -28.2$ dBm.

The calibrated model is used to predict the total power-angular profile along both trajectories, shown in Fig. 7.15 (a) and (b). The total received power, almost equal to the power in the incoherent part, is shown here. The coherent part is more than 40dB below the incoherent part and is therefore not shown here. The result from a standard ray-based prediction tool is also plotted as a solid black curve in the same figure. Compared to the standard ray-based results the simulations based on the model in Section 7.3.1 now include dispersive effects caused by rough surfaces and calibrated by accurate measurements.

The results clearly show a similar dispersive behaviour compared to the measurements. Especially in Fig. 7.15 (b) an increase in angular spread is observed along the trajectory. The stronger and more specular component that is observed in some parts in the measurement results is not visible in the simulations, which is a direct result from the Gaussian surface assumption. To include these effects, the use of other, perhaps more suitable distributions could be considered. The amount of total received power and the direction of the highest received power are, however, in good agreement.

(a)
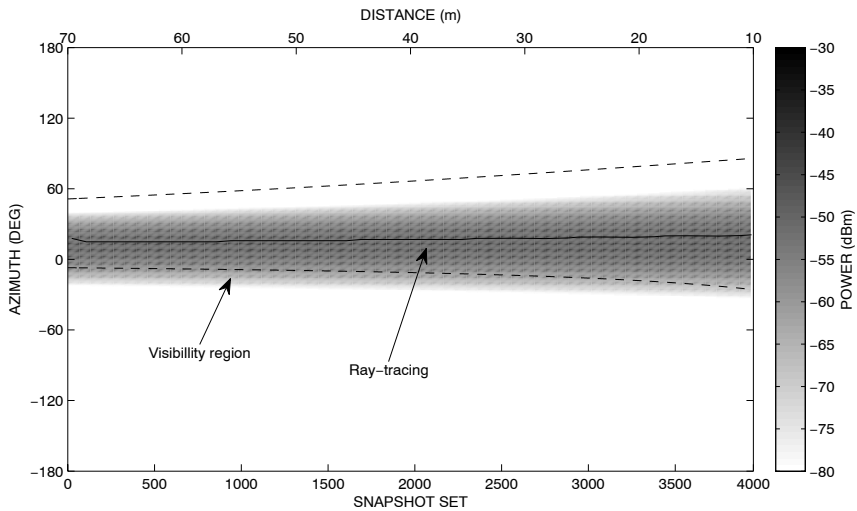
(b)

Fig. 7.15: Simulated azimuth angles corresponding to building TR for (a) receiver setup Rx1 and (b) receiver setup Rx2. The horizontal black dotted lines represent the visibility regions obtaine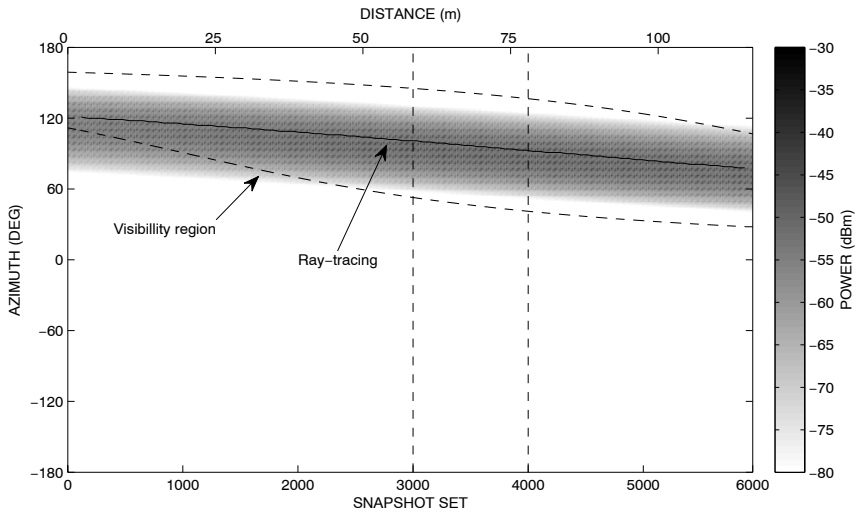d from the building geometry and the measurement scenario. The solid black lines represent results from a commercial ray-tracer.

The effects of the limited extent of the building are not included in the simulations. This effect is, however, observed in the measurements as a decrease in the angular spread if the receiver is at the beginning or moves towards the end of the building. This is most clearly shown at the begin of trajectory Rx1, where almost no scattered energy is received from the part of the building on the west side of the trajectory. This is illustrated with dotted lines (diffraction points) as visibility region, which corresponds to the actual building face that is visible to the receiver. In order to take the finite building effects into account a visibility algorithm is required.

The result of the measurements and simulations of receiver setup Rx1 at $k = 4000$ that are shown in Fig. 7.14, show that a stronger more specular component is observed in the measurements. If the effect of angular dispersion would not be taken into account and calibration would be based on the power of the more specular component, $P_{sp} = -30.8$ dBm between $89° < \phi < 93°$, the resulting simulation results would not only lack the angular dispersive effects, but would also result in an underestimation of the total power of about 3 dB, since $P_{tot} = -27.8$ dBm.

7.5   Conclusions and future work

This chapter addresses the importance of angular dispersion for future wireless systems caused by irregular surfaces and changes in dielectric and conductive material properties. An overview is given of two recent methods capable of including these effects in ray-based propagation prediction models. The computational complexity of these models can be high and accurate calibration by measurements of the models can be difficult. A novel approach is presented in a first attempt to model the dispersive effects directly at the receiver. This model generates instantaneous realisations of the channel at the receiver and includes both the coherent and incoherent components.

The results of simulations show that the method can be used to model the dispersive effects of rough surface scattering in a similar way as using the reflection reduction factor for Gaussian surfaces, except that the reduced power in the specular direction is now distributed in the angular domain. A possible approach to include the model into a 3-D ray-tracer is suggested, but future implementation requires additional effort, such as a visibility algorithm and the inclusion of the finiteness of the surfaces.

Furthermore, the model can be calibrated with the aid of high-resolution measurement data, from which angular spread values can be determined. The results obtained from measurements on a rough building surface show that calibration is possible using measurements along a small trajectory and use them to predict the effects of scattering in a wider area.

In summary, the main contributions and innovations of the work presented in this chapter are:

- A novel approach to model the dispersive effects of rough surface scattering directly at the receiver is presented in Section 7.3 and was previously published

by the author in [43]. The model generates instantaneous realisations of the channel at the receiver and includes both the coherent and incoherent components.

- The results from outdoor experiments on a rough building surface are presented in Section 7.4. The effective surface roughness in the model is calibrated through the angular spread that is generated by the surface and which is obtained via high-resolution measurement data. The results obtained from measurements on a rough building surface show that calibration is possible by using measurements in a limited area and extrapolating them to predict the effects of scattering in a wider area.

8

Summary, conclusions and recommendations

8.1 Summary and conclusions

The work presented in this thesis provides a better physical understanding of radiowave propagation in mobile radio channels in urban environments and contributes to the development of improved prediction models that are better matched to the real channel behavior. This is reflected in the following principal contributions of this work.

- Design, implementation and characterisation of a wideband high-resolution measurement system based on advanced channel sounder, a novel 3-D tilted-cross switched antenna array and an improved version of the 3-D Unitary ESPRIT signal processing algorithm.

- Analysis of outdoor experiments in different scenarios, using a novel clustering method to isolate scattering effects and omnidirectional video data to relate them directly to the environment.

- Presentation of a novel approach for the modelling of the scattering effects of building surfaces directly at the receiver as an additional stochastic component in ray-tracing-based propagation models.

The first part of the work was described in Chapters 2, 3 and 4, and covers the design, implementation and verification of a mobile radio channel measurement system. The

main motivation for the development of such a system was the demand for characterising the radio channel under mobile conditions with high resolution performance in azimuth *and* elevation, without ambiguities in the elevation domain.

In Chapter 2, a method was described to increase the effective acquisition rate of an existing channel sounder, which is an integral part of the measurement system. The acquisition rate was increased by a factor of more than 3000, which allows high-speed characterisation of the radio channel and makes it possible to perform measurements at typical urban speeds (< 50 km/h). In order to compensate for a small I/Q imbalance that still exists in the channel sounder, a post-processing method was presented that helps to improve the quality of the measurements. A 3-D antenna array was used in combination with the channel sounder to perform wideband channel measurements within a bandwidth of 100 MHz at 2.25 GHz. The antenna array consists of 31 monopole elements that are positioned in a 3-D tilted-cross geometry and occupies a volume of a sphere with a radius of approximately two times the wavelength. The array was designed such that it has maximum resolution capabilities and uniformity in both azimuth and elevation with a limited number of antenna elements. It exhibits a half-power-beamwidth of 16°, which is 2.5 times better compared to the 40° of a spherical array with the same number of elements. A switched antenna array concept was employed in order to reduce the complexity of the receiver. Additionally, a switched impedance method was developed to reduce the negative effects of mutual coupling in switched antenna arrays by reducing the antenna pattern distortion up to 6 dB and improve the return loss by 9 dB. The method was successfully applied and verified by measurements. The results indicate that mutual coupling effects can already be reduced directly at the antenna, instead of compensating the effects of mutual coupling afterwards via post-processing.

The 3-D tilted-cross antenna array geometry was designed specifically for use with the 3-D Unitary ESPRIT algorithm for high-resolution angle-of-arrival (AOA) estimation. The estimation algorithm was presented in Chapter 3, including an improved 3-D structured-least-squares (3-D I-SLS) method that enables the Unitary ESPRIT algorithm to be applied to the specific category of cross arrays. To estimate the number of sources, which is required information for the Unitary ESPRIT algorithm, a method was used that outperforms commonly used methods. To remove additional and falsely estimated sources caused by overestimating the number of sources, a unique relation between the spatial frequencies of the tilted-cross geometry was used to formulate a reliability indicator ξ and criterion ($|\xi| > t_{rel}$). To minimise the loss of performance due to the effects of shadowing from the antenna support structure, a method was presented that discards erroneous data from the shadowed antenna elements and improves the estimation accuracy in the shadowed areas. Theoretical and experimental analyses in a laboratory environment were successfully performed and support the measurement method and processing techniques. The results show that the AoAs of multiple sources can be accurately characterised with a resolution of less than 5° in both azimuth and elevation.

In Chapter 4, the result of outdoor experiments were presented in order to verify the performance and to demonstrate the system capabilities in real-world mobile

environments. The results in a rural environment in Boxtel, the Netherlands, confirm that the system can be used to characterise the radio channel under mobile conditions. Although elevation angles are estimated accurately, waves reflected by the ground are difficult to detect. This is due to the partial obstruction by the measurement vehicle and support structure, which prevents the ground reflected waves from being observed by all antennas in the array. As a result, the elevation range is effectively limited to $\theta \simeq -7°$ in the worst case, and phase distortions due to ground reflected waves cause a reduction of the estimation performance in elevation. In the azimuthal domain uniform estimation performance was observed over the entire range ($-180° < \phi < 180°$).

The results in an urban environment at the university campus in Eindhoven, the Netherlands, show that the composition of the multipath components along a trajectory can be accurately characterised and tracked. For the first time, omnidirectional video data that were captured during the measurements are used in combination with the measurement results to accurately identify and relate the received radio waves directly to the actual environment while moving through it. These results show that over rooftop diffractions can be identified, as well as reflections from irregular building structures and diffuse scattering effects in the delay and angular domain. When the transmitter is moved from an above to below rooftop scenario, a significant increase in delay and angular dispersion in the azimuth domain, and a decrease in angular dispersion in the elevation domain are observed.

The second part of the work presents the results of experiments in which the high-resolution measurement system, described in the first part, is used in several mobile outdoor experiments. The main objectives of this work were to obtain an improved understanding and more insight in radio propagation with respect to current prediction methods, as well as the clustering of measurement data to isolate scattering effects and to improve further analysis.

In Chapter 5 the measurement system described in Chapters 2 and 3 was used in the framework of a collaboration between TU/e, TNO-ICT and KPN as a diagnostic tool in a dense urban environment in Amsterdam, the Netherlands. It was shown that high-resolution measurements can be used to simulate an actual network scenario and can be very helpful in accurately identifying the main propagation mechanisms. The results underline the limitations of current propagation models used by operators and how this can lead to network problems in more complex environments. It was shown that shadowing and reflections from irregular building structures are important issues and require more accurate propagation modelling in complex environments.

Visual inspection of the multidimensional measurement data can become very complex. To support further data analysis, a method to cluster the multidimensional data is presented in Chapter 6. A hierarchical clustering method is presented that can find clusters in the four-dimensional space (azimuth, elevation, delay, position). The method was successfully applied to the high-resolution measurement data and allows the scattering effects of specific objects to be isolated, which is important for the improvement and calibration of deterministic propagation models. The results

from measurements are compared with the results from a 3-D propagation prediction tool and the dispersive effects in the angular domain, caused by irregular building surfaces and other irregular structures, have attracted particular attention. From the measurements angular spreads of less than one degree up to several degrees were observed, for different objects. These effects are generally not included in deterministic prediction models, which results in erroneous predictions.

In the third part of the work a method is presented to incorporate the angular dispersion caused by irregular surfaces into a ray-tracing-based propagation prediction model. The objective of this work is to model these effects in an efficient way to minimise the complexity and to allow calibration using a limited amount of measurements.

Although several methods have been proposed to model the effects of rough surfaces in ray-based propagation prediction models, their computational complexity can be high and accurate calibration by measurements of the models can be difficult. In Chapter 7, a novel approach is presented in a first attempt to model the dispersive effects, caused by scattering on (stochastic) rough surfaces, directly at the receiver. The method is based on assigning a stochastic effective roughness to a specific surface. The scattering effects caused by the surface roughness incorporate the combined effects of both the surface irregularities and the changes in the material properties. The model generates instantaneous realisations of the channel at the receiver and includes both the coherent and incoherent components. The results of simulations show that the method can be used to model the dispersive effects of rough surface scattering in a similar way as the reflection reduction factor is used for Gaussian surfaces, except that the reduced power in the specular direction is now distributed in the angular domain. A possible approach to include the model into a 3-D ray-tracer was described, but future implementation requires additional effort, such as a visibility algorithm and the inclusion of the finiteness of the surfaces.

The effective surface roughness in the model is calibrated through the angular spread that is generated by the real surface and which is obtained via high-resolution measurement data. The results obtained from measurements on a rough building surface show that calibration is possible using measurements in a limited area in order to accurately predict the effects of scattering in a wider area.

8.2   Recommendations

This section points out recommendations for future research directions, which could lead to extensions of the results achieved in this work.

The study addresses the importance of angular dispersion and contributes to the modelling of angular dispersion caused by irregular surfaces by providing a basis for implementation in ray-tracing-based propagation prediction models. To use the model in real-world scenarios implementation into a ray-tracer is required. The technique can be implemented by applying the method presented in Section 7.3.1 on page 120 to

account for the dispersion caused by the last interaction. For all other interactions a scattering reduction factor for the specular component can be taken into account, as described in Section 7.3.3 on page 126. To handle the effects of scattering from surfaces that have no specular component towards the receiver, the scattering from visible surfaces should first be obtained by assuming them to be infinite and subsequently account for the visibility region. Since the current model is based on a SIMO approach, it would be of high interest to further extend the model in order to obtain a full double-directional (MIMO) channel representation.

The results of the work show that the automatic clustering of data, obtained from the analysis of mobile radiowave propagation experiments, allows to isolate and identify the propagation effects of specific objects. The results from such an analysis can be used directly to calibrate building and material parameters to improve the performance of existing and improved deterministic propagation prediction models, which rely on accurate model calibration [15]. The focus should be on calibration using as *little* measurement data as possible in order to reduce the prediction error as *much* as possible. The results of calibrated predictions should be compared with measurements in several urban environments to determine the performance improvement that can be achieved.

The inclusion of the effects of irregular surfaces can have an important effect on the propagation of waves in NLOS regions where no specular path between the transmitter and receiver exists. This effect can be compared with the effect from diffracted contributions that are generally thought to be the primary cause of the energy transfer in these areas. From the measurement results presented in this study the effects of diffractions where observed in only a few cases. If they can be considered less important and the scattering effects of irregular surfaces contributes more to the total received energy, diffractions in urban environments might not always need to be considered. Since the determination of diffraction points is complex, this will reduce the computational complexity. The computational complexity of ray-based predictions can also significantly be reduced by applying a "pixel" approach [24]. By using this approach the change of the ray parameters along a trajectory is determined via interpolation between the different pixels. If more clustered measurement data is obtained, it can be used to analyse statistics of the rate of change of MPCs along trajectories in different urban environments. This information can be used to further develop the "pixel" approach and determine the allowable pixel size and interpolation techniques.

It was shown in [25] that the scattering effects of vegetation can be significant. The result presented in this thesis have also confirmed the important effects of vegetation in several cases and showed that this also causes significant angular dispersion. To include the dispersive effects of vegetation it is desirable to extend the scattering models in [25] to include the dispersive effect of vegetation in a similar way as that of irregular surfaces.

The continuing trend towards "connected anytime-anywhere" will require a seemingly fluent transition between outdoor mobile cellular radio networks, in different scenarios, to indoor femto-cell or WLAN-based radio networks. These different scenarios

require different type of propagation models, which means that future research should focus more on the *transitions* between different type of propagation models and on the improvement of indoor, and outdoor-indoor propagation prediction. This also requires more knowledge of the double-directional propagation channel and the need for double-directional channel measurements, characterisation and modelling for the analysis of MIMO.

Fulfilling the above recommendations will provide long-term benefits based on improved propagation prediction models that result from efficient *and* effective modelling of the most dominant propagation phenomena. The results will contribute to the design and improvement of current and next generation mobile wireless networks, such that they are better matched to the real-world behaviour of radio waves. This will improve the performance of the mobile wireless infrastructure and helps to fulfil the needs of our future society.

<div align="right">

A

</div>

Radiated field of a passive cylindrical dipole antenna

This appendix derives the current in a passive cylindrical dipole antenna and its radiation field in terms of the impedance of the load, as presented in Section 2.4 on page 21. The derivation is based on the theory in [54, 59].
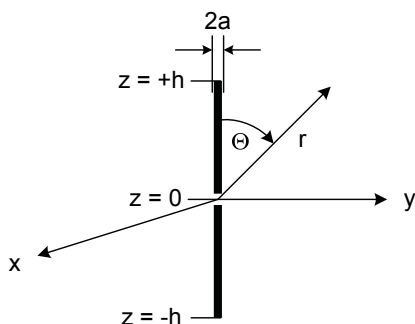

Fig. A.1: Dipole antenna.

The induced current in a passive dipole antenna of height $2h$ (or equivalent monopole antenna of height h) and conductor radius a, as shown in Fig. A.1, in the vicinity of

an active element of comparable length can be approximated by [59]

$$I(z) = E^{\text{inc}}\left[u(z) - v(z)u(0)\frac{Z_L Z_0}{Z_L + Z_0}\right], \tag{A.1}$$

where the impedance of the antenna itself and the load are defined by Z_0 and Z_L respectively. The distribution of the current for an unloaded antenna, $u(z)$, is given by

$$u(z) = \frac{(j4\pi/\zeta_0)[\cos\beta_0 z - \cos\beta_0 h]}{\Psi_{dU}\cos\beta_0 h - \Psi_U(h)}, \tag{A.2}$$

and $v(z)$, the distribution of the current in the active element given by

$$v(z) = \left[\frac{j2\pi}{\zeta_0\Psi_{dR}\cos\beta_0 h}\right][\sin\beta_0(h - |z|) + T(\cos\beta_0 z - \cos\beta_0 h)], \tag{A.3}$$

where $\beta_0 = 2\pi/\lambda$ and the free space impedance $\zeta_0 = \sqrt{\frac{\mu_0}{\epsilon_0}} = 120\pi$. Here, Eq. (A.2) and (A.3) are good approximations when $\beta_0 a \le 0.06$, $a \le 0.1h$ and $\beta_0 h \le 5\pi/4$, but give correct order of magnitude results over wider ranges. The value for T, a ratio factor that involves both h and a, is obtained from

$$T = \frac{\Psi_V(h) - j\Psi_{dI}\cos\beta_0 h}{\Psi_{dU}\cos\beta_0 h - \Psi_U(h)}, \tag{A.4}$$

and the parameters for Ψ are defined as

$$\Psi_V(h) = \int_{-h}^{h}\sin\beta_0(h - |z'|)K(h, z')dz' \tag{A.5}$$

$$\Psi_U(h) = \int_{-h}^{h}(\cos\beta_0 z' - \cos\beta_0 h)K(h, z')]dz' \tag{A.6}$$

$$\Psi_{dU} = (1 - \cos\beta_0 h)^{-1}\int_{-h}^{h}(\cos\beta_0 z' - \cos\beta_0 h)[K(0, z') - K(h, z')]dz' \tag{A.7}$$

$$\Psi_{dR} = \sin\beta_0 h\int_{-h}^{h}\sin\beta_0(h - |z'|)[K(0, z') - K(h, z')]dz' \tag{A.8}$$

$$\Psi_{dI} = (1 - \cos\frac{1}{2}\beta_0 h)^{-1}\int_{-h}^{h}\sin\beta_0(h - |z'|)[K(0, z') - K(h, z')]dz', \tag{A.9}$$

$$\tag{A.10}$$

where $K(z, z') = \frac{e^{-j\beta_0\sqrt{(z-z')^2+a^2}}}{\sqrt{(z-z')^2+a^2}}$. The constants Ψ are tabulated in [59] or can be found by numerically evaluating the integrals, but are only needed here to find T.

To find the radiated field of a passive dipole, the radiated field at distance r caused by a current $I(z)$ in a dipole is used, which is given by

$$E(r, \Theta) = -\frac{j\omega\mu_0 e^{-j\beta_0 r}}{4\pi r}\int_{-h}^{h}I(z')e^{j\beta_0 z'\cos\Theta}\sin\Theta dz'. \tag{A.11}$$

By re-writing Eq. (A.1) as

$$I(z) = \frac{E^{\text{inc}} u(0)}{\beta_0} \left[\frac{u(z)}{u(0)} - \frac{v(z)}{v(0)} \frac{Z_L}{Z_L + Z_0} \right], \tag{A.12}$$

and using

$$\frac{u(z)}{u(0)} = \frac{G_m(\Theta, \beta_0 h)}{1 - \cos \beta_0 h} \tag{A.13}$$

$$\frac{v(z)}{v(0)} = \frac{F_m(\Theta, \beta_0 h) + T G_m(\Theta, \beta_0 h)}{\sin \beta_0 h + T(1 - \cos \beta_0 h)}, \tag{A.14}$$

with

$$G_m(\Theta, \beta_0 h) = \frac{\sin \beta_0 h \cos(\beta_0 h \cos \Theta) \cos \Theta - \cos \beta_0 h \sin(\beta_0 h \cos \Theta)}{\sin \Theta \cos \Theta} \tag{A.15}$$

$$F_m(\Theta, \beta_0 h) = \frac{\cos(\beta_0 h \cos \Theta) - \cos \beta_0 h}{\sin \Theta}, \tag{A.16}$$

the radiated field of the passive dipole antenna can now be obtained by substituting Eq. (A.12) in Eq. (A.11) as

$$E(r, \Theta) = \frac{j \zeta_0 E_z^{inc} e^{-j\beta_0 r}}{2\pi \beta_0 r} u(0) \left\{ \frac{G_m(\Theta, \beta_0 h)}{1 - \cos \beta_0 h} - \frac{F_m(\Theta, \beta_0 h) + T G_m(\Theta, \beta_0 h)}{\sin \beta_0 h + T(1 - \cos \beta_0 h)} \frac{Z_L}{Z_0 + Z_L} \right\}. \tag{A.17}$$

It was shown in [54, 59] that the formulation above directly applies to monopoles over highly conductive ground planes when the appropriate impedances are used.

B

Real-valued transformation and Forward-backward averaging

This appendix defines the real-valued transformation with incorporated forward-backward averaging used in Unitary ESPRIT and presented in Section 3.3.2 on page 37.

If the phase reference for the array steering vectors is chosen to be the array centroid, the centro-symmetry property can be represented by its array steering matrix as follows

$$\mathbf{\Pi}_M \mathbf{A}^{*(i;r)} = \mathbf{A}^{(i;r)}, \tag{B.1}$$

where $\mathbf{\Pi}_M$ is defined as

$$\mathbf{\Pi}_M = \begin{bmatrix} & & & 1 \\ & & 1 & \\ & \cdot^{\cdot^{\cdot}} & & \\ 1 & & & \end{bmatrix} \in \mathbb{R}^{M \times M}. \tag{B.2}$$

From the relation in Eq. (B.1), $\mathbf{A}^{(i;r)}$ is by definition called centro-Hermitian [68,106]. This centro-Hermitian property can be used to improve the estimate of the covariance matrix, obtained from Eq. (1.28), by applying so-called forward-backward averaging. Instead of using $\mathbf{Y}^{(i;r)} \in \mathbb{C}^{(M \times K)}$, an extended matrix

$$\begin{bmatrix} \mathbf{Y}^{(i;r)} & \mathbf{\Pi}_M \mathbf{Y}^{(i;r)*} \mathbf{\Pi}_K \end{bmatrix} \quad \in \mathbb{C}^{(M \times 2K)}, \tag{B.3}$$

can be used to estimate $\hat{\mathbf{R}}^{(i;r)}$ as

$$\hat{\mathbf{R}}^{(i;r)} = \frac{1}{2K} [\mathbf{Y}^{(i;r)} \mathbf{Y}^{(i;r)H} \quad \mathbf{\Pi}_M \mathbf{Y}^{(i;r)*} \mathbf{Y}^{(i;r)*H} \mathbf{\Pi}_K]. \tag{B.4}$$

It can be observed that the extended matrix in Eq. (B.3) itself is also centro-Hermitian. This observation can be used to reduce the computational complexity by transforming Eq. (B.3) to a real-valued equivalent. This is possible because centro-Hermitian matrices of size $M \times K$ form a $M \cdot K$-dimensional linear space over $\mathbb{R}$ [68] and Eq. (B.3) can therefore be mapped to a real valued matrix as

$$\mathbf{Z}^{(i;r)} = \mathbf{Q}_M^H[\mathbf{Y}^{(i;r)} \ \ \mathbf{\Pi}_M\mathbf{Y}^{(i;r)*}\mathbf{\Pi}_K]\mathbf{Q}_{2K} \quad \in \mathbb{R}^{(M \times 2K)}, \tag{B.5}$$

where $\mathbf{Q}$ is a so-called left Π-real transformation matrix defined as

$$\mathbf{Q}_{2\ell} = \frac{1}{\sqrt{2}} \left[\begin{array}{cc} \mathbf{I}_\ell & j\mathbf{I}_\ell \\ \mathbf{\Pi}_\ell & -j\mathbf{\Pi}_\ell \end{array} \right], \tag{B.6}$$

if ℓ is even and

$$\mathbf{Q}_{2\ell+1} = \frac{1}{\sqrt{2}} \left[\begin{array}{ccc} \mathbf{I}_\ell & \mathbf{0} & j\mathbf{I}_\ell \\ \mathbf{0}^T & \sqrt{2} & \mathbf{0}^T \\ \mathbf{\Pi}_\ell & \mathbf{0} & -j\mathbf{\Pi}_\ell \end{array} \right], \tag{B.7}$$

if ℓ is odd. Now, $\mathbf{Z}^{(i;r)}$ can be used to calculate the real-valued covariance matrix.

Glossary

General Notation

$\mathbf{X}$	matrix
$\mathbf{x}$	vector
$\mathbf{X}^T$	transpose of matrix $\mathbf{X}$
$\mathbf{X}^H$	conjugate transpose of matrix $\mathbf{X}$
$\mathbf{X}^*$	conjugate of matrix $\mathbf{X}$
$\mathbf{X}^{-1}$	inverse of matrix $\mathbf{X}$
$\mathbf{X}^\dagger$	pseudo-inverse of matrix $\mathbf{X}$, given by $(\mathbf{X}^H\mathbf{X})^{-1}\mathbf{X}^H$
$\mathbf{X} \otimes \mathbf{Y}$	Kronecker or direct matrix product of matrices $\mathbf{X}$ and $\mathbf{Y}$
$\mathbf{I}_N$	$N \times N$ identity matrix
$\mathbf{0}$	all zeros matrix
$\text{vec}\{\mathbf{X}\}$	column vector that contains the stacked columns of $\mathbf{X}$ below one another
$\mathbb{E}\{x\}$	expected value of x
$\mathbb{P}\{x\}$	probability of occurence of x
$\in$	element of
$\hat{x}$	estimate of x
$< \cdot >$	mean value
$|\cdot|$	absolute value
$\cong$	congruent to
$\simeq$	approximately equal to
$\approx$	almost equal to, asymptotic to
$\neq$	not equal to

Acronyms and abbreviations

2-D	two dimensional
3-D	three dimensional
3G	third generation
3GPP	3rd Generation Partnership Project

4G	fourth generation
A/D	analogue-to-digital
ADC	analogue-to-digital converter
AIC	Akaike information criterion
AOA	angle-of-arrival
BPSK	binaire phase-shift keying
BS	base station
CAS	RMS cluster azimuth spread
CES	RMS cluster elevation spread
CIR	complex impulse response
CRB	Cramer Rao bound
CW	continuous wave
D/A	digital-to-analogue
DAC	digital-to-analogue converter
dB	decibel
dBi	decibel relative to isotropic
dBm	decibel relative to miliwatt
DC	direct current
DSL	digital subscriber line
EM	electromagnetic
EM	expectation maximisation
ESPRIT	estimation of signal parameters via rotational invariance techniques
EVD	eigenvalue decomposition
FB	forward-backward
GDE	Gerschörin disk estimator
GO	geometrical optics
GPS	global positioning system
HPBW	half-power-beam-width
HSDPA	high-speed downlink packet access
HSUPA	high-speed uplink packet access
I	in-phase
IEEE	institute of electrical and electronics engineers
IF	intermediate frequency
I-SLS	improved structured-least-squared
LNA	low noise amplifier
LO	local oscillator
LOS	line of sight
LPF	low pass filter
LS	least-squared
LTE	long term evolution
MC	mutual coupling
MDL	minimum description length
MIMO	multiple-input multiple-output
MoM	method-of-moments
MPC	multipath component

MPSR	multipath power sensitivity ratio
MUSIC	multiple signal classification
NLOS	non line of sight
pdf	probability density function
PDP	power-delay profile
PN	pseudonoise
Q	quadrature
QoS	quality of service
RF	radio frequency
RMS	root mean square
RX	receiver
SAGE	space alternating generalized EM
SCM	spatial channel model
SDMA	spatial-division multiple access
SINR	signal-to-interference-and-noise ratio
SLS	structured-least-squared
SMA	sub-miniature version A
SNR	signal-to-noise-ratio
SSD	simultaneous Schur decomposition
TLS	total-least-squared
TX	transmitter
UCA	uniform circular array
UMTS	Universal Mobile Telecommunication System
URFA	uniform rectangular frame array
WiMAX	Worldwide Interoperability for Microwave Access
WLAN	wireless local area networks

References

[1] Technical Specification Group Radio Access Network, "Physical channels and modulation, 3GPP TS 36.211, V8.1.0," Nov. 2007.

[2] K. H. Teo, Z. Tao, and J. Zhang, "The mobile broadband WiMAX standard (standards in a nutshell)," *IEEE Signal Processing Mag.*, vol. 24, no. 5, pp. 144–148, Sept. 2007.

[3] I. Jami and H. Tao, "Micro-cell planning within macro-cells in UMTS: downlink analysis," in *3rd conf. on 3G Mobile Communication Technologies*, 2002, number 489, pp. 211–215.

[4] A. Fiacco and N. Piercy, "Capacity enhancement for indoor picocells using distributed base stations," in *4th Int. Workshop on Mobile and Wireless Communications Network*, 2002, pp. 278–281.

[5] D.S. Baum, J. Hansen, and J. Salo, "An interim channel model for beyond-3G systems: extending the 3GPP spatial channel model (SCM)," in *Proc. IEEE 61st Veh. Technol. Conf. (VTC 2005 Spring)*, 2005, vol. 5, pp. 3132–3136.

[6] "IST-4-027756 WINNER II D1.1: WINNER II interim channel models," November, 2006.

[7] Luis M. Correia, *Mobile broadband multimedia networks*, Elsevier Science & Technology Books, 2006.

[8] *IlmProp: geometry-based Multi-User MIMO Channel Modelling tool*, Available for download at http://tu-ilmenau.de/ilmprop/.

[9] Giovanni Del Galdo, *Geometry-based Channel Modeling for Multi-User MIMO Systems and Applications*, Ph.D. thesis, Ilmenau University of Technology, Ilmenau, Germany, 2007.

[10] M.F. Iskander and Zhengqing Yun, "Propagation prediction models for wireless communication systems," *IEEE Trans. Microwave Theory Tech.*, vol. 50, no. 3, pp. 662–673, 2002.

[11] H.L. Bertoni, S.A. Torrico, and G. Liang, "Predicting the radio channel beyond second-generation wireless systems," *IEEE Antennas Propagat. Mag.*, vol. 47, no. 4, pp. 28–40, 2005.

[12] T.K. Sarkar, Zhong Ji, Kyungjung Kim, A. Medouri, and M. Salazar-Palma, "A survey of various propagation models for mobile communication," *IEEE Antennas Propagat. Mag.*, vol. 45, no. 3, pp. 51–82, 2003.

[13] M. Coinchon, A.-P. Salovaara, and J.-F. Wagen, "The impact of radio propagation predictions on urban UMTS planning," in *Int. Zurich Seminar on Broadband Communications*, 19-21 Feb. 2002, 32, pp. 1–6.

[14] O.C. Mantel, J.C. Oostveen, and M.P. Popova, "Applicability of deterministic propagation models for mobile operators," in *2nd European Conf. on Antennas and Propagation (EuCAP 2007)*, 2007, pp. 1–6.

[15] J. Jemai, R. Piesiewicz, and T. Kürner, "Calibration of an indoor radio propagation prediction model at 2.4 GHz by measurements of the IEEE 802.11b preamble," in *Proc. IEEE 61st Veh. Technol. Conf. (VTC2005-Spring)*, 2005, vol. 1, pp. 111–115.

[16] V. Degli-Esposti, D. Guiducci, A. de'Marsi, P. Azzi, and F. Fuschini, "An advanced field prediction model including diffuse scattering," *IEEE Trans. Antennas Propagat.*, vol. 52, no. 7, pp. 1717–1728, July 2004.

[17] C.C. Constantinou and M.J. Mughal, "On the modeling of reflected energy from building faces in microcellular mobile radio planning tools," *IEEE Trans. Antennas Propagat.*, vol. 53, no. 8, pp. 2623–2630, Aug. 2005.

[18] Y.L.C. de Jong and M.H.A.J. Herben, "A tree-scattering model for improved propagation prediction in urban microcells," *IEEE Trans. Veh. Technol.*, vol. 53, no. 2, pp. 503–513, Mar. 2004.

[19] D. Didascalou, M. Dottling, N. Geng, and W. Wiesbeck, "An approach to include stochastic rough surface scattering into deterministic ray-optical wave propagation modeling," *IEEE Trans. Antennas Propagat.*, vol. 51, no. 7, pp. 1508–1515, Jul. 2003.

[20] Y. Cocheril, S. Reynaud, and R. Vauzelle, "Comparison between two original methods including scattering in 3D channel simulations," in *Proc. 9th European Conf. on Wireless Technology*, S. Reynaud, Ed., Sept. 2006, pp. 87–90.

[21] E.O. Flores, D.M. Rodriguez, J.J. Gaytan, and J.E. Miller, "Cellular system capacity with smart antennas in dispersive channels," in *Proc. IEEE 50th Veh. Technol. Conf. (VTC1999-Fall)*, 1999, vol. 1, pp. 52–56.

[22] E.M. Vitucci, *Multidimensional characterization of the MIMO Radio Channel*, Ph.D. thesis, University of Bologna, 2007.

[23] Leo Chan and Sergey Loyka, "Impact of multipath angular distribution on performance of MIMO systems," in *Canadian Conf. on Electrical and Computer Engineering*, May 2004, vol. 2, pp. 853–857.

[24] M. Jevrosimovic, *Channel Modelling and Smart Antenna Performance Analysis for UMTS*, Ph.D. thesis, Technische Universiteit Eindhoven, Eindhoven, The Netherlands, 2005.

[25] Y.L.C. de Jong, *Measurement and modelling of radiowave propagation in urban microcells*, Ph.D. thesis, Technische Universiteit Eindhoven, Eindhoven, The Netherlands, 2001.

[26] Y.L.C. de Jong and M.H.A.J. Herben, "High-resolution angle-of-arrival measurement of the mobile radio channel," *IEEE Trans. Antennas Propagat.*, vol. 47, no. 11, pp. 1677–1687, Nov. 1999.

[27] J. Fuhl, J.-P. Rossi, and E. Bonek, "High-resolution 3-D direction-of-arrival determination for urban mobile radio," *IEEE Trans. Antennas Propagat.*, vol. 45, no. 4, pp. 672–682, 1997.

[28] V.-M. Kolmonen, J. Kivinen, L. Vuokko, and P. Vainikainen, "5.3-GHz MIMO radio channel sounder," *IEEE Trans. Instrum. Meas.*, vol. 55, no. 4, pp. 1263–1269, Aug. 2006.

[29] K. Kalliola, H. Laitinen, L.I. Vaskelainen, and P. Vainikainen, "Real-time 3-D spatial-temporal dual-polarized measurement of wideband radio channel at mobile station," *IEEE Trans. Instrum. Meas.*, vol. 49, no. 2, pp. 439–448, Apr. 2000.

[30] M. Alatossava, L. Hentila, V.M. Holappa, and J. Meinila, "Comparison of Outdoor to Indoor and Indoor to Outdoor MIMO Propagation Characteristics at 5.25 GHz," in *Proc. IEEE 65th Veh. Technol. Conf. (VTC 2007 Spring)*, 2007, pp. 445–449.

[31] Xinying Gao, Jianhua Zhang, Guangyi Liu, Ding Xu, Ping Zhang, Yang Lu, and Weihui Dong, "Large-Scale Characteristics of 5.25 GHz Based on Wideband MIMO Channel Measurements," *IEEE Antennas Wireless Propagat. Lett.*, vol. 6, pp. 263–266, 2007.

[32] E. Zollinger, "A Novel Architecture for a Flexible Integrated Wideband Vector Channel Sounder for MIMO System Investigation," in *URSI, General Assembly of the International Union of Radio Science*, Maastricht, Netherlands, 2002.

[33] T. Zwick, D. Hampicke, A. Richter, G. Sommerkorn, R. Thoma, and W. Wiesbeck, "A novel antenna concept for double-directional channel measurements," *IEEE Trans. Veh. Technol.*, vol. 53, no. 2, pp. 527–537, 2004.

[34] R.S. Thoma, D. Hampicke, A. Richter, G. Sommerkorn, A. Schneider, U. Trautwein, and W. Wirnitzer, "Identification of time-variant directional mobile radio channels," *IEEE Trans. Instrum. Meas.*, vol. 49, no. 2, pp. 357–364, 2000.

[35] M.R.J.A.E. Kwakkernaat, Y.L.C. de Jong, and M.H.A.J. Herben, "Mobile high-resolution direction finding of mutlipath radio waves in azimuth and elevation," in *Proc. IEEE 1st BENELUX/DSP Valley Signal Processing Symp.*, Antwerp, Belgium, 2005.

[36] M.R.J.A.E. Kwakkernaat, Y.L.C. de Jong, R.J.C. Bultitude, and M.H.A.J. Herben, "3-D switched antenna array for angle-of-arrival measurements," in *1st European Conf. on Antennas and Propagation (EuCAP 2006)*, Nice, France, Nov. 2006.

[37] M.R.J.A.E. Kwakkernaat, Y.L.C. de Jong, R.J.C. Bultitude, and M.H.A.J. Herben, "High-resolution angle-of-arrival measurements on physically-nonstationary mobile radio channels," *IEEE Trans. Antennas Propagat.*, vol. 56, no. 8, pp. 2720–2729, Aug. 2008.

[38] M.R.J.A.E. Kwakkernaat, Y.L.C. de Jong, R.J.C. Bultitude, and M.H.A.J. Herben, "Reduction of mutual coupling in switched arrays of linear antennas," in *1st European Conf. on Antennas and Propagation (EuCAP 2006)*, Nice, France, Nov. 2006.

[39] M.R.J.A.E. Kwakkernaat, Y.L.C. Jong, J.C. Bultitude, and M.H.A.J. Herben, "Improved structured least squares for the application of Unitary ESPRIT to cross arrays," *IEEE Signal Processing Lett.*, vol. 13, no. 6, pp. 349–352, 2006.

[40] M.R.J.A.E. Kwakkernaat and M.H.A.J. Herben, "Analysis of clustered multipath estimates in physically nonstationary radio channels," in *Proc. IEEE 18th International Symposium on Personal, Indoor and Mobile Radio Communications (PIMRC 2007), (Best paper award)*, Sept. 2007, pp. 1–5.

[41] M.R.J.A.E. Kwakkernaat and M.H.A.J. Herben, "Analysis of scattering in physically nonstationary mobile radio channels," in *2nd European Conf. on Antennas and Propagation (EuCAP 2007)*, Edinburgh, U.K., 2007.

[42] M.R.J.A.E. Kwakkernaat and M.H.A.J. Herben, "Analysis of scattering in mobile radio channels based on clustered multipath estimates," *Int. Journal of Wireless Information Networks (IJWIN) Special Issue: Physical Layer Engineering for Emerging Wireless Applications, (Invited paper)*, 2008.

[43] M.R.J.A.E. Kwakkernaat and M.H.A.J. Herben, "Modelling angular dispersion in ray-based propagation prediction models," in *COST2100, TD(08)519*, Trondheim, Norway, 2008.

[44] J.P.F. Glas, "Digital I/Q imbalance compensation in a low-IF receiver," in *Proc. IEEE Global Telecommunications Conf. (GLOBECOM 98)*, 1998, vol. 3, pp. 1461–1466 vol.3.

[45] A. Manikas, A. Alexiou, and H.R. Karimi, "Comparison of the ultimate direction-finding capabilities of a number of planar array geometries," in *Proc. IEE Radar, Sonar and Navigation*, Dec. 1997, vol. 144, pp. 321–329.

[46] C.A. Balanis, *Antenna theory: analysis and design*, Wiley, Chichester, 1997.

[47] D.S. Baum and H. Bolcskei, "Impact of phase noise on MIMO channel measurement accuracy," in *Proc. IEEE 60th Veh. Technol. Conf. (VTC2004-Fall)*, 2004, vol. 3, pp. 1614–1618.

[48] Daniel S. Baum and Helmut Bölcskei, "Information-theoretic analysis of MIMO channel sounding," *IEEE Trans. Inform. Theory*, 2007.

[49] J. Kivinen and P. Vainikainen, "Calibration scheme for synthesizer phase fluctuations in virtual antenna array measurements," *Microwave and Optical Technology Letters*, vol. 26, no. 3, pp. 183–187, 2000.

[50] K.M. Pasala and E.M. Friel, "Mutual coupling effects and their reduction in wideband direction of arrival estimation," *IEEE Trans. Aerosp. Electron. Syst.*, vol. 30, no. 4, pp. 1116–1122, 1994.

[51] R. Goossens and H. Rogier, "A Hybrid UCA-RARE/Root-MUSIC Approach for 2-D Direction of Arrival Estimation in Uniform Circular Arrays in the Presence of Mutual Coupling," *IEEE Trans. Antennas Propagat.*, vol. 55, no. 3, pp. 841–849, 2007.

[52] R.J.C. Bultitude and N. Adnani, "Analysis of wideband measurement data to assess and predict system performance for IMT2000 systems," in *IEEE Radio and Wireless Conf.*, Denver, CO, USA, 2000, pp. 55–58.

[53] J.D. Fredrick, Yuanxun Wang, and T. Itoh, "Smart antennas based on spatial multiplexing of local elements (SMILE) for mutual coupling reduction," *IEEE Trans. Antennas Propagat.*, vol. 52, no. 1, pp. 106–114, Jan. 2004.

[54] R. King, "Reduction of reradiated field in equatorial plane of parasitic antenna," *IEEE Trans. Antennas Propagat.*, vol. 20, no. 3, pp. 376–379, May 1972.

[55] K. Chen and V. Liepa, "The minimization of the back scattering of a cylinder by central loading," *IEEE Trans. Antennas Propagat.*, vol. 12, no. 5, pp. 576–582, Sep. 1964.

[56] J.L. Smith, "A method to determine the detuning reactance for unused elements in directional arrays," *IEEE Trans. Broadcast.*, vol. 47, no. 3, pp. 259–262, Sept. 2001.

[57] D.V. Thiel and S. Smith, *Switched parasitic antennas for cellular communications*, Artech House, Boston, 2002.

[58] J. Andersen and H. Rasmussen, "Decoupling and descattering networks for antennas," *IEEE Trans. Antennas Propagat.*, vol. 24, no. 6, pp. 841–846, Nov. 1976.

[59] R.B. Mack R.W.P. King and S.S. Sandler, *Arrays of cylindrical dipoles*, Cambridge, New York, 1968.

[60] FEKO, "FEKO Suite 5.1, EM Software and Systems," 2005, http://www.feko.info.

[61] L.C. Godara, "Application of antenna arrays to mobile communications: II. Beam-forming and direction-of-arrival considerations," *Proc. IEEE*, vol. 85, no. 8, pp. 1195–1245, 1997.

[62] H. Krim and M. Viberg, "Two decades of array signal processing research: the parametric approach," *IEEE Signal Processing Mag.*, vol. 13, no. 4, pp. 67–94, 1996.

[63] R. Schmidt, "Multiple emitter location and signal parameter estimation," *IEEE Trans. Antennas Propagat.*, vol. 34, no. 3, pp. 276–280, 1986.

[64] R. Roy, A. Paulraj, and T. Kailath, "ESPRIT–A subspace rotation approach to estimation of parameters of cisoids in noise," *IEEE Trans. Signal Processing*, vol. 34, no. 5, pp. 1340–1342, 1986.

[65] J.A. Fessler and III Hero, A.O., "Penalized maximum-likelihood image reconstruction using space-alternating generalized em algorithms," *IEEE Trans. Image Processing*, vol. 4, no. 10, pp. 1417–1429, 1995.

[66] M. Tschudin, C. Brunner, T. Kurpjuhn, M. Haardt, and J.A. Nossek, "Comparison between unitary ESPRIT and SAGE for 3-D channel sounding," in *Proc. IEEE 49th Veh. Technol. Conf.*, 1999, vol. 2, pp. 1324–1329.

[67] A. Richter, R.S. Thomae, and T. Taga, "Directional measurement and analysis of propagation path variations in a street micro-cell scenario," in *Proc. IEEE 57th Veh. Technol. Conf. (VTC 2003-Spring)*, 2003, vol. 1, pp. 246–250.

[68] M. Haardt and J.A. Nossek, "Unitary ESPRIT: how to obtain increased estimation accuracy with a reduced computational burden," *IEEE Trans. Signal Processing*, vol. 43, no. 5, pp. 1232–1242, May 1995.

[69] M. Haardt and M.E. Ali-Hackl, "Unitary ESPRIT: how to exploit additional information inherent in the relational invariance structure," in *Proc. IEEE Int. Conf. on Acoustics, Speech, and Signal Processing (ICASSP-94)*, Apr. 1994, vol. 4, pp. 229–232.

[70] M. Haardt, "Structured least squares to improve the performance of ESPRIT-type algorithms," *IEEE Trans. Signal Processing*, vol. 45, no. 3, pp. 792–799, 1997.

[71] M. Haardt and J.A. Nossek, "Simultaneous Schur decomposition of several non-symmetric matrices to achieve automatic pairing in multidimensional harmonic retrieval problems," *IEEE Trans. Signal Processing*, vol. 46, no. 1, pp. 161–169, Jan. 1998.

[72] M.D. Zoltowski, M. Haardt, and C.P. Mathews, "Closed-form 2-D angle estimation with rectangular arrays in element space or beamspace via unitary ESPRIT," *IEEE Trans. Signal Processing*, vol. 44, no. 2, pp. 316–328, Feb. 1996.

[73] R. Eckhoff, "Direction-of-arrival determination using 3-axis crossed array and ESPRIT," in *Proc. IEEE 9th Int. Sym. on Personal, Indoor and Mobile Radio Communications (PIMRC1998)*, Sept. 1998, vol. 1, pp. 471–475.

[74] H. Wu, J. Yang, and F. Chen, "Source number estimator using Gerschgorin disks," in *Proc. IEEE Int. Conf. on Acoustics, Speech, and Signal Processing (ICASSP-94)*, 19-22 April 1994, vol. 4, pp. 261–264.

[75] E. Radoi and A. Quinquis, "A new method for estimating the number of harmonic components in noise with application in high resolution radar," *EURASIP JASP*, vol. 8, pp. 1177–1188, 2004.

[76] C.P. Mathews and M.D. Zoltowski, "Eigenstructure techniques for 2-D angle estimation with uniform circular arrays," *IEEE Trans. Signal Processing*, vol. 42, no. 9, pp. 2395–2407, Sept. 1994.

[77] D. J. Bird et al, "Study of broad-scale anisotropy of cosmic-ray arrival directions from 2×10^{17} to 10^{20} electron volts from fly's eye data," *The Astrophysical Journal*, vol. 511, pp. 739–749, 1999.

[78] EPAK GmbH, "Radome specifications," Private communications, 2007, http://www.epak.de.

[79] Point Grey Research Inc., *Ladybug User Manual and API Reference, version 1.1*, available from: http://www.ptgrey.com/, 2003.

[80] Honeywell, *Vehicle Navigation Unit (VNU) Datasheet*, available from: http://www.magneticsensors.com/, 2005.

[81] E.S. Sousa, V.M. Jovanovic, and C. Daigneault, "Delay spread measurements for the digital cellular channel in Toronto," *IEEE Trans. Veh. Technol.*, vol. 43, no. 4, pp. 837–847, Nov. 1994.

[82] CCIR, "Reflection from the surface of the earth, report 1008," in *Propagation in Non-ionized Media, Recommendations and Reports of the CCIR*, Geneva, 1986, Int. Telecomm. Union, vol. 5.

[83] M. Hata, "Empirical formula for propagation loss in land mobile radio services," *IEEE Trans. Veh. Technol.*, vol. 29, no. 3, pp. 317–325, 1980.

[84] N. Czink, E. Bonek, Xuefeng Yin, and B. Fleury, "Cluster angular spreads in a MIMO indoor propagation environment," in *Proc. IEEE 16th Int. Symp. on Personal, Indoor and Mobile Radio Communications (PIMRC2005)*, 2005, vol. 1, pp. 664–668.

[85] N. Czink, G. Del Galdo, and C. Mecklenbräuker, "A novel automatic cluster tracking algorithm," in *Proc. IEEE 17th Int. Symp. on Personal, Indoor and Mobile Radio Communications (PIMRC2006)*, Helsinki, Finland, September 2006.

[86] J. B. MacQueen, "Some methods for classification and analysis of multivariate observations," in *Proc. 5th Berkeley Symp. on Mathematical Statistics and Probability.* 1967, vol. 1, pp. 281–297, University of California Press.

[87] A. K. Jain and Richard C. Dubes, *Algorithms for clustering data*, Prentice Hall, 1988.

[88] B.H. Fleury, "First- and second-order characterization of direction dispersion and space selectivity in the radio channel," *IEEE Trans. Inform. Theory*, vol. 46, no. 6, pp. 2027–2044, Sept. 2000.

[89] M. Bengtsson and B. Volcker, "On the estimation of azimuth distributions and azimuth spectra," in *Proc. IEEE 54th Veh. Technol. Conf. (VTC 2001 Fall)*, Oct. 2001, vol. 3, pp. 1612–1615.

[90] Radioplan GmbH, "RPS 5.3, Radiowave Propagation Simulator," 2006, http://www.radioplan.com.

[91] J. Lahteenmaki, "Testing and verification of indoor propagation models," in *COST 231 TD(94)111*, 1994.

[92] L. Vuokko, P. Vainikainen, and J. Takada, "Clusterization of measured direction-of-arrival data in an urban macrocellular environment," in *Proc. IEEE 14th Int. Symp. on Personal, Indoor and Mobile Radio Communications (PIMRC 2003)*, 2003, vol. 2, pp. 1222–1226.

[93] L. Vuokko, P. Vainikainen, and J. Takada, "Clusters extracted from measured propagation channels in macrocellular environments," *IEEE Trans. Antennas Propagat.*, vol. 53, no. 12, pp. 4089–4098, 2005.

[94] Y. Cocheril, R. Vauzelle, and L. Aveneau, "3D Channel Simulations Including Scattering from Non-Gaussian Rough Surfaces," in *Proc. IEEE 64th Veh. Technol. Conf. (VTC 2006 Fall)*, 2006, pp. 1–5.

[95] Y. Cocheril and R. Vauzelle, "A new ray-tracing based wave propagation model including rough surfaces scattering," *Progress In Electromagnetics Research, PIER*, vol. 75, pp. 357–381, 2007.

[96] V. Degli-Esposti and H.L. Bertoni, "Evaluation of the role of diffuse scattering in urban microcellular propagation," in *Proc. IEEE 50th Veh. Technol. Conf. (VTC 1999 Fall)*, 19–22 Sept. 1999, vol. 3, pp. 1392–1396.

[97] V. Degli-Esposti, "A diffuse scattering model for urban propagation prediction," *IEEE Trans. Antennas Propagat.*, vol. 49, no. 7, pp. 1111–1113, Jul. 2001.

[98] V. Degli-Esposti, F. Fuschini, E. M. Vitucci, and G. Falciasecca, "Measurement and modelling of scattering from buildings," *IEEE Trans. Antennas Propagat.*, vol. 55, no. 1, pp. 143–153, Jan. 2007.

[99] R.A. Serway and R.J. Beichner, *Physics: for scientists and engineers with modern physics*, Saunders College Publishing, London, 5th edition, 2000.

[100] J. A. Oglivy, *Theory of Wave Scattering From Random Rough Surfaces*, Taylor & Francis, 1991.

[101] Petr Beckmann and Andre Spizzichino, *The scattering of electromagnetic waves from rough surfaces*, Artech House, 1987.

[102] F.G. Bass and I.M. Fuks, *Wave Scattering from Statistically Rough Surfaces*, Pergamon, Oxford, 1979.

[103] Y. Lostanlen and G. Gougeon, "Introduction of diffuse scattering to enhance ray-tracing methods for the analysis of deterministic indoor UWB radio channels," in *Proc. Int. Conf. on Electromagnetics in Advanced Applications (ICEAA 2007)*, 17–21 Sept. 2007, pp. 903–906.

[104] A. Papoulis, *Probability, random variables and stochastic processes*, McGraw-Hill, 4th ed. edition, 2002.

[105] S. Loyka and G. Tsoulos, "Estimating MIMO system performance using the correlation matrix approach," *IEEE Commun. Lett.*, vol. 6, no. 1, pp. 19–21, 2002.

[106] M. Haardt and J.A. Nossek, "Structured least squares to improve the performance of ESPRIT-type high-resolution techniques," in *Proc. IEEE Int. Conf. on Acoustics, Speech, and Signal Processing (ICASSP-96)*, May 1996, vol. 5, pp. 2805–2808.

Samenvatting

De toepassing van multi-antenne technieken is een belangrijke manier om de bandbreedte efficiëntie van mobiele draadloze communicatiesystemen te vergroten. Het effectief en betrouwbaar ontwerpen van deze multi-antenne systemen vereist een grondige kennis van de radiogolfvoortplanting (radiopropagatie) in cellulaire omgevingen.

Het doel van het werk beschreven in dit proefschrift is het verkrijgen van een beter fysisch inzicht in de radiopropagatie in mobiele kanalen en het creëren van een basis voor verbeterde voorspellingen van radiopropagatie in stedelijke omgevingen door gebruik te maken van driedimensionale radiopropagatie experimenten, simulaties en ruimtegolfmodellering. De nadruk ligt met name op: het ontwerpen van een geavanceerd driedimensionaal mobiel radiokanaal meetsysteem, het verkrijgen van meetdata uit mobiele radiopropagatie experimenten, de analyse van de meetdata en het modelleren van radiogolf verstrooiing in het hoekdomein, voor het verbeteren van deterministische radiopropagatie modellen.

Het eerste gedeelte van de studie presenteert het ontwerp, de implementatie en de verificatie van een breedbandige radiokanaalsounder voor het in het hoekdomein karakteriseren van radiopropagatie effecten in mobiele radiokanalen. Het systeem werkt met behulp van een verbeterde versie van het 3-D Unitary ESPRIT algoritme, dat gebruik maakt van complexe impulsresponsiedata die verkregen is van antennes in een geavanceerd driedimensionaal geschakeld antenne stelsel in de vorm van een gedraaid kruis. Terwijl het systeem beweegt met een gematigde snelheid kan het algoritme de vertragingen en de aankomsthoeken van radiogolven in zowel het horizontale als verticale vlak met hoge resolutie schatten. Voor het eerst is gebruik gemaakt van omnidirectionele videodata, verkregen tijdens de mobiele metingen, om in combinatie met de meetdata zeer nauwkeurig aan te geven wat de relatie van de ontvangen radiogolven met de omgeving is, terwijl er door de omgeving wordt bewogen.

Het tweede gedeelte van de studie presenteert de resultaten van experimenten waarbij het meetsysteem, beschreven in de voorgaande deel, gebruikt is in verschillende openlucht experimenten in verschillende configuraties. Het doel van deze metingen is om meer kennis en inzicht te vergaren over de manier waarop radiogolven zich voortplanten. De resultaten van deze metingen hebben specifiek de aandacht gevestigd op het dispersieve karakter van radiogolven veroorzaakt door onregelmatige oppervlakte structuren. Deze effecten beïnvloeden niet alleen het totale ontvangen vermogen in

stedelijke gebieden, maar kunnen ook een grote invloed hebben op de beoogde werking van multi-antenne systemen en de manier waarop deze kunnen worden ingezet. Om de data representatie te verbeteren en om verdere dataverwerking te ondersteunen is een hiërarchische clustering methode ontwikkeld die met succes clusters kan onderscheiden in de multidimensionale data. Door gebruik te maken van de omnidirectionele video informatie kunnen deze clusters gerelateerd worden aan de objecten in de omgeving, elk met hun eigen specifieke verstrooiings kenmerken. Deze resultaten zijn belangrijk voor de verbetering en kalibratie van deterministische radiopropagatie modellen.

In het derde deel van de studie wordt er een nieuwe methode gepresenteerd waarmee de hoekdispersie, veroorzaakt door onregelmatige oppervlakken, kan worden meegenomen in een op stralenbenadering gebaseerd radiopropagatie model. De methode is gebaseerd op het toekennen van een effectieve ruwheid aan een specifiek oppervlak. Op deze manier kan de verstrooiing van het vermogen in het hoekdomein worden meegenomen, dit in tegenstelling tot de veelal gebruikte reflectie reductiefactor voor Gaussische ruwe oppervlakken. De resultaten van geclusterde meetdata zijn gebruikt voor de calibratie van het model en laten zien dat hiermee een verbeterde voorspelling van het radiokanaal kan worden bepaald dat beter aansluit op het propagatie gedrag van radiogolven in de werkelijkheid.

Acknowledgements

"Synergy is the highest activity of life."
Stephen R. Covey

The research journey that has led to this thesis would not have been possible without the help and support of many people. I would like to express my sincere gratitude to the following people.

I am very grateful to dr. Matti Herben, for offering me support, guidance, encouragement and the freedom of exploring new fields. He was always available for feedback and interesting discussions, which gave me new inspiration. Special thanks also to my first promotor prof. Erik Fledderus for providing valuable advices and support. I also thank the Eindhoven University of Technology (TU/e), Koninklijke PTT Nederland (KPN) and Netherlands Organization for Applied Scientific Research (TNO) for providing financial support to this work through the Liquid Bandwidth program within the research framework Dutch Research Delta (DRD).

I would like to thank all my colleagues, students and friends who contributed to the pleasant atmosphere and good cooperation while working within the Radiocommunications group (ECR) at the TU/e. I always enjoyed the lunches, social events and the discussions during the coffee breaks where we, from our point of view, solved the biggest problems and riddles in the world. I especially would like to mention Iwan Akkermans, Remco Dirks, Els Gerritsen-Lecluse, José Hakkens-Jansen, Marija Jevrosimovic, Fabiola Jiménez, Imran Kazim, Maurice Kastelijn, Doret Pellegrino, Susan de Leeuw, Peter van Leuven, Thijs van Lieshout, Jean-Paul Linnartz, Ewart Martijn, Emilia Motoasca, Dries Neirynck, Robert van Poppel, Ad Reniers, Tim Schenk, Peter Smulders, Erwin Verdurmen, Raymond West and Haibing Yang. The technical assistance from Rainier van Dommelen and Jaap Swijghuisen Reigersberg is greatly appreciated. Your work improved the hard- and software of the new channel sounder presented in Chapter 2 and your assistance during the experiments helped to obtain several of the results presented in this thesis.

All the colleagues at the Communication Research Centre Canada (CRC) in Ottawa, Canada were greatly appreciated for their support, pleasant company and nice atmosphere during my visits. The work of Jeff Pugh, Tyler Smith and Hong Zhu in designing and implementing parts of the hard and software presented in Chapter 2 is gratefully acknowledged. I am also thankful for the use of the anechoic chambers, the measurement equipment and the support by the David Florida Laboratory (DFL) of the Canadian Space Agency (CSA).

Also, I like to thank all the colleagues from TNO Information and Communication Technology, the Netherlands, for their support, inspiring discussions and participation in this project. I would like to mention Job Oostveen, Marijn Rijken, Yohan Toh and Haibin Zhang and especially Onno Mantel for his interesting discussions and feedback during many of the progress meetings.

KPN gave me the opportunity to perform measurements within their mobile network, for which I am grateful. Especially, the support by Hendrik de Greef is greatly appreciated. I also thank Matthijs Klepper for letting me share my ideas and results with the radio acces group.

I thank prof. Thomas Kürner for being my second promotor and prof. Martin Haardt and prof. Anton Thijhuis for reading the thesis and commenting on the draft version. Your review and constructive comments have helped me to improve this thesis. I am very grateful to prof. Robert Bultitude and dr. Yvo de Jong for being part of the core-committee, but even more for our pleasant cooperation, interesting discussions, difficult questions and constructive feedback. You two are greatly appreciated for the reading and commenting on many of the manuscripts I produced. The results achieved in this cooperation are reflected in Chapter 2 and 3 of this thesis.

I also thank my parents, other family members and all friends for their unconditional support and understanding. Finally, I wish to thank you, Anne-Marie for your love, patience and encouragement, which helped me to complete this work.

Curriculum vitae

Maurice Kwakkernaat was born in Venray, the Netherlands, on 21 February 1978. After finishing secondary school at the R.K. MAVO Maasdorpen in Meerlo in 1994 and, subsequently, finishing the Regional Training Centre (ROC) for secondary vocational education (MTS) at the department of Technique and Technology in Helmond in 1998, he finished the Fontys University of Applied Sciences (HTS) at the department of Electrical Engineering in Eindhoven in 2001. He started studying Electrical Engineering at the Eindhoven University of Technology (TU/e) in Eindhoven, the Netherlands in 2001. During this study he worked as a part-time research engineer at Experts in Connectivity and Communications Technology (ECCT) in Eindhoven, the Netherlands. The research for his M.Sc. Thesis was performed within the Propagation Research Group at the Communication Research Centre Canada (CRC) in Ottawa, Canada and was concerned with the design of a 3-D antenna array for high-resolution angle-of-arrival measurements. He received the M.Sc. Degree in 2004.

In September 2004, he started working towards the Ph.D. Degree as a Research Assistant within the Radiocommunications chair at the TU/e. The work was performed in cooperation with CRC and, in a later stage, the research framework Dutch Research Delta (DRD), a research cooperation between Koninklijke PTT Nederland (KPN), Netherlands Organization for Applied Scientific Research (TNO) and a large number of Dutch universities. He also worked as a freelance consultant in the area of wireless communications.

The results of the work presented in this thesis have been published in over 8 contributions to international journals and conferences. In September 2007, Maurice received a best paper award at the IEEE PIMRC2007 conference. In 2008 his work has been recognised with the first Netelcom Award, awarded by the professional organisation of suppliers of telecommunication equipment in the Netherlands (Netelcom), as the most innovative and scientific contribution of Ph.D. research work within the research framework DRD.

As of January 2009, Maurice will be with TMC Electronics in Eindhoven, the Netherlands.